UNDERSTANDING LENGTH SCALES OF DIFFUSION IN HIERARCHICAL MATERIALS

A DISSERTATION
SUBMITTED TO THE FACULTY OF THE
UNIVERSITY OF MINNESOTA
BY

CHOONGSZE LEE

IN PARTIAL FULFILMENT OF THE REQUIREMENTS
FOR THE DEGREE OF
DOCTOR OF PHILOSOPHY

Advisors:
PAUL J. DAUENHAUER
MICHAEL TSAPATSIS

APRIL 2022

Acknowledgements

Among the many people I have crossed paths with the last five years, I would like to extend particular acknowledgement to a special few. Foremost, I would like to express my sincere gratitude to my advisors, Professors Paul Dauenhauer and Michael Tsapatsis, for their guidance and support during my PhD. Paul has taught me creativity is a valuable tool in scientific research and I greatly admire his dedication to his craft. I would also like to thank my preliminary and doctoral final exam committee members, Professors Wei-Shou Hu, Alon McCormick, Andre Mkhoyan, Nicholas Race, and Courtney Roberts, for taking the time to share insightful comments and suggestions during this process. Additionally, I very much appreciate the helpful discussions with students, staff, and faculty from the Catalysis Center for Energy Innovation that funded this work.

This thesis could not have been completed (or even started) without my collaborators of three years – Dr. Heng Dai and Professor Jeffrey Rimer at the University of Houston. We initiated the project with what we previously called “strawberry” zeolites, learned some stuff, and moved up the alphabet to rename them to…fins! Thank you for working with me as we fine-tuned the technique from its conception. I would also like to thank Dr. Thuy T. Le and Kumari Shilpa from the Rimer Group as well as Dr. M. Alexander Ardagh, Professor Manish Shetty, Dr. Gaurav Kumar, and Professor Omar Abdelrahman from Dauenhauer Lab for the collaborative work included in this thesis. Additionally, I very much appreciate the helpful discussions with students, staff, and faculty from the Catalysis Center for Energy Innovation, the Department of Energy Research Center that funded this work.

I have worked alongside a multitude of inspiring scientists in the Dauenhauer and Tsapatsis Labs, including Katie, Sabrina, Limin, Matheus, Greg, Alex, Manish, Gaurav, Vineet, Ankita, Xinyu, Yutong, Supriya, Nathan, Isaac, Ming, Jimmy, Amber, and Sallye. I have learned so much from each of you, from our drive together to Chicago, our many meals together (I honestly think I know most

of your Chipotle orders), to who to partner with in escape rooms, and who to not partner with if we were stuck in a horror movie. Thank you for the laughs, the helpful discussions, and sharing this journey with me. I have to especially acknowledge my lab companion, Yutong Pang, and fourth floor mate, Supriya Ghosh, who have thankfully been by my side for the past five years as we navigated graduate school together. I cannot imagine Amundson Hall without you two and will dearly miss our Pusheen™ exchanges and our photography walks together.

In early summer of 2016, I asked Dr. Raj Rajagopalan at ExxonMobil what a zeolite was. I miss our daily conversations that summer (standing outside in Houston heat – what we were thinking?) as we attempted to answer that question and other interesting ones. The next year, Dr. Tilman Beutel and Keith Hajkowski at ExxonMobil (New Jersey) introduced to me the world of infrared spectroscopy and zeolite characterization. Even better, they demonstrated to me the values of integrity and persistence in pursuance of science. My conversations with these mentors led specifically to my interest in the work presented in this thesis. For that, I am very grateful.

I cherish the many friendships I have made throughout graduate school in the CEMS department. From paintball outings and conferences together with the catalysis groups, to exploring state parks and the state fair with my fellow first years (which I still think of us as), to taking the first Friday of each month to buy beer in the roundtable committee, and volunteering with Science for All - this community is really special, and I am grateful to have been a part of it. To my friends in NILS and my beloved chosen family – you know who you are. Thank you for providing much needed reprieve and safe haven for me to escape to this past decade. I always look forward to our time together.

Most importantly, all of my love and gratitude to my unwavering support system: mom, dad, my brothers, Janet, Mark, Doc, and Alexander. To Alexander, you are my rock. I could not have done this without you.

Table of Contents

List of Tables

List of Figures

Chapter 1 - Introduction

1.1 Motivation

Most of the world's basic fuels and chemicals pass through zeolites, microporous materials widely used as shape-selective catalysts and absorbents across a range of industries, including petrochemical, agricultural, and water treatment facilities.[1,2] The global zeolite market size was valued at $13.2 Billion in 2022 and expected to grow in value by 6.2% from 2022 to 2030.[3] Processes in the petrochemical industry that utilize zeolites include fluid catalytic cracking,[4,5] olefin isomerization and oligomerization,[6,7] and aromatics production.[1] Zeolites are such critical components in refineries that their cost was the basis of the Final Investment Decision (FID) for Chevron when evaluating the recent installment of new catalytic crackers, a $10B investment expected to operate for the next 30 to 40 years.[3]

The increase in CO_2 emissions and concomitant climate change has motivated a focus on replacing fossil fuel derived carbon with renewable, carbon-neutral sources. Just as zeolites have played a critical role in transforming and catalyzing the fuels and chemicals of the petrochemical industry in the past 50 years, they can drive the industrial production of the next wave of renewable fuels and chemicals in the next 50 years. However, opportunities for and scalability of next-generation technologies that utilize alternative feedstocks, such as methane-to-methanol[2,8] and methanol-to-olefins[9,10] processes, ultimately depend on return on investment dictated by process efficacy. High catalyst performance is required for renewable technology to compete with petroleum-based technology, therefore motivating a need for greater understanding of the structure of these materials.

There are currently more than 250 synthetic zeolites ranging in framework, dimension, and channel as well as acidic properties and pore topologies (Figure 1-1).[11] To compare and contrast such a wide range of zeolites, key catalyst performance metrics are measured: 1) rate enhancement via an increase in activity, 2) higher selectivity to desired products, and 3) longer stability under high temperature reaction conditions. In order to optimize the aforementioned catalyst performance metrics, we attribute proxy parameters in zeolite design that we can observe or measure using characterization tools to further develop scaling relationships, and eventually, catalyst design principles.

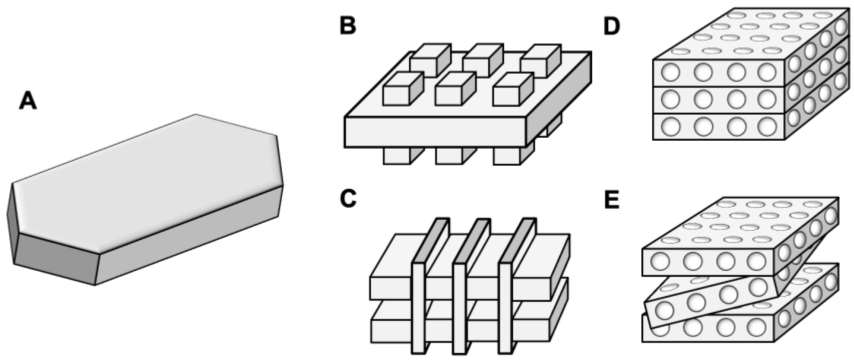

Figure 1-1. (A) Zeolite particle with (B-E) various dimensions, channels, and sites distribution.

1.2 Background

The development of design principles for heterogenous catalysts that operate at the gas-solid interface requires an in-depth understanding of the hierarchical structure of the material. Zeolites are microporous materials consisting of a silicate (SiO_4) framework that allows for acid strength modification via isomorphic substitution with heteroatoms (Al, P, B, Ti, Ge, Sn, Zr,…). Hierarchical structure classification employs the use of *"member rings (MR)"* i.e., intersecting nodes for categorization of pore sizes, with small pores defined as <8 MR, medium pores as ~10 MR, and large pores as >12 MR.

Experimental methods used for acid site quantification and distribution include direct and indirect methods. Direct methods involve measuring the protons and framework aluminums, i.e. acid sites, via ^{1}H-NMR and ^{27}Al-MAS-NMR spectroscopy.[12] Indirect detection methods involve the sorption of probes and measuring the perturbations via gravimetry,[13] calorimetry,[14] vibrational spectroscopy,[15-17] and reactive tests via *in situ* poisoning with pyridine.[18,19] The substitution of heteroatoms into the SiO_4 framework results in perturbations that can be measured by vibrational spectroscopy techniques, including infrared (IR),[20-

[24] Raman,[25-27] quasi-elastic neutron scattering,[28-30] and electron energy loss spectroscopy (EELS).[31-33] The bulk of this thesis focuses on the use of probes with Fourier-Transformed Infrared (FTIR) spectroscopic technique for acid site characterization.

The utility of probe molecules in infrared spectroscopy is ubiquitous in the catalysis field for assessing the number and type of acid sites in zeolites. The structures of common probes, such as ammonia, pyridine, benzene, and carbon monoxide, and acid-base interaction mechanisms with sites are observable and even quantifiable via IR.[34-38] Probe diffusion through zeolites is intrinsically heterogenous due to differences in framework types, distribution of acid sites, and interconnected channels. The appropriate selection of a probe molecule corresponding to the zeolite and chemistry of interest include the following criteria: 1) dominating base and rather weak acidic properties, 2) ability to distinguish between sorption on protonic (Brønsted) and aprotic (Lewis) acid sites, and 3) comparable size to that of the reactant.[39] Pyridine derivatives are more commonly used than amine derivatives because Bronsted and Lewis acidity are more pronounced in the IR spectra.[40] Most research focuses on finding probes small enough to enter pores, therefore reducing the experimental scope to studying only the length scale for diffusion. To grasp a better understanding of molecular mobility in zeolites, it is helpful to study diffusion at the single-molecule probe level.[41] In this work, we explored substituted pyridines as probes that “just fit” into the pores due to steric hindrance, allowing for structure-diffusivity relationship that correlates time scale with length scale of diffusion.

There are three main methods for diffusion in zeolites: single-file, Knudsen, and molecular.[42] In the single-file case, the molecules are too small to pass each other and they simply fit inside the zeolite cage, which we can simplify as a cylindrical tube. The second type is Knudsen, where the molecules are smaller so molecule-wall interaction becomes more important. With even smaller molecules that are significantly smaller than the cylinder pore, molecular, i.e., molecule-to-molecule interactions dominate. The two diffusion methods that apply in this work are the single-file and Knudsen, as the molecules barely fit inside the cylindrical pores, where molecule-wall and adsorbate-site interactions are important. Specifically in this work, the molecules travel through the zeolite channels via a cage-hopping mechanism, adsorbing to the sites as they diffuse through the length of the crystal.[11]

As shown in Figure 1-2, upon interaction with the probe molecule, the acid sites on the zeolitic framework are perturbed, an effect empirically observed using vibrational spectroscopy. IR spectra for catalyst characterization is typically reported in the mid-range IR, with frequency measurements from 4000 to 800 cm^{-1} interval.[44] The three states (zeolitic framework ZH, base B, and formed species ZH---B) can be correlated to distinct features in the IR spectra (Figure 1-2). With only the zeolitic framework (ZH), there are 3 vibrational modes of SiOH, 1 stretching and 2 bending in/out of plane, which appears in the 4000 to 3000 cm^{-1} interval. Upon interaction with base B, there is a negative shift, with magnitude of the shift partially corresponding to the strength of the interaction. The interaction of B with ZH can range from weak (0-400cm^{-1} shift), such as van der Waals type bonding, to medium (400-1000 cm^{-1} shift), to strong (1000-2000 cm^{-1} shift), such as hydrogen bonding. As with any acid/base chemistry, the interaction can be so strong that there is a complete proton transfer, resulting in the formation of anionic Z- and protonated BH+. The first type of interaction describes covalent interactions, while the latter type describes ionic interaction, which may show up in overlapping regions of the IR spectra. The likelihood of complete proton transfer depends on the hydrogen bond strength of the acid ZH, i.e. acid site strength, the proton affinity of the base B, the stabilization of ionic pairs once formed, and other factors such as solvent and surface effects. The stronger the base, the weaker the hydrogen bond of the ionic pair; thus, the reason that the frequency for complete proton transfer is in range of “medium strength” is due to this compensation. The proton affinity for pyridine, ammonia, and most nitrogen-containing probes is around 200 kcal mol^{-1} therefore resulting in a high likelihood of formation of the protonated hydrogen-bonded BH+ with anionic pair Z-.[45]

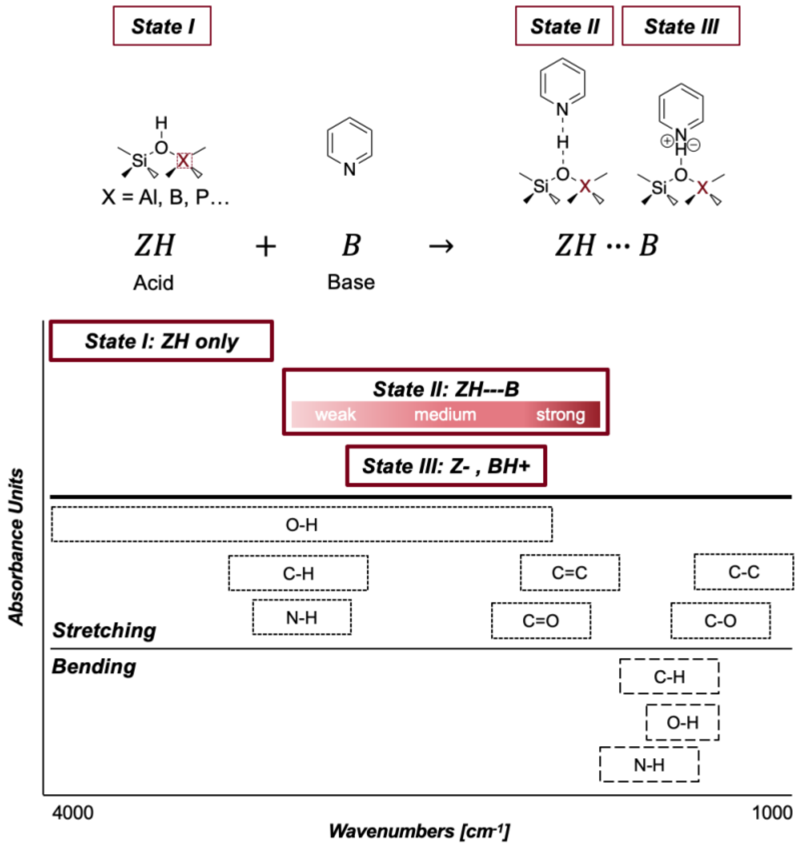

Figure 1-2. (Top) Formation of ZH---B from acid site ZH and base B. (Bottom) Simplified schematic of IR spectroscopy features and vibrational modes expected from different states of adsorption and bonds.

1.3 Thesis Scope and Objectives

In **Chapter 2**, we detail the experimental procedure and analysis in the use of bulky amines, specifically 2,4,6-trimethylpyridine (TMPyr) and 2,3-dimethylpyridine (DMPyr) as probe molecules in IR spectroscopy to assess internal diffusion of zeolites. In **Chapter 3**, we present an alternative, facile approach to enhance mass transport properties of zeolites by the epitaxial growth of fin-like protrusions on seed crystals. We validate this generalizable methodology on two common zeolites, MFI- and MEL-type, and confirm that fins are in crystallographic registry with the underlying seeds, and that secondary growth does not impede access to micropores. In **Chapter 4**, we extended the scope of the technique by demonstration on finned two-dimensional ferrierite (FER). Time-resolved titration of Brønsted acid sites confirmed the improved mass transport properties of finned zeolites compared to conventional analogues. These findings highlight the advantages of introducing fins through facile and tunable post-synthesis modification to impart material properties that are otherwise unattainable by conventional synthesis methods. In **Chapter 5**, we applied the technique to an entirely new categorization of zeolite, core-shell and egg-shell MFI and MEL-type catalysts. Here, we systematically assessed the impact of mesoscopic gradients in acid site concentration: core-shell zeolites possess catalytically active cores and passivated shells of varying thickness while egg-shell configurations comprised of an inert core and catalytically active shell. Time-resolved acid titration of core and core-shell catalysts confirmed that the siliceous shell introduces a hydrophobic exterior that impacts molecular diffusion. In **Chapter 6**, we evaluate a set of progressively stronger solid acid catalysts for the catalytic C-O bond cleavage and dehydration of tetrahydrofuran. We show that selectivity to products, mainly butadiene and propene, was controlled by the interplay of enthalpy-entropy contributions to dehydra-decyclization and retro-Prins reactions, respectively. Collectively, this thesis presents the time-resolved FTIR spectroscopic technique as an alternative approach to assess mass transport properties of zeolites by correlating amine diffusion time scales and length scales. We demonstrate that this approach can be used to elucidate the enhanced performance of commercial catalysts, with the promise of becoming a generalized tool for characterization of zeolites across a broad range of framework types.

Chapter 2 – Understanding Length Scales of Diffusion in Hierarchical Materials

*Reproduced with permission from C. Lee, H. Dai, M. A. Ardagh, M. Tsapatsis, J. Rimer, P. J. Dauenhauer. Understanding Length Scales of Diffusion in Hierarchical Materials. *In Prep* (2022).

2.1 Introduction

The utility of probe molecules, such as pyridine, benzene, and mesitylene in infrared (IR) spectroscopy is ubiquitous in the catalysis field to assess the number and type of sites in zeolites. This work describes a methodology to assess Brønsted acid site (BAS) distribution in medium pore two- and three-dimensional zeolites. Time-resolved FT-IR spectroscopy is a powerful technique to elucidate transient diffusion of organic probe molecules through zeolite pores by assessing the distinct transport properties of seed and finned MFI, MEL, and FER zeolites, a new class of hierarchical material. We present an alternative approach to compare internal diffusion properties of zeolites using bulky, sterically hindered amines. The method uses 2,4,6-trimethylpyridine and 2,3-dimethylpyridine, both of which diffuses through MFI/MEL and FER frameworks, respectively, over the time scale of 4000 minutes. By observing the titration of BAS over time and analyzing differential data, distinct diffusion regimes within the zeolite confinements between fins and seed crystals are discerned. Additionally, a correlation was found between the relative number of fins and enhanced transport due to diffusion time scales, which contributed enhanced catalyst lifetime and performance. This methodology can be extended to probe diffusion regimes and obtain active site distributions of various zeotype catalysts.

2.2 Experimental Procedure

Figure 2-1 depicts an overview of the technique. Time-resolved spectra were measured using a Fourier-transform infrared spectroscopy (FTIR) with a HeNe laser and RT-DLaTGS detector (Bruker Vertex 70, 20 kHz scanner velocity, 6 mm aperture, KBr beam splitter). For sample preparation, 15 mg of powder catalyst sample was homogenized using an agate mortar and pestle, pressed (Pike Technologies, CrushIR Digital Hydraulic Press) at ~3 ton for 5 min into 13 mm-diameter pellets (International Crystal Laboratories, KBR Die, CAS no.7758-02-3) and inserted into the cell body (Harrick Scientific, High Temperature Cell, Part no. HTC-M-05, CaF_2 windows). Before inserting each sample pellet, a background spectrum was collected (64 scans, 4 cm^{-1} resolution) with the empty cell. A K-type thermocouple (Harrick Scientific, Part No. 008-144) was in constant intimate contact with the sample pellet holder to measure the temperature. The manufacturer-provided cartridge heater (100W, 24V) was controlled via a temperature controller in cascade mode (Omega CN7800). To ensure that the CaF_2 windows of the sample cell does not overheat, cooling water was continuously pumped (Control Company, Variable Flow Chemical Pump) and flowed through water cooling ports connected to the cell body. FTIR spectra (64 scans, 4 cm^{-1} resolution, scan range from 4000 to 1000 cm^{-1}) were saved continuously at different time intervals during the duration of the experiment: every 30 s for the first 30 min, then every 10 min for the rest of the experiment (Figure 2-2).

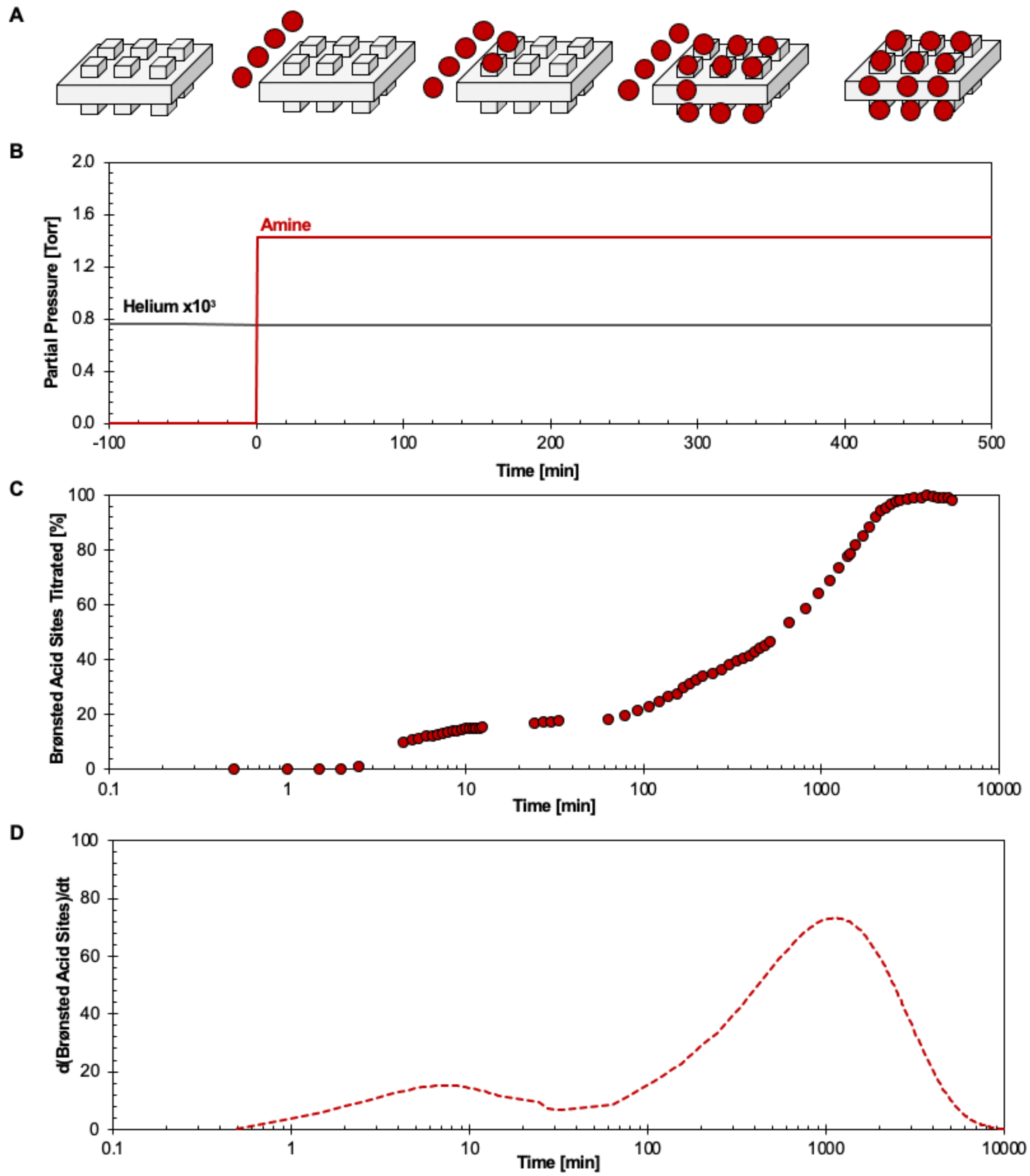

Figure 2-1. Overview of Method.

(A) Simplified schematic of probe molecules (red) diffusing through the zeolite particle during the time scale of experiment (~72 hrs). (B) Partial pressures of Helium and amines (2,4,6-trimethylpyridine or 2,3-dimethylpyridine) during each run, indicating time zero as the start of the run. (C) Representative data set of Brønsted acid sites (BAS) titration by 2,4,6-trimethylpyridine over time. Data collected by integration of 1565 cm^{-1} peak area over time. (D) Derivative of Brønsted acid sites (BAS) titration by 2,4,6-trimethylpyridine over time. The derivative plot was obtained via the following procedure - fitting smoothing spline function over BAS titration over time, taking discrete derivative between each point, fitting the derivative plot with peak fitting function in MATLAB.

Cold 2,4,6-trimethylpyridine (Sigma-Aldrich, CAS no. 108-75-8, 99%) and 2,3-dimethylpyridine (Sigma-Aldrich, CAS no. 583-61-9, 99%) were used for dosing in FTIR. For the amine dosing process, Helium gas (Minneapolis Oxygen Company, Grade 5.0 He, UN1046) was flowed over the sample pellet to purge any remaining air. To ensure that the Helium is moisture-free, Helium gas was flowed through a liquid nitrogen trap and desiccator before reaching the cell body. The initial spectrum of the calcined catalyst was measured at this time, with the background spectrum subtracted.

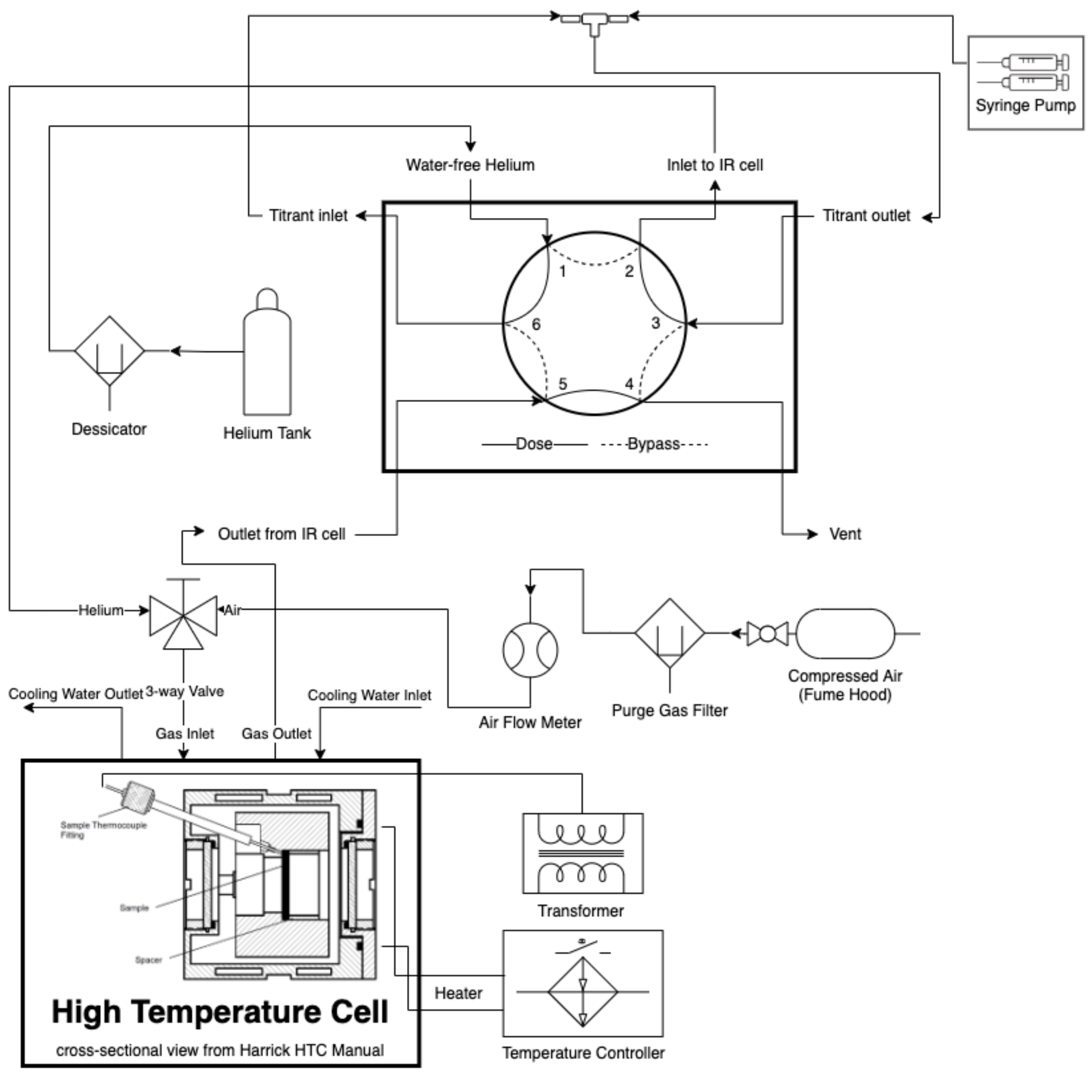

Figure 2-2. Schematic of Experimental Setup.

2.3 Materials Synthesis and Characterization

ZSM-11 (MEL-type), ZSM-5 (MFI-type), and FER-type zeolites were synthesized via seeded growth mechanism where rough fin-like features (with α dimensions of 30-50 nm) were created on the exterior surface of the seed crystals of β dimensions (400-500 nm). XRD, SEM, and TEM tomography confirmed the presence and sizes of these fins. Before each run, samples were calcined *in situ* in the High Temperature Cell (Harrick Scientific) at 500°C for 4 h in air (Linde, Air Ultra Zero) at a ramp rate of 1°C min^{-1}. After calcination, the sample was cooled down to and remained at 240 °C for the duration of the experiment to ensure the absence of water. See Section 3.2 One-pot synthesis of finned zeolites for more details on material synthesis and characterization.3.2 One-pot synthesis of finned zeolites

2.4 Data Analysis

The differential equation (Eq. 2-1) describing the temporal concentration gradient of molecule, C_A, in a spherical particle, is shown below:

$$\frac{\partial C_A}{\partial \mathrm{t}} = \mathfrak{D}\left[\frac{1}{r^2}\frac{\partial}{\partial \mathrm{r}}\left(r^2\frac{\partial C_A}{\partial \mathrm{r}}\right)\right] \qquad \text{2-1}$$

where $\mathfrak{D}$ is the diffusivity of gaseous phase *A*, with initial conditions as (Eq. 2-2):

$$C_A(r,\ t=0) = C_{A,0} \qquad \text{2-2}$$

and boundary conditions as (Eq. 2-3,4):

$$\left.\frac{\partial C_A}{\partial \mathrm{t}}\right|_{r=0,t} = 0 \qquad \text{2-3}$$

$$C_A(r=R,\ t) = C_{A,R} \qquad \text{2-4}$$

Applying the initial and boundary conditions to the governing equation results in Eq. 2-5:

$$\therefore \theta_A(t) = \frac{C_A}{C_{A,0}} = \left[e^{-\lambda_n^2 * \mathfrak{D} * t}\right] \qquad n = 1,2,\ldots \tag{2-5}$$

Thus, the relative percentage of BAS titrated can be described by Eq. 2-6**,**

$$\%\, BAS\ titrated = A * \left(1 - e^{-\lambda_n^2 * \mathfrak{D} * t}\right) \tag{2-6}$$

and simplified to the exponential model for seed particle (Eq. 2-7),

$$\%\, BAS\ titrated = A * \left(1 - e^{-\frac{t}{\tau_{seed}}}\right) \tag{2-7}$$

and similarly for finned samples (Eq. 2-8),

$$\%\, BAS\ titrated = A * \left(1 - e^{-\frac{t}{\tau_{seed}}}\right) + A_{fin} * \left(1 - e^{-\frac{t}{\tau_{fin}}}\right) \tag{2-8}$$

where τ_{seed}, and τ_{fin} are terms to describe diffusion time scales in the micropores of both bulk particles.

The procedure below was used to analyze temporal BAS titration data, which is attributed to 1565 cm^{-1} peak for 2,4,6-trimethylpyridine and 1555 cm^{-1} peak for 2,3-dimethylpyridine in the FTIR spectra. After integration of the respective peaks, the mean and standard deviation of three separate runs of the same sample were computed. A smoothing spline function was fitted using MATLAB over the run-averaged data. Discrete derivative between each data point were then taken of each run and the fit of the average run. The derivative, i.e. differential, plots were fitted with peak fitting function in MATLAB. Figures SX1 – SX4 show the corresponding plots for each step of this procedure for MEL-seed, MEL-finned, and SPP samples. See SI for full MATLAB codes that were used in this analysis.

2.5 Results and Discussion

FTIR spectra of ZSM-5 in the region of interests are shown in Figure 2-3. With the zeolite exposed only to Helium, the peak at 3605 cm^{-1} assigned to bridging hydroxyl groups indicate vacant Brønsted acid sites (BAS). After exposure to pyridine, often used to probe the overall number of Brønsted (BAS) and Lewis acid sites (LAS), the peak at 3605 cm^{-1} disappear completely, while the peak at 1545 cm^{-1} appears and increases in area, indicating the titration of the BAS by pyridine (Py-H+). Another common organic probe that is used is collidine, or 2,4,6-trimethylpyridine (TMPyr). The titration of BAS by TMPyr is shown in Figure 2-3 in red, where a slight shift from 1545 cm^{-1} to 1565 cm^{-1}, indicating trimethylpyridine-adsorbed Brønsted acid site (TMPyr-H+). Pyridine is a common FTIR probe in zeolite catalysis, as pyridine's kinetic diameter of 5 Å allows it to readily diffuse into MFI and MEL pores (~5.75 Å). Figure 2-3 shows the BAS titration over time of various adsorbates. Smaller adsorbates, such as pyridine and tert-butyl amine, readily saturate internal and external Brønsted acid sites within ~10 minutes. However, for TMPyr, with a slightly larger kinetic diameter of 5.75 Å, the timescale for complete titration increased by orders of magnitude (4000 minutes for TMPyr vs. 10 minutes for pyridine).

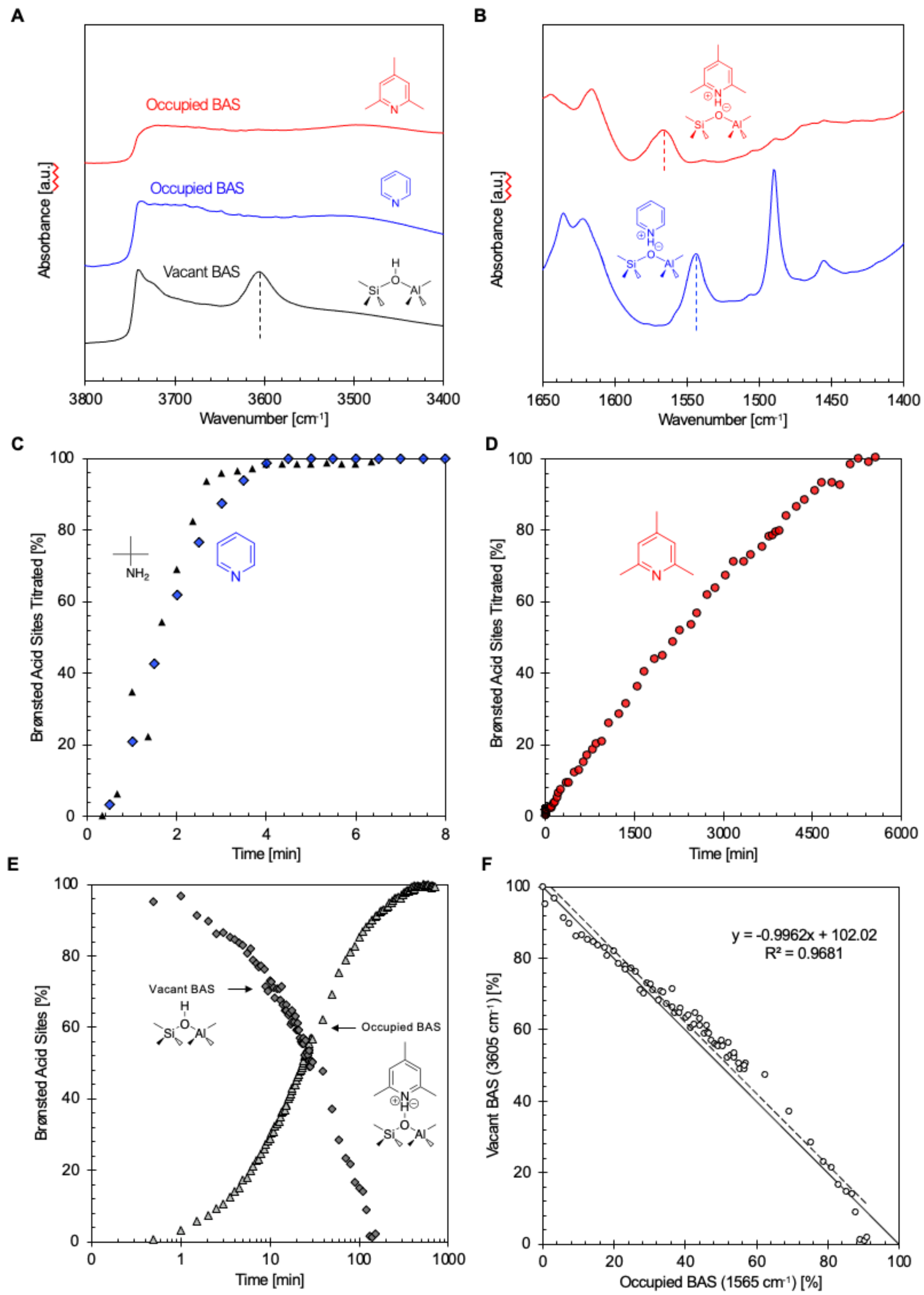

Figure 2-3. Brønsted Acid Site Titration with various probe molecules with FTIR Techniques in MFI.

(A,B) FTIR spectra of ZSM-5 (black), titrated with pyridine (blue), and 2,4,6-trimethylpyridine (red). (C,D) Sites titrated (%) versus time (min) of ZSM-5, with pyridine (blue), tertbutyl-amine (black) and 2,4,6-trimethylpyridine (red). (E) Peak areas of 3605 cm^{-1} (vacant sites) and 1565 cm^{-1} (occupied sites) over time. (F) Parity plot of peak areas of 3605 cm^{-1} and 1565 cm^{-1}, with slope of ~-1.

The slow diffusion of TMPyr through the MFI and MEL micropores is due to steric hindrance from the methyl groups. The temporal titration of TMPyr was quantified by the disappearance of the IR peak at 3605 cm^{-1} corresponding to the vacant Brønsted acid sites and also the appearance of 1565 cm^{-1} associated with trimethylpyridinium (TMPyr-H+) ion (Figure 2-4). Loss of Brønsted acid site was linearly correlated to increase in TMPyridinium ions (Figure SX1). At the termination of experiment, complete disappearance of 3605 cm^{-1} peaks is observed, corresponding to the saturation of all vacant BAS.

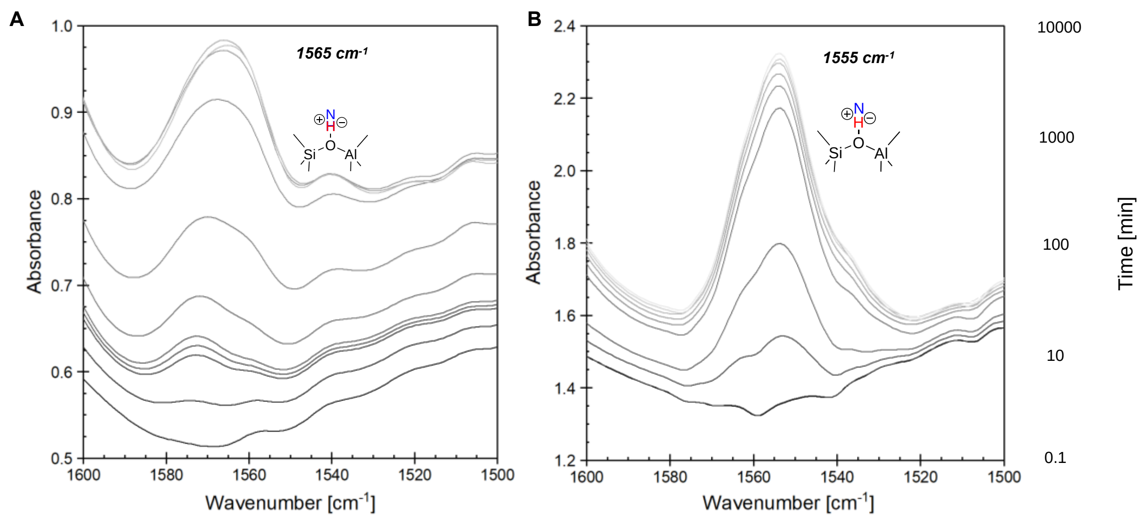

Figure 2-4. Temporal titration of Brønsted acid site by amines quantified by appearance of 1565 cm^{-1} and 1555 cm^{-1}.

For smooth samples without any rough exterior features, the initial increase in BAS uptake indicates adsorbed TMPyr on the external sites of the zeolite, limited by the diffusion of TMPyr in the gas phase in the boundary layer to the surface of the sample. From 10 min to 10^4 min, the slow diffusion time constants of TMPyr through the MFI and MEL smooth pores, τ_{seed}, were quantified to be of 10^5 s (Figure 3-4 Table Inset). Similarly for the MFI and MEL rough samples, we observe the slow diffusion time constants to be on the order of 10^5 s. However, the rough samples have a distinct fast uptake regime in the first ~100 min, where TMPyr was able to diffuse through the pores of the zeolites much more quickly. The fast diffusion time constants, τ_{fin}, were calculated to be 10^2 s, which is three orders of magnitudes faster than the slow diffusion time constants (Figure 3-4 Table Inset).

As the titration curves exhibit complex behavior that is not intuitively understandable, the inflection points, i.e. points of highest amine uptake for each diffusion regime, were further analyzed. The derivative, i.e. differential, of the titrated BAS over time was calculated and plotted (Figure 2-5). The derivative plot was obtained via the following procedure: fitting smoothing spline function over BAS titration over time, taking discrete derivative between each point, fitting the derivative plot with peak fitting function in MATLAB (Figure SX3). The derivative plots present a clearer picture of where most of the uptake were by fins vs. in the bulk zeolite, corresponding the time scales of diffusion with the length scales of the particle. Commercial samples, namely Zeolyst seed and finned of ZSM-5 and ZSM-11, exhibit the same phenomena with fast fin timescales and slow bulk timescales (Figure 3-4). Self-pillared pentasil (SPP) zeolite, which consists of uniform MFI hierarchical nanosheets, exhibit only one (fast) timescale, i.e. one diffusion regime that is slower than the diffusion through fins (Figure SX2).

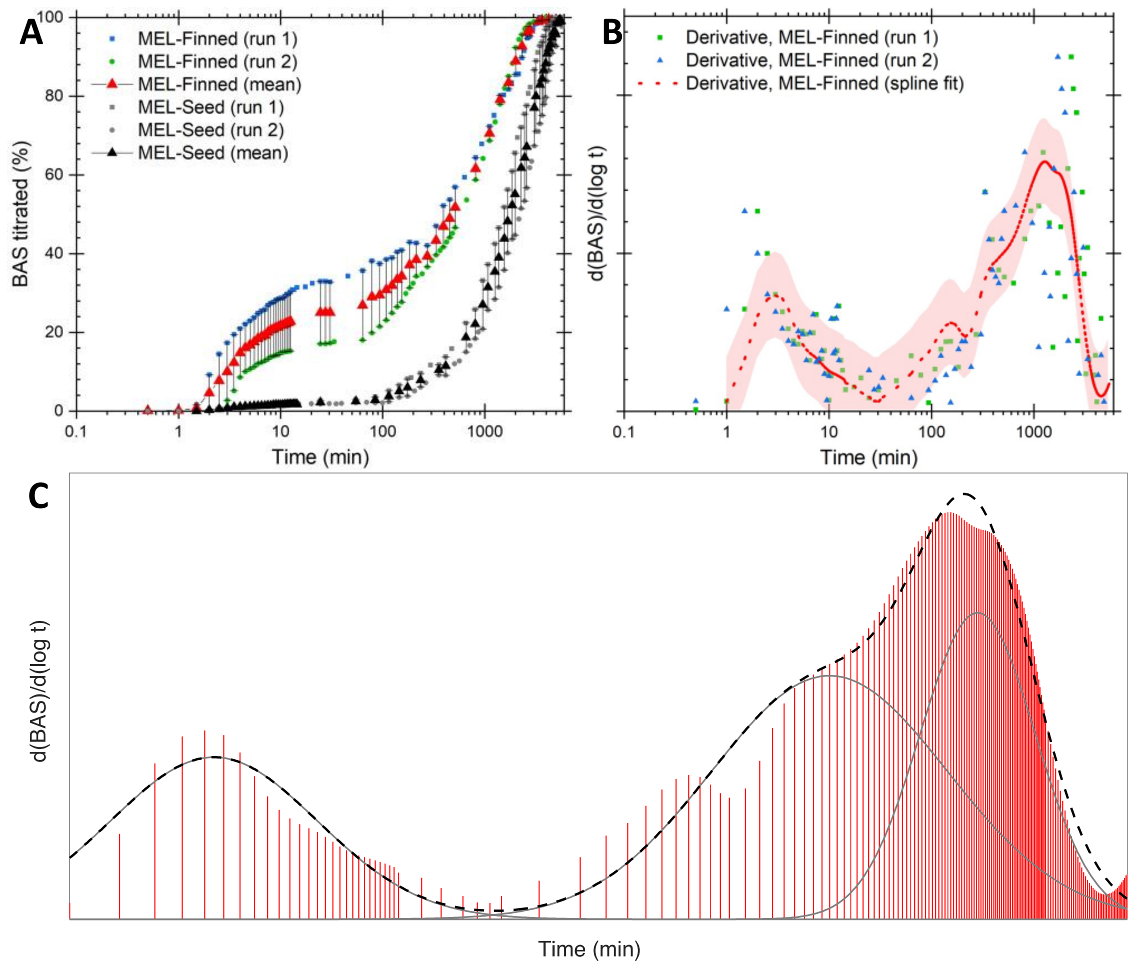

Figure 2-5. Derivative of Brønsted acid sites (BAS) titration by 2,4,6-trimethylpyridine over time.

The area under the peaks represent the cumulative amount of Brønsted acid sites titrated at different time point, with the first peak's maxima indicated by τ_{fp}, or peak at fast time-scale. The derivative plot was obtained via the following procedure - fitting smoothing spline function over BAS titration over time, taking discrete derivative between each point, fitting the derivative plot with peak fitting function in MATLAB.

The amine class was broadened to probe diffusion through two-dimensional zeolites with various pore sizes. The dimensionality of the system was reduced from 3-dimensional to 2-dimensional in order to deconvolute the multiple shouldering peaks in the differential titration curves due to multiple diffusion lengths. Ferrierite (FER), a 2-dimentional 8-MR and 10-MR zeolite, was chosen because it is also a commonly used industrial catalyst with commercial equivalent from Zeolyst. Similarly to MFI/MEL samples in the previous section, growth of fin-like protrusions on seed crystals resulted in enhanced catalyst lifetime in methanol-to-hydrocarbon (MTH) reactions. Expanding on the finned zeolite concept, the fin sizes were tuned, ranging from 30 to 50 nm, by preparation at different synthesis temperatures.

Figure 2-4 shows the FTIR spectra of 2,3-dimethylpyridine titration of Brønsted acid sites (DMPyr-H+) in FER samples. Similarly to TMPyr-H+, the 1555 cm^{-1} peak area increased over a period of 4000 minutes. DMPyr behaves similarly in FER seed vs finned zeolites, where the bulky organic base just fits into the FER pores. With the derivative data, the two time scales can be attributed to the two path length scales within the zeolite – one to fins, and the other to the bulk seed crystal. The area under the peaks represents the cumulative amount of Brønsted acid sites titrated at different time points, with the first peak's maxima indicated by τ_{fp}, or peak at fast time-scale (Figure 4-6). τ_{fp} was calculated for all FER samples and correlated well with the sizes of fins. When peak areas, representing the relative amount of BAS titrated in fins vs. seed, were plotted as a function of τ_{fp}, more fin volume and enhanced transport due to faster diffusion time scale directly correlated with catalyst lifetime and performance. Specifically, FER-F1 and FER-F2 have higher percentage of fin BAS and lower τ_{fp}, indicating enhanced transport of 2,3-dimethylpyridine.

2.6 Conclusion

The use of 2,4,6-trimethylpyridine (TMPyr) and 2,3-dimethylpyridine (DMPyr) were explored to probe internal diffusion of seed and finned zeolites. By strategically utilizing bulky amines as probe molecules in MFI, MEL, and FER-type zeolites, distinct diffusion regimes between the seed and fins were distinguished. An exponential model was fitted to BAS uptake, i.e. the amine adsorption on BAS over time. Across all zeolite samples employed in this study, seed crystals had amine diffusion time scales of 10^5s while fins had 2-3 orders of magnitudes faster diffusion time scales. Differential of titrated BAS over time was analyzed via MATLAB. The derivative plots of all samples exhibit distinct diffusion regimes: smooth zeolites had one bulk regime whereas finned zeolites had two regimes, a fast one attributed to fins and a slower one attributed to seed. By applying the technique on finned zeolites with varying fin sizes, further analysis of the derivative plots reveals relative percentage of fins and time scale of uptake by fins result in enhanced mass transport that can be correlated to enhanced catalyst performance and lifetime. In conclusion, the time-resolved IR technique presented in this work is an alternative, facile approach to assess mass transport properties of zeolites by correlating amine diffusion time scales and length scales. The technique has also been expanded to study core-shell and egg-shell zeolites with controlled BAS distribution within the samples. Future work includes broadening of amine class to probe one-dimensional zeolites as well as other zeotype catalysts.

Chapter 3 – Finned Zeolite Catalysts

*Reproduced with permission from H. Dai, Y. Shen, T. Yang, C. Lee, D. Fu, A. Agarwal, T. T. Le, M. Tsapatsis, J. C. Palmer, B. M. Weckhuysen, P. J. Dauenhauer, X. Zou, J. D. Rimer. Finned zeolite catalysts. *Nature Materials* **19**, 1074–1080 (2020).

3.1 Conspectus

There is growing evidence for the advantages of synthesizing nano-sized zeolites with markedly reduced internal diffusion limitations for enhanced performance in catalysis and adsorption. Producing zeolite crystals with sizes less than 100 nm, however, is nontrivial, often requires the use of complex organics, and typically results in small product yield. Here, we present an alternative, facile approach to enhance mass transport properties of zeolites by the epitaxial growth of fin-like protrusions on seed crystals. We validate this generalizable methodology on two common zeolites and confirm that fins are in crystallographic registry with the underlying seeds, and that secondary growth does not impede access to micropores. Molecular modeling and time-resolved titration experiments of finned zeolites probe internal diffusion and reveal substantial improvements in mass transport, consistent with catalytic tests of a model reaction showing that these unique structures behave as pseudo nanocrystals with sizes commensurate to that of the fin.

3.2 One-pot synthesis of finned zeolites

The confined channels and cages of microporous materials (zeolites) are utilized in numerous applications spanning from catalysis (*1, 2*) and adsorption (*3*) to selective separations (*4, 5*). A common objective in the design of zeolitic materials is to overcome the inherent mass transport limitations of micropores. This is a ubiquitous challenge for the development of zeolite catalysts where narrow pore apertures and long diffusion path lengths lead to more rapid deactivation owing to the accumulation of carbonaceous deposits (coke) (*6*). This is particularly true for zeolites with low-dimensional pore networks. There is an increasing body of literature showing how the preparation of nano-sized crystals can enhance catalyst lifetime and/or alter product selectivity (*7, 8*). For example, the advent of two-dimensional (*9, 10*) or self-pillared (*11*) zeolites with sizes on the order of a crystal unit cell (ca. 2 – 4 nm) exhibit superior catalytic performance to conventional zeolites; however, the preparation of these materials has only been demonstrated for a few framework types. Indeed, there is a relatively small number of reported zeolites with crystal sizes less than 100 nm, which highlights the challenges associated with synthesizing nano-sized microporous materials. This has motivated the development of alternative methods, such as the preparation of hierarchical materials (*12, 13*), where the introduction of mesopores has an analogous beneficial effect on mass transport. Practical challenges of nano-sized zeolite synthesis include the customary requirement of unconventional organics and the frequent drawback of small product yields. This underscores the need for more facile, efficient methods of producing nano-sized zeolites by methodologies that are generalizable to a broad number of framework types.

Here we investigate an alternative method of reducing internal diffusion limitations via the synthesis of zeolites with rough protrusions (size α) on their exterior surfaces (Figure 3-1A), which exhibit an identical crystallographic registry with the interior crystal (size β). These features resemble “fins” that are well known to enhance the rate of heat transfer in conductive materials owing to increased external surface area. Analogous to studies by Ryoo and coworkers (*10*) who showed that hierarchical zeolites possessing high external surface area markedly reduce external coking, we demonstrate a similar effect for finned catalysts, focusing on two common 3-dimensional medium-pore zeolites: ZSM-11 (MEL) and ZSM-5 (MFI). The synthesis of ZSM-11 using a previously reported protocol (*14*) yields crystals with relatively smooth exterior surfaces (fig. S1). We identified an alternative one-pot synthesis of ZSM-11 that produces crystals with finned surfaces (Figure 3-1, B and C). Transmission electron microscopy (TEM) reveals that these are single crystals (Figure 3-1D) with an identical registry between the center of the particle and the exterior fins. These exterior features are aligned in parallel with an average dimension of 35 nm (Figure 3-1E). Elemental analysis reveals no evidence of aluminum zoning (table S1) (*15*), which has been reported for ZSM-5 (*16*). Moreover, textural analysis (fig. S2) shows no evidence of mesoporosity in ZSM-11 samples, although TEM tomography reveals the presence of isolated pores within the interior of these particles (fig. S3 and movie S1), which is likely attributed to the nonclassical mechanism of zeolite growth involving particle attachment (*17, 18*).

Prior studies have reported rough crystals of ZSM-11 (*19*) and ZSM-5 (*20*). The majority of these examples are structures with distinctly different features than those reported here. Notably, rough crystals in literature are commonly aggregates with small crystallites arranged in random orientations on the exterior surfaces of larger particles (fig. S4). These misoriented domains can give rise to pore blockage at the interfacial boundaries between adjacent particles; however, prior studies have demonstrated that these aggregated structures enhance overall catalytic performance relative to conventional analogues, which is attributed to the introduction of interstitial mesopores (*21*). Here, we show that the one-pot synthesis of finned ZSM-11 improves catalyst properties owing to a different mechanism: enhanced mass transport through fins of much smaller dimension (i.e. $\alpha \ll \beta$). Shen et al. (*14*) previously reported trends in catalyst lifetime and selectivity as a function of H-ZSM-11 crystal size (150, 300, and 750 nm) using methanol-to-hydrocarbons (MTH) as a model reaction. Time-on-stream conversion over these three catalysts are compared to the finned H-ZSM-11 sample (Figure 3-1F), which has an overall size of ca. 460 nm that includes the fins. Interestingly, the finned catalyst deviates from the trend of increasing lifetime with decreasing crystal size when comparisons are made on the basis of overall particle dimension; however, the trend is qualitatively consistent if the finned catalyst behaves as a crystal of much smaller size, commensurate with that of the average fin dimension (α = 35 nm).

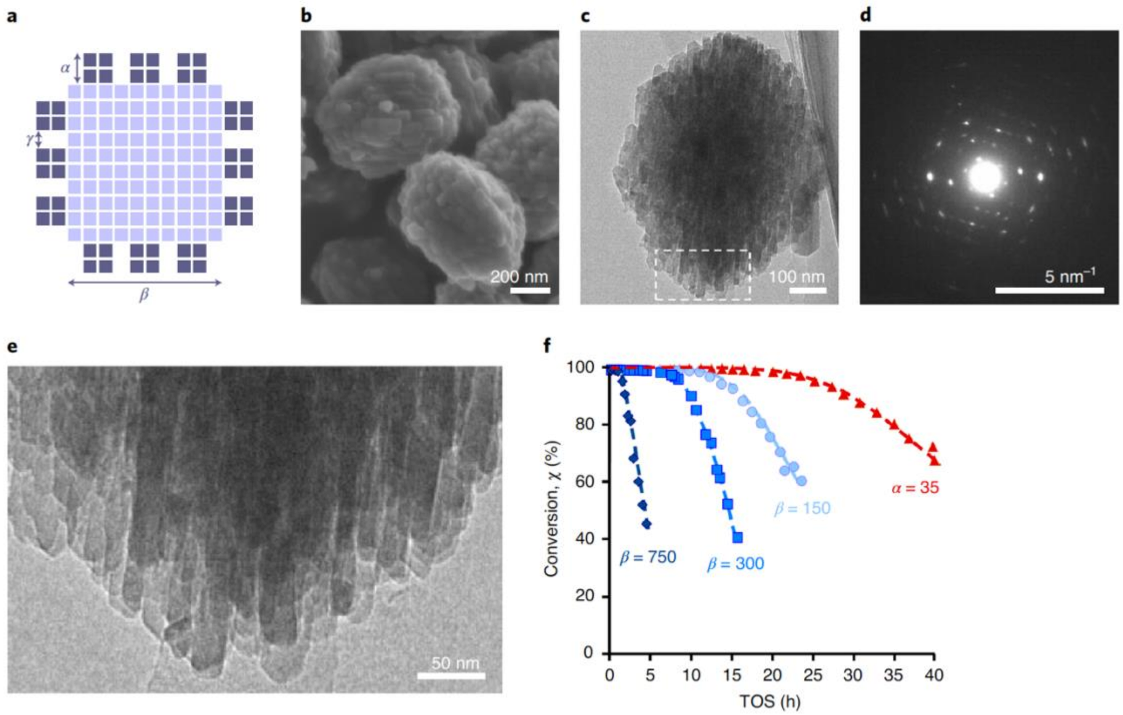

Figure 3-1. One-pot preparation of finned ZSM-11.

(A) Idealized schematic of a finned zeolite with fin and interior dimensions of α and β, respectively, and fin pitch γ. (B) Scanning electron micrograph of zeolite ZSM-11 crystals with finned surfaces prepared from a one-pot synthesis. (C) Transmission electron micrograph of a representative finned ZSM-11 crystal. (D) Corresponding SAED pattern of the crystal in panel C showing a single-crystal pattern behavior. (E) High magnification TEM image from panel C (dashed box) showing the parallel alignment of fins. (F) Time-on-stream methanol-to-hydrocarbons (MTH) conversion for H-ZSM-11 catalysts (Si/Al ~ 20) at 350 °C with WHSV = 9 h-1. The performance of finned H-ZSM-11 with an overall size of 460 nm (fins $\approx$ 35 nm) is compared to conventional H-ZSM-11 crystals with sizes of 750 nm (diamonds), 300 nm (squares), and 150 nm (circles). Dashed lines are interpolations to guide the eye.

3.3 Preparation of finned zeolites by secondary growth

The preparation of finned zeolite crystals via a one-pot synthesis is arbitrary and difficult to predict owing to the largely unknown impact of synthesis parameters on zeolite crystallization. To this end, secondary (or seeded) growth offers a more controlled method of creating fins on the exterior surfaces of seed crystals. Here we demonstrate the secondary growth method for both ZSM-11 (Figure 3-2, A – D) and ZSM-5 (Figure 3-2, E – H). Scanning electron microscopy (SEM) images of ZSM-11 (Figure 3-2A) and ZSM-5 (Figure 3-2E) seeds reveal exterior crystal surfaces devoid of rough features. SEM images after secondary growth of ZSM-

11 (Figure 3-2B) and ZSM-5 (Figure 3-2F) confirm the presence of fins (protrusions). TEM images show average feature sizes of 30 ± 3 nm for ZSM-11 (Figure 3-2C) and 53 ± 6 nm for ZSM-5 (Figure 3-2G). Selected area electron diffraction (SAED) patterns (Figure 3-2, D and H) also confirm that the samples are single zeolite crystals, thus indicating that the fins grow epitaxially on the surfaces of the seeds. Powder X-ray diffraction (XRD) patterns indicate the samples are fully crystalline before and after seeded growth (fig. S5 and fig. S6), while textural analysis (table S3 and fig. S7) shows a slight increase in total surface area (ca. 8%) with secondary growth without an appreciable change in micropore volume. Elemental analysis (table S3) also confirms that the Si/Al ratio of the samples before and after seeded growth are nearly identical.

The protocol for generating finned zeolites (see Methods in Appendix) was strategically selected by adjusting the supersaturation to a level that was sufficiently high to avoid layer-by-layer growth of core-shells (i.e. complete overgrowth of seed crystals), which was previously demonstrated by Ghorbanpour et al. (*22*). However, there is an upper limit of supersaturation that, when exceeded, leads to homogeneous nucleation of new crystals in the growth solution, thereby generating aggregates of both small and large crystallites. TEM tomography of finned ZSM-11 (Figure 3-2I and movie S2) and ZSM-5 (Figure 3-2J and movie S3) after secondary growth confirms the absence of intraparticle mesoporosity. Cross-sectional transmission electron tomography images of each sample along the z-direction (z stacks), depicted in Figure 3-2I and Figure 3-2J at the bottom, middle, and top of the particles, clearly show the size and distribution of fins on the exterior surfaces. The finned zeolites prepared by secondary growth (Figure 3-2K) are comprised of regions with two characteristic dimensions: β is the size of the original seed along the principal zone axis of diffusion (i.e. *b*-directions for MFI and MEL) and α is the average size of fins. An idealized schematic of finned zeolites (Figure 3-2L) shows medium-pore channels extending from interior to exterior with identical registry.

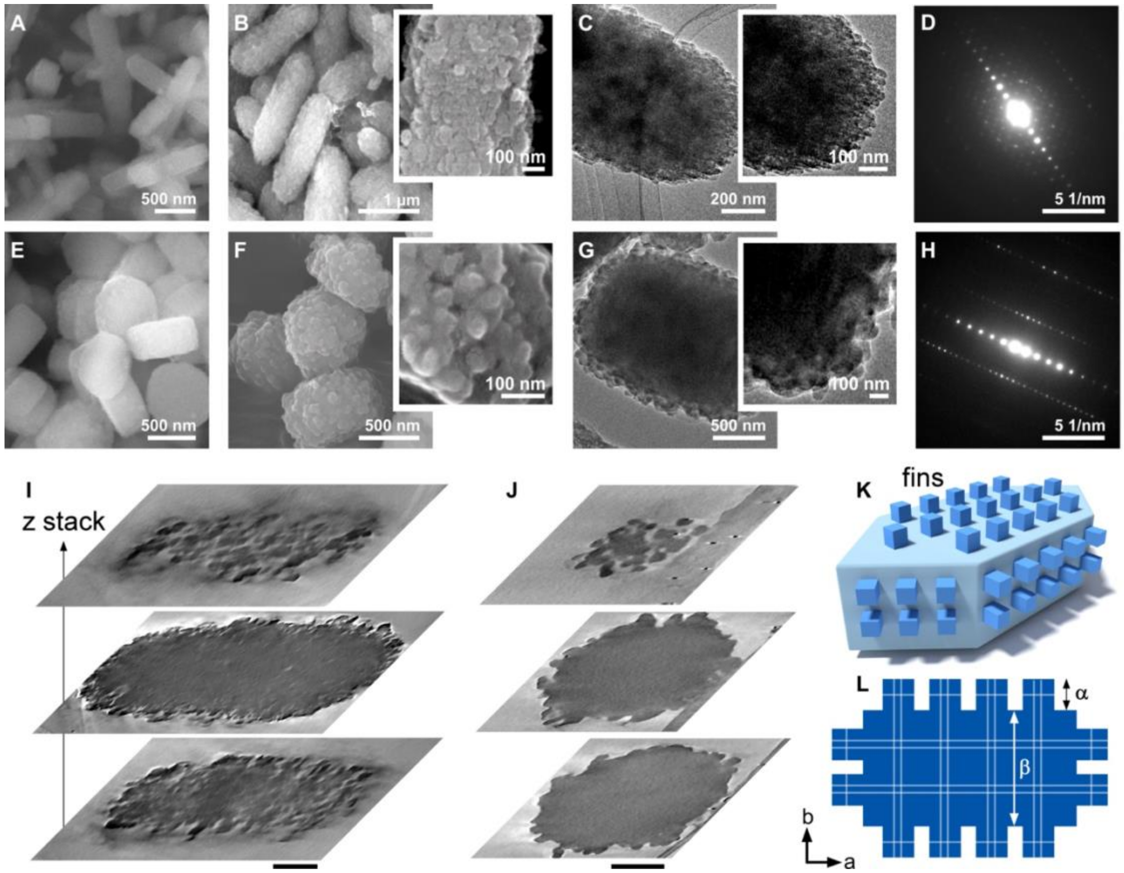

Figure 3-2. Electron micrographs of zeolite (A – D) ZSM-11 and (E – H) ZSM-5 crystals.

Comparisons are made between seeds prepared by conventional protocols (A and E) and finned crystals (B – D; F – H) prepared by secondary growth of the seeds. SAED patterns (D and H) reveal that the finned zeolites are single crystals. (I and J) TEM tomography images of finned (I) ZSM-11 and (J) ZSM-5 crystals showing cross-sectional images. Scale bars equal 200 nm. (K) Idealized schematic of a finned zeolite where the fins have the same crystallographic registry as the seed. (L) Illustration of a finned zeolite comprised of continuous channels throughout the seed (with characteristic size β) and fins (with characteristic size α).

3.4 Impact of fins on catalyst performance

To substantiate the enhanced mass transport properties of zeolites after secondary growth, we assess the performance of acid-exchanged (H-form) seed and finned samples in the MTH reaction at sub-complete methanol conversion (60 – 90%). The acid site density and the framework Al of each catalyst was quantified (table S3 and fig. S8) to ensure a consistent weight hourly space velocity (WHSV). Time-on-stream (TOS) analysis of both seed and finned H-ZSM-11 (Figure 3-3A) and H-ZSM-5 (Figure 3-3B) samples reveal similar catalyst activity (i.e. nearly identical starting conversion). This suggests that reactions in finned samples are not solely restricted to the exterior protrusions, but also occur within the interior of the catalyst. This is qualitatively consistent with TEM and textural analyses showing the epitaxial growth of fins without noticeable obstruction of pores at the fin-seed boundary. For both crystal topologies, we observe an approximate 3-fold reduction in the rate of deactivation, thus confirming the presence of fins markedly extends catalyst lifetime. Moreover, comparison of product selectivities (Figure 3-3C and Figure 3-3D) reveals a subtle shift whereby finned zeolites, which seemingly behave as pseudo nano-crystallites of dimension α, promote the olefin-based cycle of the MTH hydrocarbon pool (HCP) mechanism (*23*). Prior studies have shown a progressive shift in the preferred cycle (from aromatic to olefin) with decreasing crystal size (*24*). This is clearly evident when comparing the conventional descriptor *ethylene/2MBu*, which is a ratio of signature products from the aromatic-based cycle (ethylene) and olefin-based cycle (2MBu = 2-methylbutane and 2-methyl-2-butene). Over the entire range of methanol conversion we observe a noticeable reduction in the ethylene/2MBu ratio of finned catalysts (Figure 3-3E), which agrees with the expected trend for smaller particles.

MTH reactions were repeated using *operando* UV-Vis diffuse reflectance spectroscopy (DRS) coupled with on-line gas chromatography to track the spatiotemporal progression of the formation of hydrocarbon species in the zeolite crystals. It was previously shown (*25*) that a UV-Vis spectrum, obtained during MTH catalysis, can be grouped into three distinct regions of wavelengths corresponding to HCP species as well as small and large polyaromatics. HCP species are reaction products small enough to diffuse through zeolite pores; small polyaromatics are associated with internal coke given that their size is sufficiently large to fit within zeolite pores, but too large to diffuse out of the zeolite; and large polyaromatics are attributed to external coke. The UV-Vis spectra for H-ZSM-11 (Figure 3-3F) reveal equivalent internal coke between seed and finned samples; however, there is a noticeable reduction in the quantity of external coke for the finned sample, suggesting the presence of external protrusions leads to less accumulation of polyaromatics at pore mouths. A similar trend was observed for

H-ZSM-5 samples (Figure 3-3G), but with shorter lifetime owing to the tortuous sinusoidal channels of MFI compared to the straight channels of MEL (insets of Figure 3-3A and Figure 3-3B). Collectively, these studies indicate that finned catalysts enhance mass transport properties of the zeolite by suppressing the formation of external coke. This seemingly implies that olefins and small aromatics more readily diffuse through the fins, leading to reduced residence time of HCP species near pore mouths.

One advantage of the finned synthesis approach is that it is theoretically applicable to a wide range of framework types. Moreover, this approach can be used to upgrade commercial catalysts via the addition of a secondary growth step. As proof of principle, we have performed a seeded growth experiment using a commercial ZSM-5 sample from Zeolyst (CBV5524G, Si/Al = 25). Electron micrographs of as-received H-ZSM-5 reveal a heterogeneous particle size distribution with dimensions spanning from 100 to 250 nm (Figure 3-3H and fig. S11). Secondary growth of these particles successfully generates finned H-ZSM-5 with $\alpha = 35 \pm 5$ nm (Figure 3-3I and fig. S11). Elemental analysis (table S5) also confirms that the Si/Al ratio of the samples before and after seeded growth are nearly identical. MTH reactions at complete methanol conversion over as-received and finned catalysts reveal that the latter exhibits longer lifetime (Figure 3-3J) with expected trends in product selectivity (fig. S12), analogous to the synthetic seed and finned samples. It should be noted that the preparation of ZSM-5 with high Al content (Si/Al = 15 – 25) and sizes ranging from 2 nm (2D materials) to 100 nm (commercial samples) is largely inaccessible by conventional synthesis routes; however, the synthesis of finned zeolites offers a new route to achieve pseudo-crystallites within this largely inaccessible size range.

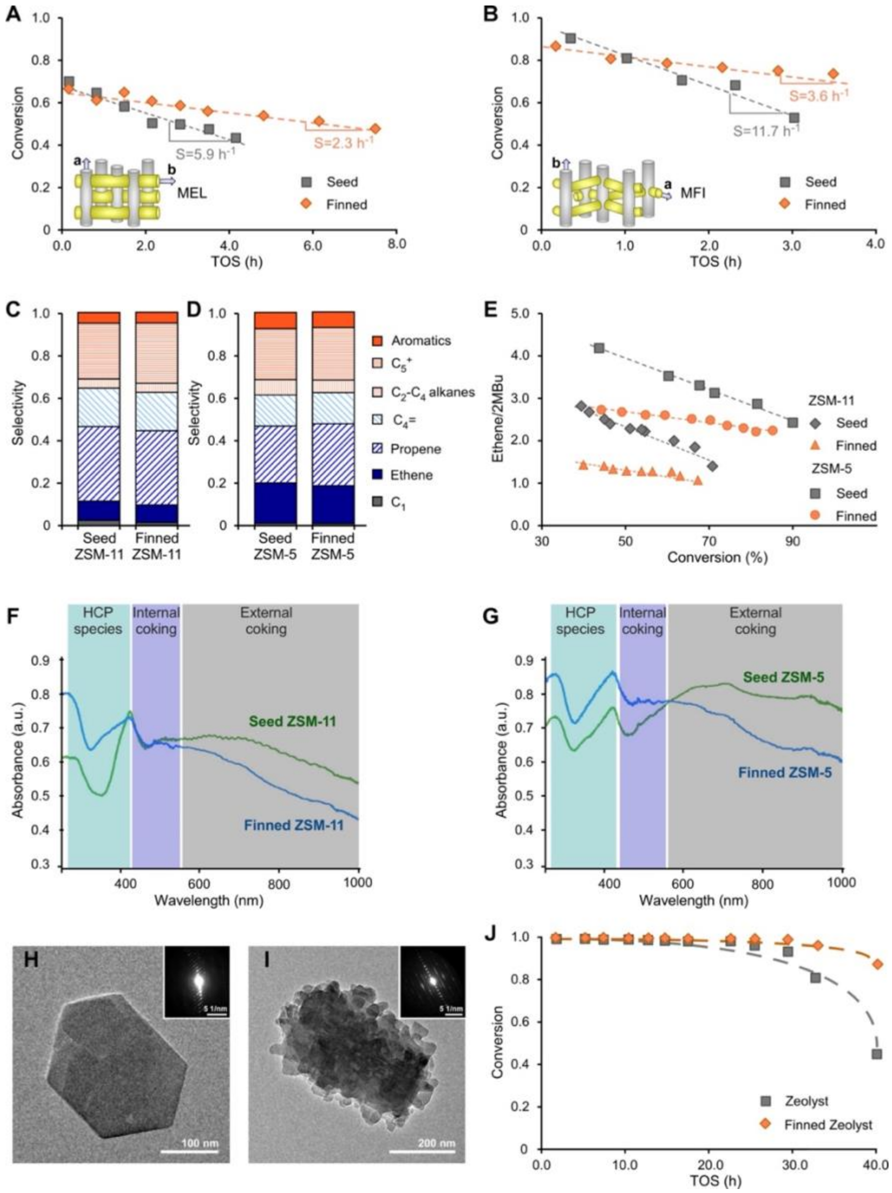

Figure 3-3. Plots of sub-complete methanol conversion over zeolite (A) H-ZSM-11 and (B) H-ZSM-5 catalysts during MTH catalysis as a function of time-on-stream.

Comparisons are made between seed (grey squares) and finned (orange diamonds) samples during the MTH reaction at 350 °C with WHSV = 20 h^{-1}. Insets: schematics of MEL and MFI frameworks, respectively. (C and D) Selectivities of hydrocarbon products for seed and finned (C) H-ZSM-11 and (D) H-ZSM-5 samples (assessed at a methanol conversion of 60 – 90%). (E) Ratio of ethylene to 2MBu (2-methylbutane and 2-methyl-2-butene) for the four set of samples. (F and G) *Operando* UV-Vis diffuse reflectance spectroscopy after 4 h TOS for (F) H-ZSM-11 and (G) H-ZSM-5 catalysts at the same reaction conditions. Comparisons are made between seed (green) and finned (blue) samples. The shaded regions correspond to distinct hydrocarbon species. (H and I) TEM images and SAED patterns of (H) a typical commercial zeolite H-ZSM-5 crystal (Zeolyst CBV5524G) and (I) a typical crystal of the corresponding finned material prepared by secondary growth. (J) Time-on-stream methanol conversion over as-received and finned commercial H-ZSM-5 during the MTH reaction at 350 °C with WHSV = 9 h^{-1}.

3.5 Mass-transport properties of finned zeolites

To confirm whether finned zeolites exhibit distinct mass transport properties relative to conventional (seed) zeolites, we performed kinetic Monte Carlo (kMC) simulations to compare diffusive behavior of benzene (a relatively bulky, representative hydrocarbon molecule) in silicalite-1 (MFI), the siliceous isostructure of ZSM-5, with preset α and β dimensions. The schematic in Figure 1A, which is not drawn to full scale, is a cross-section of the three-dimensional model used in the kMC simulations where each square represents a unit cell of silicalite-1 (unit cells belonging to the seed and fins are colored light and dark blue, respectively). The simulated model contains ~10^7 unit cells. Benzene transports through the pore network of silicalite-1 via a series of infrequent hops between favorable adsorption sites in the framework's straight pores (*S*), sinusoidal channels (*Z*), and at their intersections (*I*) (Figure 3-4A – C), which can be described by first-order kinetics. The kMC simulations of benzene hopping dynamics in silicalite-1 using rate constants from molecular modeling yield diffusivity estimates (table S6) that are in good agreement with experiment (*26, 27*). We use this modeling approach to estimate the diffusion path length r, defined as the total trajectory length of a benzene molecule between first entrance and exit of the zeolite crystal, for seed and finned superstructures created by replication of the periodic MFI unit cell. For a seed crystal (β = 500 nm), the mean diffusion path length for benzene is $\langle r \rangle = 137\ \mathrm{nm}$, corresponding to a characteristic residence time of $\langle \tau \rangle = 1.91 \times 10^{-5}\ s$ (Figure 3-4D and table S7). When the surface is decorated with fins (α = 50 nm) with a fixed pitch γ of 10 nm, we obtain $\langle r \rangle = 57$ nm and $\langle \tau \rangle = 0.79 \times 10^{-5}\ s$ (Figure 3-4D and table S7). This 2.4-fold reduction arises from the comparatively shorter distance required for diffusing molecules to enter and exit through the fins, relative to the seed crystal. Although the magnitude of the improvement depends on the fin surface density (table S7), kMC simulations show that the finned structures exhibit superior mass transport characteristics, consistent with experimental observations.

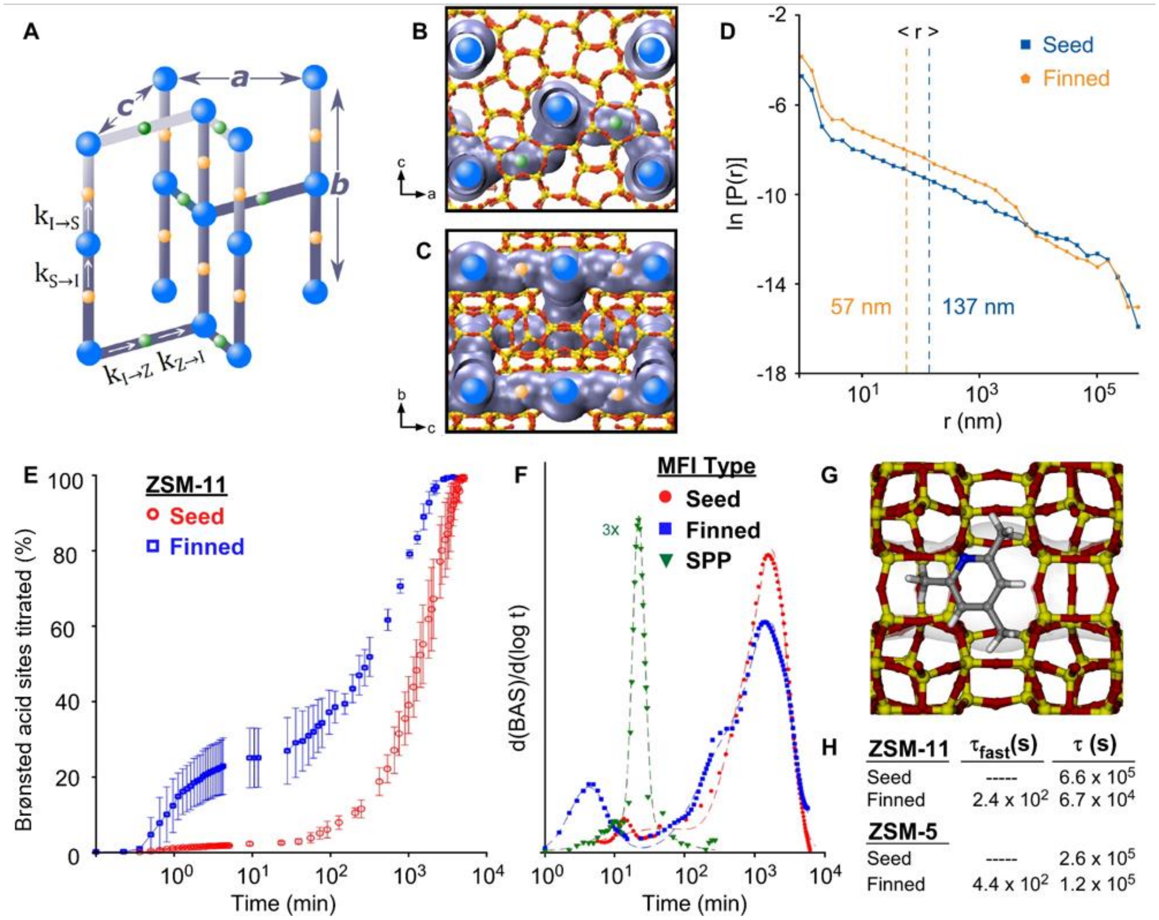

Figure 3-4. Enhanced mass-transport properties of finned zeolites.

(A – C) Molecular simulations of benzene diffusion in a finned Si-MFI structure. (A) Kinetic Monte Carlo lattice representation of the pore network for the MFI unit cell. Favorable adsorption sites in the straight pores (*S*), sinusoidal channels (*Z*), and at their intersections (*I*) are labelled as orange, green, and blue spheres, respectively. (B and C) Renderings along the (B) *b*-direction and (C) *a*-direction showing the kMC pore network superimposed on an atomistic unit cell. (D) Log probability density distribution of benzene diffusion path length *r* for a finned zeolite (β = 500; α = 50; γ = 10; see Figure 3-1) and a seed crystal with cubic geometry (β = 500 nm). Dashed vertical lines mark the mean diffusion path lengths $\langle r \rangle$ of 57 and 137 nm for the finned and seed crystals, respectively. Dashed vertical lines mark the mean diffusion path lengths $\langle r \rangle$ of 57 and 137 nm for the finned and seed crystals, respectively. (E - H) Time-resolved titration of Brønsted acid sites by TMPyr was monitored by FTIR spectroscopy. (E) Time-resolved titration of Brønsted acid sites for H-ZSM-11 seed and finned samples. (F) Differential plot of titrated Brønsted acid sites in Zeolyst ZSM-5 seed/finned samples and self-pillared pentasil (SPP), with peak fitting procedure shown and plots of additional samples shown in the appendix. (G) Snapshot from a molecular dynamics simulation showing TMPyr within a MEL channel. (H) Fast (τ_{fast}) and slow (τ) diffusion time constants from exponential models of TMPyr titration curves.

The enhanced mass transport properties of finned zeolites were further verified using a new experimental protocol for assessing internal diffusion based on time-resolved FTIR spectroscopy. In these studies, the purified bulky organic base 2,4,6-trimethylpyridine (TMPyr) is used to titrate Brønsted acid sites (BAS) within zeolite micropores (see Methods and fig. S18 in Appendix for details). Diffusion and adsorption of TMPyr slowly permeates the micropores of H-ZSM-11 and H-ZSM-5 over 72 h due to steric hindrance from the methyl groups (*28*). The temporal permeation of TMPyr was quantified by the disappearance of FTIR intensity at 3605 cm^{-1} corresponding to the vacant Brønsted acid sites and also the appearance of peaks at 1565 cm^{-1} associated with the trimethylpyridinium ion (fig. S13). Loss of Brønsted acid sites is linearly correlated to the increase in TMPyridinium ions (fig. S17). The distinct TMPyr uptake kinetics for H-ZSM-11 (Figure 3-4E) and H-ZSM-5 (fig. S14), both with and without fins, are described by an exponential diffusion model. When the differential of the titrated Brønsted acid sites over time is plotted for the Zeolyst samples (Figure 3-4F) and other zeolites (fig. S15), we observed the two distinct diffusion regimes, indicating the initial fast uptake of TMPyr in the fins relative to the bulk particle. To further assert the correspondence of the two time scales to the finned and bulk portions of the crystals, we also applied the method to examine a self-pillared pentasil (SPP) zeolite, which consists of intergrown few-nm thick MFI nanosheets (i.e., it has a uniform micro-/mesopore hierarchical structure throughout each particle), and as such it should exhibit only one (fast) time scale. Indeed, we obtained one diffusion regime albeit somewhat slower than the fast one obtained in the finned samples indicating possible contributions of mesopore resistances in SPP (Figure 3-4F). Molecular dynamics simulations also confirm that TMPyr is of sufficient size to fit within the channels of both MEL (Figure 3-4G) and MFI (fig. S16) frameworks.

Experimental points in TMPyr titration curves were fitted using an exponential model (see Supplementary Text in Appendix) to obtain time constants for fast (τ_{fast}) and slow (τ) diffusion within the finned and interior micropore regions, respectively (Figure 3-4H and table S8). The finned zeolites exhibit initial rapid uptake kinetics three orders of magnitude faster than the seed. These trends are qualitatively consistent with kMC models and catalytic studies showing distinct transport properties of finned zeolites where the introduction of protrusions with size $\alpha \ll \beta$ markedly reduce internal diffusion limitations. Time-resolved titration measurements also reveal that this disparity in time constants is maintained for nanocrystals where the differences between α and β are less substantial (e.g. Zeolyst H-ZSM-5 in Figure 3-3H and Figure 3-3H I).

Conventional zeolite synthesis methods cannot readily produce MFI and MEL crystal sizes in the range of 10 – 80 nm. Conversely, methods of producing 2D crystals with sizes less than 10 nm often result in insufficient acid site density (e.g. Si/Al > 40) for industrial hydrocarbon catalysis. Moreover, ultrasmall crystallite sizes pose practical challenges for solids extraction in commercial synthesis processes. The generation of finned zeolites overcome these restrictions and challenges by altering the performance of large crystals to behave as pseudo-nanocrystals. Using a synergistic combination of state-of-the-art experimental techniques, we show that finned ZSM-5 and ZSM-11 zeolites possess unusually outstanding mass transport properties. Markedly enhanced rates of molecular uptake in fins, coupled with reduced internal diffusion path lengths, leads to less coke formation on external surfaces, longer catalyst lifetime, and a shift in product selectivities that are characteristic of zeolites with an overall crystal size equal to that of the average fin dimension. The ability to introduce fins through a facile secondary growth process is a new method to reduce diffusion limitations in zeolites. Here, we demonstrate that this approach can be used to enhance the performance of commercial catalysts, with the promise of becoming a generalized platform for the rational design of zeolites across a broad range of framework types.

Chapter 4 – Enhanced Selectivity and Stability of Finned Ferrierite Catalysts in Butene Isomerization

*Reproduced with permission from H. Dai, C. Lee, W. Liu, T. Yang, J. Claret, X. Zou, P. J. Dauenhauer, X. Li, J. D. Rimer. Enhanced Selectivity and Stability of Finned Ferrierite Catalysts in Butene Isomerization. *Angewandte Chemie* **Volume 61**, Issue 8 (2022).

4.1 Conspectus

Designing zeolite catalysts with improved mass transport properties is crucial for restrictive networks of either one- or two-dimensional pore topologies. Here, we demonstrate the synthesis of finned ferrierite (FER), a commercial zeolite with two-dimensional pores, where protrusions on crystal surfaces behave as pseudo nanoparticles. Catalytic tests of 1-butene isomerization reveal a 3-fold enhancement of catalyst lifetime and an increase of 12% selectivity to isobutene for finned samples compared to corresponding seeds. Electron tomography was used to confirm the identical crystallographic registry of fins and seeds. Time-resolved titration of Brønsted acid sites confirmed the improved mass transport properties of finned ferrierite compared to conventional analogues. These findings highlight the advantages of introducing fins through facile and tunable post-synthesis modification to impart material properties that are otherwise unattainable by conventional synthesis methods.

4.2 Introduction

The confined channels and cages of zeolites and zeotypes have been widely used as shape-selective catalysts and absorbents in numerous commercial processes due to their unique properties, such as (hydro)thermal stability, tunable acidity, and versatile pore topologies[1]. A common objective in the design of zeolite catalysts is overcoming the inherent mass transport limitations of micropores. Advancements in the synthesis of two-dimensional (2D)[2], self-pillared[3], hierarchical (e.g. mesoporous)[4], and nanosized[5] zeolites have revealed their superior catalytic performance relative to conventional analogues owing to reduced internal diffusion pathlength and increased external surface area (i.e. more accessible acid sites). The majority of these advancements have focused on the optimization of zeolites with three-dimensional pores; however, the frameworks with the most restrictive mass transport are zeolites with one- and two-dimensional pore networks. Methods to optimize one-dimensional materials include post-synthesis modification to introduce mesopores[6] or relatively few cases where the judicious selection of synthesis parameters leads to nanosized crystals[7]. Two-dimensional zeolites are either layered materials[8] or structures that are amenable to the generation of nanosheets[9] with thicknesses less than a few unit cells of the crystal structure; however, diffusion is orthogonal to these directions where the enhanced external surface area promotes reactions involving bulky (sterically-hindered) molecules but does little to mitigate internal diffusion limitations.

In this study, we examined the synthesis and catalytic performance of ferrierite (FER), which is a two-dimensional zeolite with interconnected small 8-membered ring (MR, 3.5×4.8 Å) and medium 10-MR (4.2×5.4 Å) pore apertures (Figure 4-1). Ferrierite is a commercial catalyst that is used in isomerization[10] and other reactions[11] owing to its unique pore topology that includes intersections of two disparate pore sizes and cavities within the smaller channels that can promote shape-selective reactions. Restricted diffusion through two-dimensional pores makes ferrierite more susceptible to rapid deactivation from coke formation (i.e. pore blockage)[12]. To our knowledge, ferrierite crystals have not been synthesized with dimensions less than 100 nm in both the b- and c-directions (parallel to 8- and 10-MR pores, respectively). There have been examples where particles (or aggregates of particles) comprised of smaller domains or protrusions with dimensions less than 100 nm have been synthesized via the judicious selection of organic structure-directing agents (OSDAs). Corma and coworkers[11] produced ferrierite catalysts with a length of 10–30 nm using two cooperative OSDAs and reported an enhanced lifetime in 1-pentene oligomerization. Hong and coworkers[10] synthesized needle-like ferrierite crystals with sizes of ca. 10 nm using choline as the OSDA; and Xiao and coworkers[10] reported an alternative OSDA capable of inhibiting growth in the *a*-direction to generate ultrathin nanosheets (6–8 nm in the direction orthogonal to diffusion). Other studies have successfully synthesized ferrierite crystals with sizes on the order of 100 nm[10]. Alternative techniques include post-synthesis treatment (e.g. delamination) of layered FER precursor (PREFER)[13] or the generation of hierarchical structures by dealumination or desilication[10,14]. However, the latter methods reduce micropore volume and can often result in the loss of crystallinity.

We recently discovered a new class of hierarchical ZSM-5 (MFI) and ZSM-11 (MEL) catalysts referred to as “finned” zeolites[15]. It was demonstrated for these three-dimensional zeolites that the epitaxial mass-transport properties and catalyst lifetime in the methanol-to-hydrocarbon (MTH) reaction. Here, we extend this general concept to the synthesis of ferrierite and test the hypothesis that ultrasmall fins (< 50 nm) on this two-dimensional zeolite markedly enhance catalyst turnovers and product selectivity. Our findings revealed that ferrierite crystals can be prepared with tunable fin size to transform seeds into growth of fin-like protrusions on seed crystals dramatically enhanced pseudo nanoparticles with improved mass transport properties. This phenomenon was validated for both synthetic and commercial ferrierite where we observed that the introduction of fins leads to sizable increases in catalyst turnovers and isobutene selectivity compared to their non-finned counterparts.

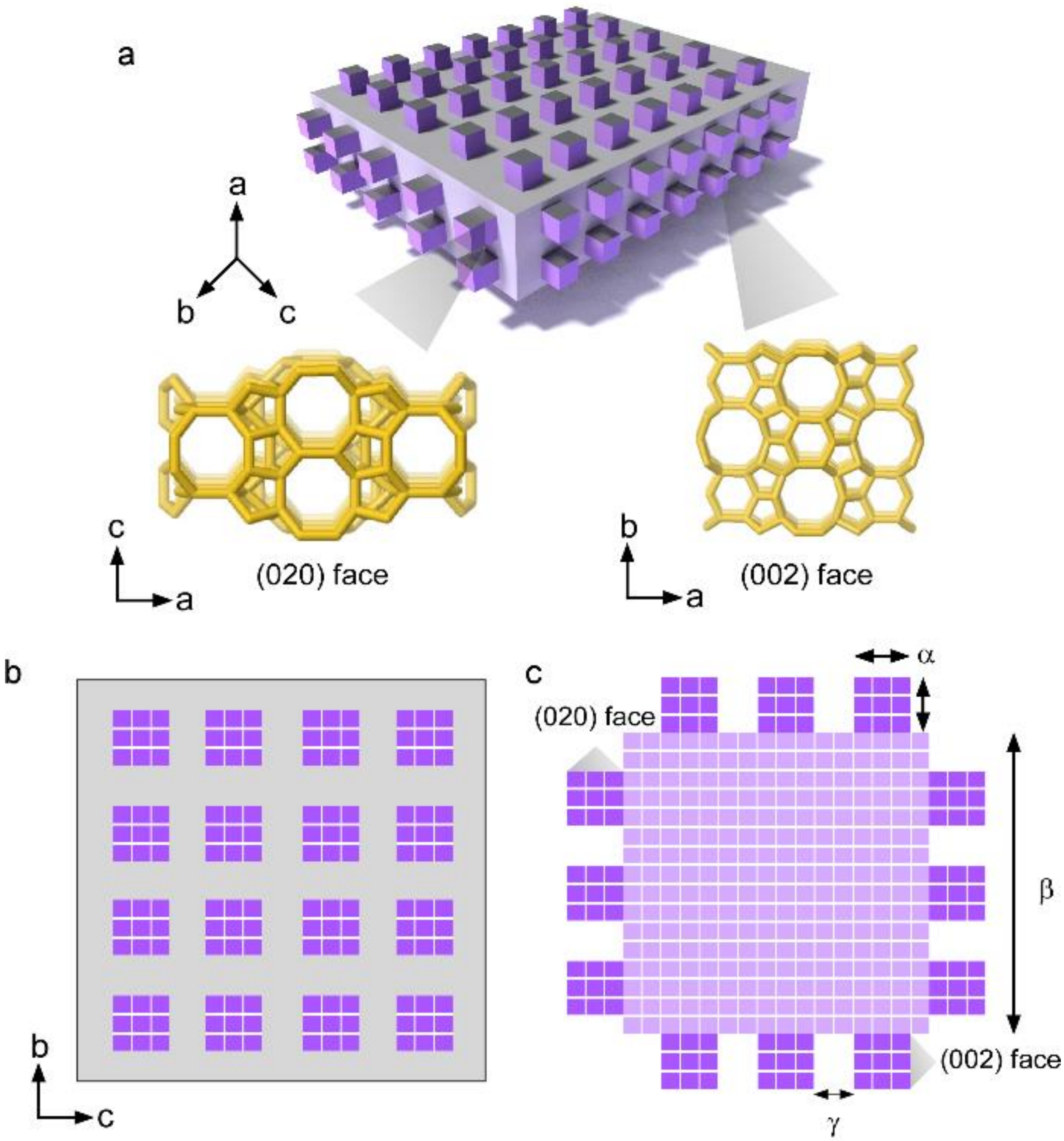

Figure 4-1. Idealized structure of finned ferrierite.

(a) Scheme of a finned ferrierite (FER) zeolite where the fins have the same crystallographic registry as the seed (*Immm* space group with unit cell parameters, a = 19.02 Å, b = 14.30 Å, c = 7.54 Å, α = β = γ = 90°). The FER topology comprises two-dimensional pores with 8-membered ring channels oriented in the [020] direction and 10-membered ring channels oriented in the [002] direction. In the scheme, grey and purple shaded regions represent nonporous and porous faces, respectively. (b) Fins located on basal (200) facets are isolated nanoparticles with pore networks disconnected from the seed crystal. (c) Illustration of a finned zeolite along a cross-sectional (200) plane with fins located on the (020) and (002) facets. The network of interconnected channels is continuous throughout the seed (size β) and fins (size α). Here we depict equal fin spacing (γ).

4.3 Results and Discussion

Using seed-assisted synthesis[15] we prepared a series of finned ferrierite (FER) zeolites. First we synthesized seeds with a relatively uniform size distribution (Figure 4-2a) using a reported protocol with slight modifications[10]. Crystallization of ferrierite resulted in a platelet morphology, which is typical of 2D zeolites, where pores are accessible on low surface area facets (i.e. edges with thickness < 100 nm) and a nonporous basal surface in the [100] plane. The schemes in Figure 1a and 1b highlight porous and nonporous facets as purple and grey shaded regions, respectively. Secondary growth of ferrierite seeds with the careful selection of hydrothermal synthesis conditions (Table S1) resulted in three-dimensional growth of protrusions (referred to as fins) from all surfaces of the platelet. Fins that populate the basal surface (Figure 4-1b) have a pore network that is disconnected from that of the seed, rendering each of these fins an isolated nanoparticle, which differs from zeolites with three-dimensional pores where the channels within fins and seeds are interconnected. The latter is representative of fins populating the edges of ferrierite platelets (Figure 4-1c), which are in crystallographic registry with the seed (*vide infra*), have their 2D network of pores oriented such that they are interconnected with pores in the seed. Herein, we refer to β as the width of seed platelets (*b* or *c* dimension), which is 820 ± 46 nm for seeds prepared in this study. We refer to β as the average size of fins, which are approximately isotropic in shape with a size ranging from 25 to 50 nm. The average spacing between fins, labelled as γ in Figure 4-1c, is 10 – 30 nm.

Parametric analysis of secondary growth conditions revealed that fin size can be tuned by changing synthesis temperature. All syntheses used identical seeds, which are referred to as sample FS. We prepared three finned ferrierite samples of increasing fin size using synthesis temperatures of 120 °C (Figure 4-2b), 130 °C (Figure 4-2c), and 140 °C (Figure 4-2d); these samples are referred to as FSF1, FSF2, and FSF3, respectively. Scanning electron micrographs showed that the lowest temperature for seeded growth results in reduced coverage of fins (Figure 4-2b and 3a) compared to the two samples prepared at higher temperatures where reduced energetic barriers for surface nucleation lead to a higher density of fins.

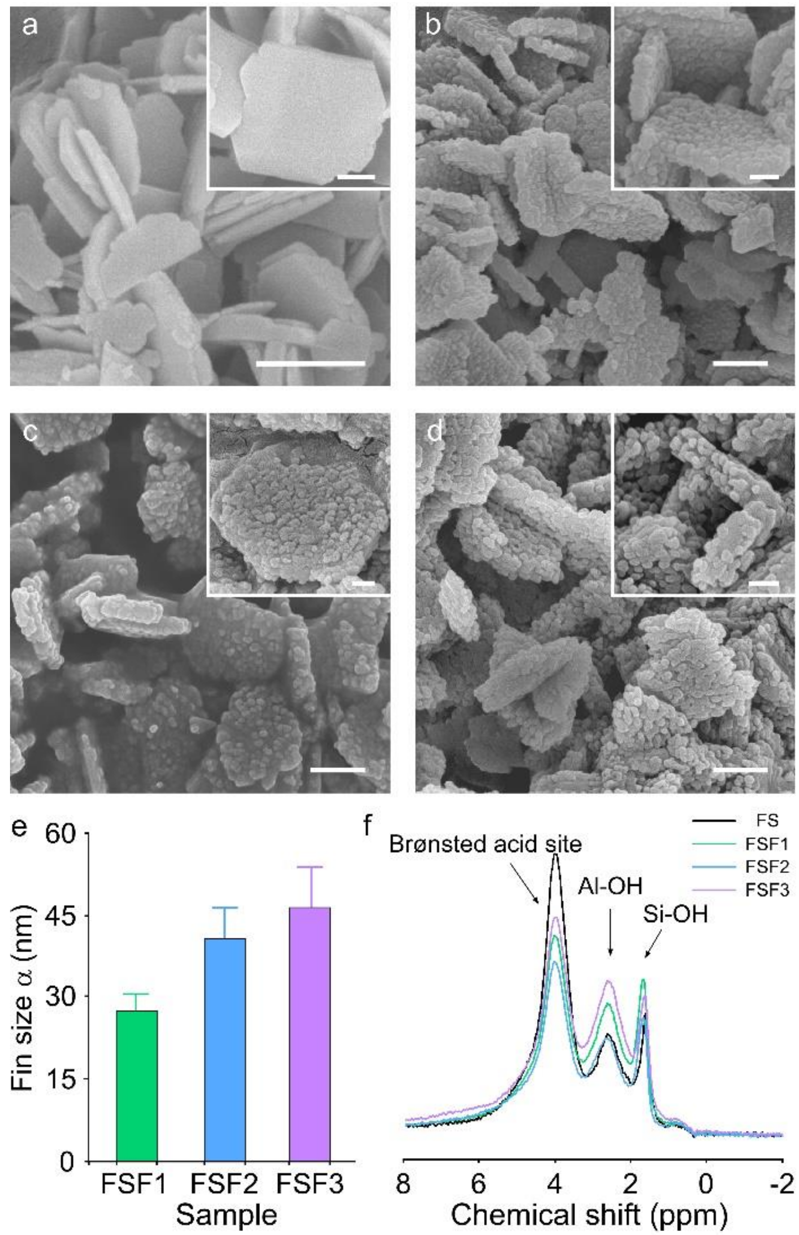

Figure 4-2. Validation of tunable fin size on ferrierite crystals.

(a – d) Scanning electron micrographs of (a) seed and (b – d) finned crystals prepared at three different synthesis temperatures: (b) 120 °C (FSF1), (c) 130 °C (FSF2), and 140 °C (FSF3). Scale bars equal 500 nm. Insets: high magnification images of representative crystals. Scale bars equal 200 nm. (e) Comparison of fin size α for all finned ferrierite samples. Measurements are the average of ca. 30 crystals from a single batch. Error bars equal one standard deviation. (f) Solid state ^{1}H MAS NMR analysis of H-form zeolites prepared for catalyst testing.

Moreover, an increase in temperature resulted in a monotonic increase in α, as shown in Figure 2e. Powder X-ray diffraction (XRD) patterns of all samples (Figure S1) indicated complete crystallinity without evidence of impurities. Textural analysis revealed that both seed (FS) and finned (FSF1, FSF2, and FSF3) samples have similar micropore volume (Table 4-1) with type IV isotherms (Figure S2) confirming the absence of mesopores after secondary growth. The increased size and coverage of fins with increased synthesis temperature resulted in a maximum external surface area corresponding to sample FSF2 (Table 4-1). Elemental analysis indicated that the compositions of both seed and finned samples are nearly identical (Si/Al ratio = 9.2 ± 0.4, Table 4-1). We also checked for potential elemental zoning[16], which is a phenomenon where mesoscopic gradients in Si/Al ratio can lead to either Si- or Al-rich exterior rims of zeolite crystals. Comparison of the bulk composition measured by inductively-coupled plasma optical emission spectrometry (ICP-OES) to that of the surface measured by X-ray photon spectroscopy (XPS) showed only mild Si-zoning for samples FS and FSF1 (Table 4-1), and no appreciable differences for finned samples FSF2 and FSF3.

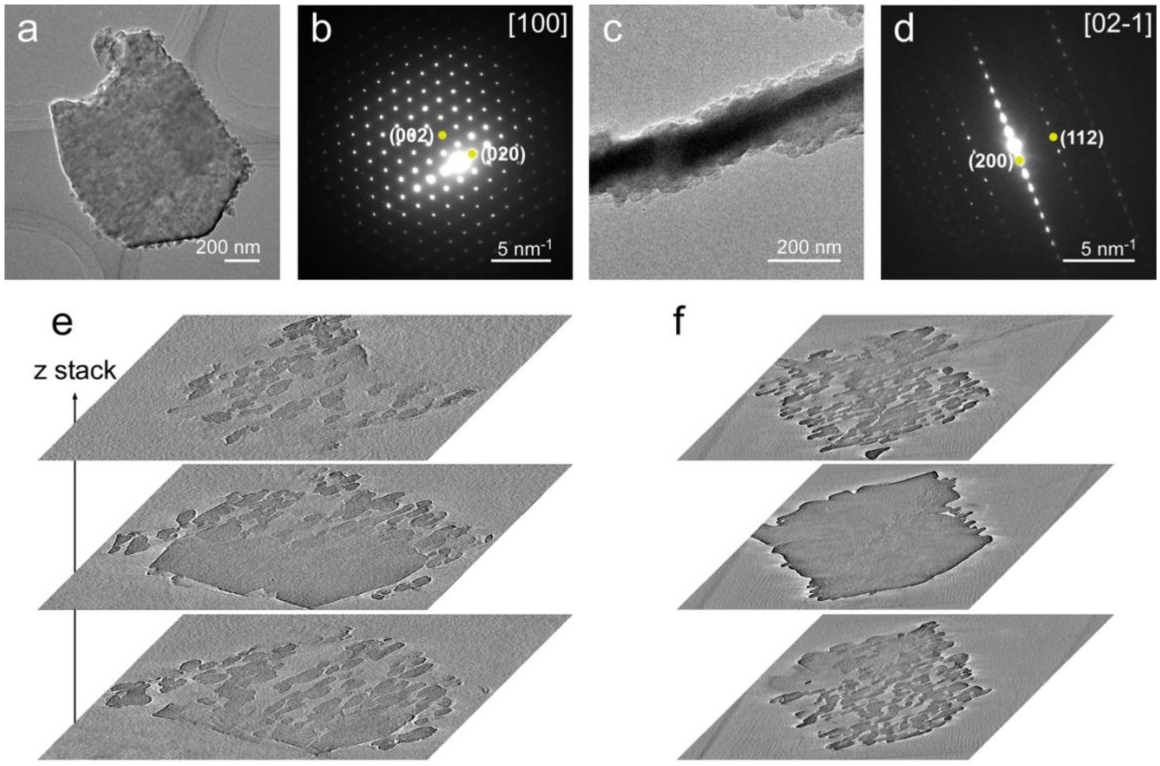

Figure 4-3. Confirmation of finned zeolite 3D morphology and structure.

Transmission electron micrographs of sample FSF1 along directions normal to the (a) basal surface and (c) edge of the platelet. SAED patterns (b and d, respectively) reveal a single crystal, indicating both fins and seed have identical crystallographic orientation. (e and f) TEM tomography images of representative crystals from samples (e) FSF2 and (f) FSF3 showing cross-sectional images along the z direction (see Movies S2 and S3, respectively). Scale bars equal 500 nm unless otherwise denoted.

Transmission electron microscopy (TEM) confirmed the epitaxial growth of fins on seed crystal surfaces. TEM analysis of sample FSF1 captured images of platelets oriented normal to the basal surface (Figure 4-3a) and crystal edge (Figure 4-3c). Both of these facets were laden with fins, confirming secondary growth occurs on all facets of FS seed crystals (Figure S3). Selected area electron diffraction (SAED) of each crystal orientation (Figure 4-3b and d, respectively) confirmed that fins are in crystallographic registry with the underlying seed crystal; thus, the conditions reported in this study lead to epitaxial growth of fins. The systematic absences of the corresponding *hkl* planes expected for a *Immm* space group (Figure S4 and Movie S1) were confirmation of fins having an FER framework[17]. This was also evident in SAED patterns for samples FSF2 (Figure S5) and FSF3 (Figures S6 and S7).

The distribution of fins on external facets was assessed by TEM tomography wherein two-dimensional planes of target crystals were computationally reconstructed along the z direction (z stacks), which is parallel to the (200) crystal plane of the finned samples. Representative z-stack images of sample FSF2 are shown for planes imaged near the bottom, middle, and top of the platelet (Figure 4-3e and Movie S2). Similar tomography tilt series were collected for samples FSF3 (Figure 4-3f and Movie S3) and FSF1 (Movie S4). In all of the finned samples, TEM analysis revealed a relatively uniform coverage of fins on all crystal facets with average sizes that are consistent with those measured by SEM (Figure 4-2e). Moreover, the increased coverage of fins with increasing synthesis temperature was evident in TEM images and reconstructed tomography z stacks.

As proof of concept for upgrading a conventional zeolite with fins, we selected a commercial ferrierite from Zeolyst (CP914C) as a seed and generated a finned analogue using similar secondary growth mixtures at 130 °C. We refer to seed and finned samples as FC and FCF, respectively. The physicochemical properties of these materials (Table 4-1 and Figure S1) were similar to the samples synthesized in house with respect to composition (Si/Al ratio), surface area, and crystallinity. SEM images of the as-received FC sample revealed a heterogeneous size distribution of ferrierite crystals (Figure S8) with β spanning from 400 to 800 nm. Electron microscopy images of finned sample FCF (Figure S8) revealed a fin size (36±12 nm) and coverage similar to sample FSF2. The SAED patterns for FCF (Figure S9) also confirmed its single crystal structure, indicating epitaxial growth of fins on seed surfaces.

Table 4-1. Physicochemical properties of seed and finned H-form ferrierite samples.

Sample [a]	BET S_A (m^2/g) [b]	S_{ext} (m^2/g) [b]	V_{micro} (cm^3/g) [b]	Si/Al (bulk)[c]	Si/Al (surface)[c]	BAS (μmol/g) [d]	EFAl (%)[e]	τ_{fp}, fast time scale peak (min)[f]
FS	354	73	0.11	8.7	11.5	750	9.5	14.0
FSF1	387	106	0.11	9.5	11.8	590	8.5	21.5
FSF2	391	134	0.11	9.4	9.3	510	7.1	17.0
FSF3	389	99	0.12	9.1	9.7	670	12.1	28.0
FC	369	37	0.13	10	10.6	540	6.9	n.a.
FCF	362	41	0.13	10.2	11.0	580	7.8	37.5

[a]FS = synthesized FER sample, FC = commercial FER sample (Zeolyst CP914C); [b]N_2 adsorption/desorption measurements of BET total surface area (S_A), external surface area (S_{ext}), and micropore volume (V_{micro}) after calcination and prior to ion exchange; [c]Elemental analysis of bulk and surface Si/Al measured by ICP-OES and XPS, respectively; [d] BAS = Brønsted acid sites measured by ^1H MAS NMR; [e] EFAl = extra-framework aluminum measured by ^{27}Al MAS NMR; [f] Fast time scale (first peak maximum) from time-resolved titration of Brønsted acid sites by 2,3-dimethylpyridine.

All synthetic and commercial seed and finned ferrierite samples were ion exchanged with NH_4^+ and calcined according to an established protocol[18] to generate H-form catalysts. The acidity and aluminum speciation of the catalysts were characterized by multiple techniques. The quantity of Brønsted acid sites (BAS) could not be determined by a combination of ammonia temperature programmed desorption (NH_3-TPD) and pyridine Fourier transform infrared (FTIR) analyses owing to the inability of bulky pyridine molecules to access acid sites within 8-MR pores[19]. Instead of relying solely on NH_3-TPD, which overestimates the Brønsted acid site concentration, we used an established protocol based on solid state ^1H MAS NMR (Figure 4-2f) where a common external standard (adamantane)[20] was added to more accurately quantify BAS concentration (Tables 1 and S2) using chemical shifts in NMR spectra (ca. 4 ppm) related to framework Al. The percentage of extra-framework Al (EFAl) was obtained by solid-state ^{27}Al MAS NMR (Figure S10), where we observed a relatively narrow range of values spanning 7 to 12% (Table 4-1) with no discernable trends among seed and finned samples. Moreover, the general trend in BAS concentration is difficult to ascertain given that all in-house finned samples (FSF1, FSF2, and FSF3) have notably smaller values compared to the parent seed (FS), whereas the finned commercial sample (FCF) has a slightly higher BAS concentration compared to its parent seed (FC). These differences can be attributed to variations in non-framework or distorted framework Al sites. To account for the subtle differences in acidity we report the turnover number (TON), which accounts for the BAS concentration of each catalyst (see Appendix for details).

For catalytic testing we selected the 1-butene isomerization reaction to assess the effects of fins. The desired product from this isomerization reaction is isobutene (Figure 4-4a) with a variety of undesirable side products that include propene and pentene, among others. Catalyst testing was performed at sub-complete conversion of 1-butene (initial conversion of ca. 60%) in a fixed bed reactor at 400 °C using a weight-hourly space velocity of 12 h^{-1}. The TON was evaluated from the conversion versus time on stream curve of each catalyst (Figure S11) within a fixed range of 45 to 55% conversion. The parent seed FS had a TON of 5600 (Figure 4-4b) while the three finned samples (FSF1, FSF2, and FSF3) exhibited nearly two-fold increases in turnover number (spanning 9600 to 11500). The most effective catalyst was FSF2, which had the lowest BAS concentration among finned samples but also had the highest external surface area and lowest percentage of EFAl (Table 4-1). The presence of EFAl species can have a deleterious effect on catalyst performance[21], whereas the external surface area can enhance molecule entry and exit from zeolite pores, thereby reducing the rate of catalyst deactivation by coking. This indicates that the synthesis temperature during secondary growth of fins is critical for catalyst preparation, with the intermediate temperature of 130 °C used to prepare FSF2 being the most optimal condition.

In literature it has been proposed that 1-butene isomerization involves three possible mechanisms: monomolecular, bimolecular, and pseudo-monomolecular[22]. It has been hypothesized that catalyst deactivation is attributed to the pseudo-monomolecular mechanism[22]. We observed that seed and finned catalysts all have similar initial conversion at fixed space velocity (Figure S10), despite differences in BAS concentration ranging from 510 to 750 µmol/g; however, there were clear differences in catalyst deactivation wherein a temporal decrease in conversion (Figure S10) resulted in nearly linear rates of deactivation with finned catalysts coking less rapidly than the parent seed (i.e. deactivation rates of 0.5 and 1.5 h^{-1}, respectively). The ability of fins to improve catalyst lifetime is consistent with trends observed in the methanol-to-hydrocarbon reaction for ZSM-5 (MFI) and ZSM-11 (MEL) catalysts[18], where we have shown that fins reduce the internal diffusion path length and increase the rate of molecule sorption into pores. These collective effects reduce mass transport limitations in finned catalysts with a concomitant reduction in the rate of external coke accumulation.

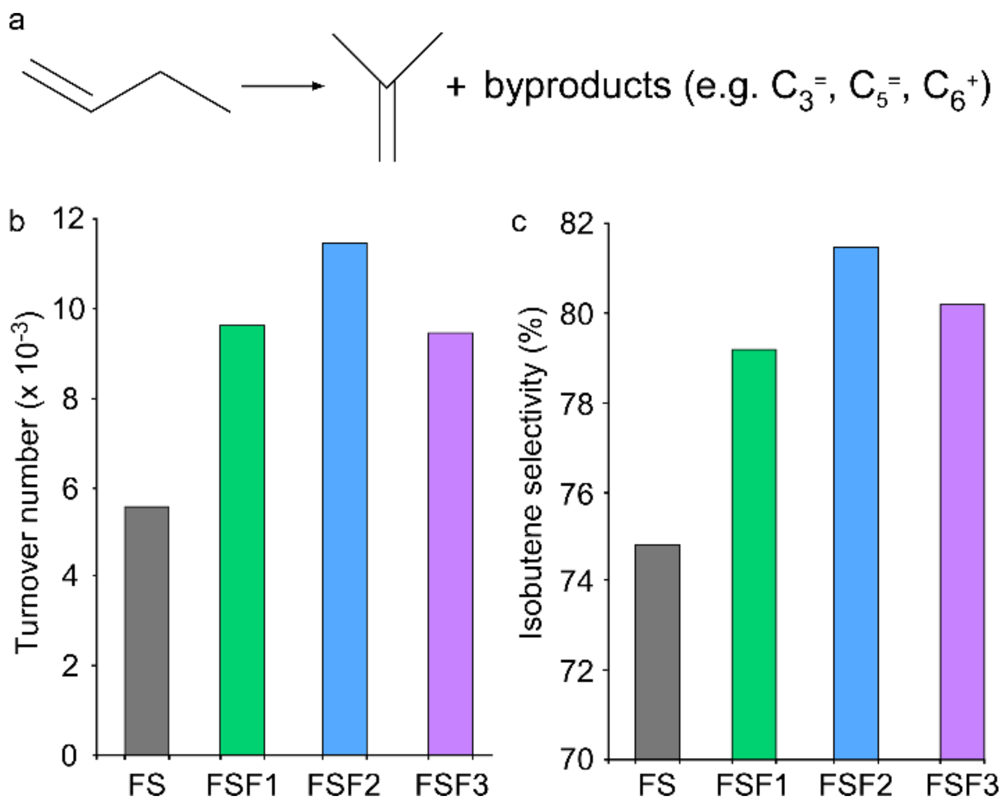

Figure 4-4. Performance of finned zeolite catalysts.

(a) Reaction of 1-butene to isobutene and byproducts (propene, pentene, etc.). (b) Comparison of turnover number (units of mol_C/mol_{H^+}) for the seed (FS, grey) and finned (FSF1, FSF2, and FSF3) catalysts in the isomerization reaction at subcomplete conversion of 1-butene (≤ 60%). Reactions were performed at 400 °C with WHSV = 12 h^{-1} (evaluated between 45 – 55% conversion, Figure S10). (c) Corresponding isobutene selectivity for each catalyst (evaluated at a 1-butene conversion of 50%). The complete distribution of product selectivity is provided in Figure S12.

We also observed that finned ferrierite zeolites increase isobutene selectivity from 75% for FS to 81% for FSF2 (Figure 4-4c). This is qualitatively consistent with previous studies showing that decreased size of ferrierite catalysts results in improved selectivity[10]. While it has been reported that the bimolecular mechanism is unselective for isobutene[22], the exact reason for increased selectivity in finned and nano-sized ferrierite zeolites is unresolved. We posit that one contributing factor may be the reduced probability of secondary reactions (e.g. cracking or polymerization) as a result of the shortened diffusion path length in finned regions of the catalyst.

Here we report the relative performance of commercial seed (FC) and finned (FCF) catalysts (Figure 4-5a) as the change in conversion with time on stream. The latter was converted to cumulative turnovers as a more direct way of comparing catalyst deactivation. Interestingly, we observed a nearly four-fold decrease in the deactivation rate of the finned commercial sample (0.3 h^{-1}) relative to its parent seed (1.4 h^{-1}). Comparison of TON (Figure 5b) revealed a three-fold increase for the finned sample (FCF) relative to its seed (FC). In addition, there was a more pronounced impact of fins on isobutene selectivity (Figure 5c) where the differences between FC and FCF increased with time on stream (i.e. with decreasing 1-butene conversion). Notably, isobutene selectivity increased from 67% (FC) to 81% (FCF) at sub-complete (50%) conversion.

To characterize the diffusion properties of finned ferrierite, titration experiments were conducted using time-resolved FTIR spectroscopy to quantify the disappearance of Brønsted acid sites (3605 cm^{-1}) and the concomitant uptake of amines (1555 cm^{-1}). Our previous study showed that 2,4,6-trimethylpyridine slowly accessed the internal pores and titrated BAS of three-dimensional zeolites with 10-MR pores (e.g. MFI) due to steric hindrance from methyl groups[53]. As mentioned, FER is a 2D zeolite comprised of two disparate pores (8-MR and 10-MR). For this study, we used the titrant 2,3-dimethylpyridine (DMPyr), an organic base with smaller kinetic diameter, as the probe molecule due to the slightly smaller 10-MR pore aperture in FER relative to MFI. The use of DMPyr as the probe molecule slowed its diffusion in FER 10-MR channels, thus allowing for time-resolved comparison of the titration of acid sites within the fins and bulk catalyst. However, DMPyr is prohibitively large to access 8-MR channels, and titration of all BAS by DMPyr only occurs via diffusion along the 10-MR channels and adsorption at the intersection of the smaller 8-MR channels.

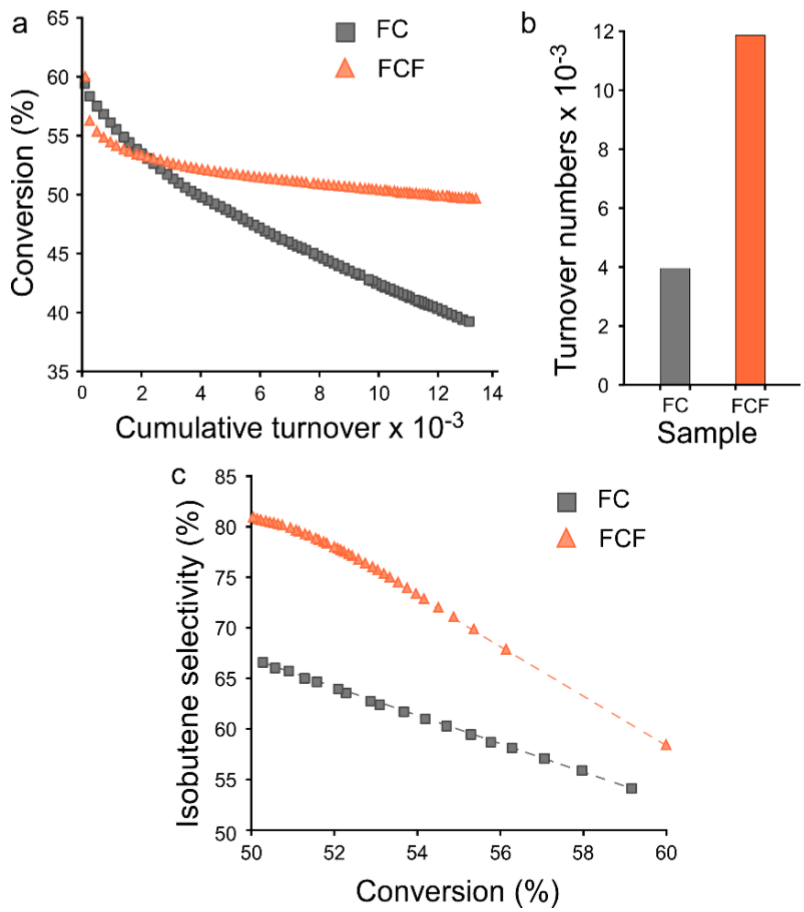

Figure 4-5. Proof of concept of catalyst optimization with fins using commercial ferrierite.

(a) Sub-complete conversion of 1-butene as a function of cumulative turnovers for commercial ferrierite FC (Zeolyst CP914C) and its finned analogue (FCF). Reactions were performed at 400 °C with WHSV = 12 h^{-1}. (b) Comparison of turnover numbers (mol_C/mol_{H^+}) for seed (FC, grey) and finned (FCF, orange) catalysts evaluated at 45 – 55% conversion. (c) Isobutene selectivity as a function of 1-butene conversion.

The adsorption kinetics of DMPyr on BAS of all ferrierite catalysts were assessed via FTIR peak area at 1555 cm^{-1} over 4,000 minutes (Figure 4-6a, S13, S16a, and S17a). As the DMPyr-H^+ peak area increases with time, BAS in the catalyst were fully titrated. To precisely determine the changing rates of amine uptake, the derivative of BAS titration over time was plotted for both seed and finned ferrierite samples (Figure 4-6b, S12, S13b, S14b, and S15).

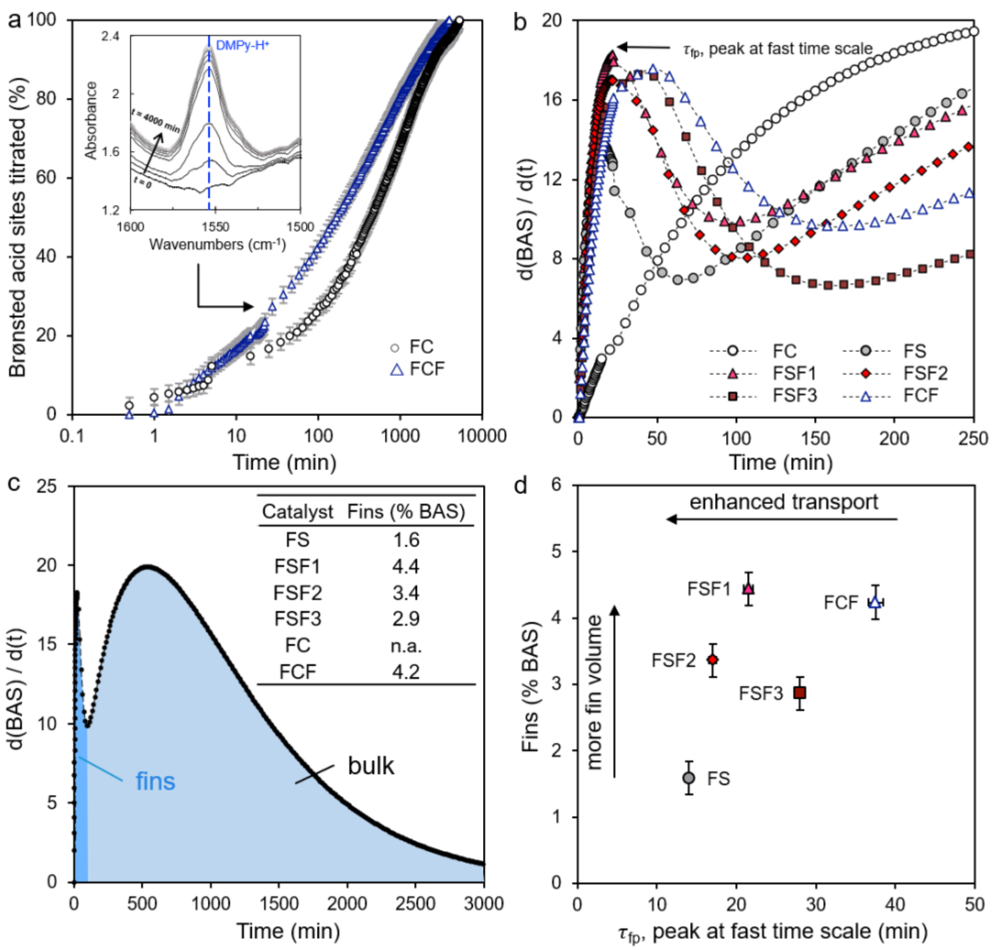

Figure 4-6. Time resolved Brønsted acid sites (BAS) titrated.

(a) Titration of BAS by 2,3-dimethylpyridine in commercial and finned FER (FC, FCF) over time. Inset: Spectra of 2,3-dimethylpyridine titration of Brønsted acid sites (1555 cm^{-1}; DMPy-H^+) of finned FCF as measured over 4000 minutes via Fourier-transformed infrared spectroscopy (FTIR). (b) Derivative of BAS titration for all catalysts. The area under the peaks represents the cumulative amount of BAS titrated at different time points, with the first peak's maxima indicated by τ_{fp}, or peak at fast time-scale. (c) Derivative of BAS titration by 2,3-dimethylpyridine in FSF1 over time. The area under the peaks represents the cumulative amount of BAS titrated at different time points, with the first peak attributed to BAS in the fins of the catalyst, and the second peak attributed to BAS in the bulk catalyst. Inset: Percentage of BAS titrated in fins over the bulk. (d) Percentage of fins BAS plotted as function of peak at fast time-scale, τ_{fp}. FSF1 and FSF2 have higher percentage of fin BAS and lower τ_{fp}, indicating enhanced transport of 2,3-dimethylpyridine (see Fig. S18). Error bars were computed from the sampling of three separate runs of different samples from the same synthesis batch.

The area under the derivative peaks in portion of BAS that can be accessed more quickly than bulk acid sites. This may explain why FS outperforms FC as a catalyst. The initial fast BAS titration was attributed to the BAS in fins and external surface areas of the catalyst, while slower uptake was attributed to the BAS within the bulk catalyst (Figure 4-6c). The percentage of BAS in fins is plotted as a function of τ_{fp} for all catalysts (Figure 4-6d). Finned ferrierite materials, specifically FSF1 and FSF2, had higher percentages of BAS in fins and relatively lower τ_{fp} compared to seed and commercial ferrierite (FS, FC, and FCF). Collectively, these results indicate that enhanced catalyst performance can be attributed to both the improved mass transport properties and higher BAS volume in the fins. Figure 6c represents the cumulative amount of BAS titrated at different times, with the first peak's maximum indicated by τ_{fp} (Table 4-1), also referred to as the "peak at fast time-scale" (Figure S14). We observed that commercial ferrierite (FC) does not exhibit this initial peak τ_{fp} associated with fins, while the catalysts synthesized in-house (FS, FSF1, FSF2, FSF3, and FCF) all had τ_{fp}, indicating the presence of a significant portion of BAS that can be accessed more quickly than bulk acid sites. This may explain why FS outperforms FC as a catalyst. Indeed, the presence of rough features (i.e. small fin-like protrusions) on the surfaces of FS seeds, which are undetected by electron microscopy, are seemingly evident in titration experiments. This is also consistent with FS having a nearly two-fold higher external surface area than FC, despite both samples having (on average) similar crystal size. It is also possible that the commercial sample contains defects that are removed during secondary growth of fins, which contributes to the net improvement in catalyst lifetime and selectivity.

4.4 Conclusion

We have developed a facile and highly versatile method for improving mass transport properties of zeolites with 2D pore networks. Most zeolites with 2D pores crystallize as platelets where internal diffusion is markedly more restricted than 3D counterparts. This places greater emphasis on the ability to synthesize nanosized zeolites and/or control anisotropic crystal growth to achieve morphologies that increase access to pore openings and reduce the internal diffusion pathlength. These outcomes are difficult to achieve by the manipulation of common synthesis parameters. The few cases where nanosized ferrierite crystals are reported in literature rely on the use of unconventional organic structure-directing agents. Here, we demonstrate that secondary growth using traditional synthesis conditions can produce fins of tunable size, thereby endowing conventional ferrierite materials with enhanced properties that align with those of much smaller crystal size. This was confirmed by time-resolved titrations showing an initial uptake of the titrant is more rapid in fins; therefore, the introduction of fins transforms seeds into pseudo nanocrystals with enhanced mass transport and improved catalytic performance.

In this study, we selected 1-butene isomerization to assess the impact of fins on both catalyst lifetime and selectivity. This study was performed using a zeolite with two-dimensional pores to assess the degree to which fins can improve catalyst performance in materials that exhibit more severe mass transport limitations in comparison to three-dimensional zeolites originally used to validate finned synthesis. Our findings revealed that fins dramatically extend the lifetime of ferrierite catalysts and also improve their efficiency (i.e. increase total turnovers) relative to conventional counterparts. This is most evident for commercial ferrierite where finned analogues exhibit a four-fold decrease in the deactivation rate and a three-fold increase in TON. Moreover, finned commercial ferrierite has much higher isobutene selectivity, thus illustrating a key advantage of this approach: the ability to take a zeolite off the shelf and perform a facile post-synthesis modification to improve its properties. While this study focuses on a single reaction, we envision that finned zeolites can be used more generally to improve zeolite performance for a range of commercially-relevant reactions where mass transport limitations impose restrictions on current catalysts.

Chapter 5 – Core-shell and Egg-shell Zeolite Catalysts for Enhanced Hydrocarbon Processing

*Reproduced with permission from T. T. Le, K. Shilpa, C. Lee, S. Han, C. Weiland, S. R. Bare, P. J. Dauenhauer, J. D. Rimer. Core-shell and Egg-shell Zeolite Catalysts for Enhanced Hydrocarbon Processing. *Journal of Catalysis* **405** (2022) 664-675.

5.1 Conspectus

Developing structure-performance relationships with the underlying goal of optimizing known zeolite catalysts involves the manipulation of their physicochemical properties. Here, we systematically assessed the impact of mesoscopic gradients in acid site concentration, which has received little attention in the design of zeolite catalysts for hydrocarbon upgrading. A series of core-shell MEL-type zeolites were synthesized with catalytically active ZSM-11 cores and passivated silicalite-2 shells of varying thickness. Our findings revealed that ZSM-11@silicalite-2 particles with ultrathin shells (< 10 nm) have enhanced mass transport, characteristic of relatively smaller particles, compared to the corresponding ZSM-11 core. Catalytic testing using the methanol-to-hydrocarbon (MTH) reaction showed that core-shell zeolites exhibit longer lifetimes, higher total turnovers, and an unexpected promotion of the aromatic cycle in the hydrocarbon pool mechanism. Time-resolved acid titration of core and core-shell catalysts confirmed that the siliceous shell introduces a hydrophobic exterior that impacts molecular diffusion. In comparison, prepared MFI core-shells (ZSM-5@silicalite-1) showed similar enhancement in catalyst performance. Moreover, we prepared egg-shell configurations of each zeolite, silicalite-2@ZSM-11 and silicalite-1@ZSM-5, comprised of an inert core and catalytically active shell. This inverse design of the egg-shell created pseudo nanosheets with total turnovers that were markedly higher than their homogeneous counterparts. Collectively, this study demonstrated that mesoscopic gradients in acid concentration via the design of core-shell and egg-shell zeolites markedly improve catalyst performance over conventional analogues for hydrocarbon upgrading.

5.2 Introduction

Many synthetic approaches to optimize the physicochemical properties of zeolite catalysts focus on the design of hierarchical materials with nano-sized microporous domains that reduce diffusion limitations, thereby enhancing overall catalytic performance [1, 2]. There has also been growing interest in the development of methods to control aluminum distribution in zeolite frameworks on both a microscopic and mesoscopic level [3-5]. In this manuscript, we combine these approaches in catalyst design by focusing on the preparation of zeolites with tailored mesoscopic gradients in aluminum composition (i.e. Si/Al ratio) and assessing their effects on catalyst performance using the methanol-to-hydrocarbons (MTH) reaction. Prior studies have reported the synthesis of naturally *zoned* zeolites where the exterior rim is enriched in either aluminum or silicon [6, 7]. Among reported cases of zoning, the majority involve Al-zoned MFI-type zeolites; Weckhuysen and coworkers [6] reported the direct synthesis of Si-zoned MFI zeolite and demonstrated by operando MTH testing of single crystals that the siliceous exterior suppresses the formation of external coke (i.e. development of bulky aromatics and graphitic hydrocarbons) owing to the passivation of external acid sites.

An analogous approach to passivate the external surfaces of zeolite catalysts involves post-synthesis processes wherein a silicon-rich layer of either amorphous silicate or siliceous zeolite is grown on the surface of a parent zeolite crystal. Early methods of surface passivation commercialized by DuPont [8] and Mobil [9] used chemical vapor or liquid deposition of silanes. Other similar approaches have been adopted [10, 11] with the objective of eliminating surface reactions to enforce shape selectivity within micropores. One of the challenges associated with surface passivation is the potential for narrowing or blockage of pore mouths, which can lead to improved product selectivity often at the expense of reduced catalyst activity. An alternative technique that is more broadly applied in heterogeneous catalysis [3] involves secondary growth of seed crystals to generate a core-shell structure wherein the core and shell are of distinct compositions or crystal structures. One example of core-shell zeolites is ZSM-5@silicalite-1, where both core and shell have the same MFI framework structure [12]. Prior studies of core-shell zeolites have been limited to around five different frameworks [13-16]. In most cases, the shells are polycrystalline and/or non-contiguous with thicknesses in the hundred nanometers to micrometers range, which can negate the benefit of surface passivation by exacerbating mass transport limitations and/or leaving segments of the core without coverage of a shell.

Mass transport limitations in zeolite pores can be mitigated by tailoring crystal size and pore heterogeneity, either through the synthesis of nano-sized crystals or materials with intraparticle meso/macroporosity. Examples include two-dimensional nanosheets [1], self-pillared pentasils with dimensions spanning from 2 to 30 nm [17-19], hierarchical (or mesoporous) zeolites [20], finned zeolites [21], and nanoparticles with sizes less than 100 nm [22]. Studies have demonstrated that enhanced diffusion in these materials coupled with increased external acidity (i.e., increased surface area) generally improves catalytic stability compared to conventional zeolites. One design concept that transcends multiple classes of heterogeneous catalysts is supported metal/oxide catalysts [23, 24]; and an analogous design is that of an egg-shell structure (opposite that of a core-shell) where the active catalyst is an ultrathin shell that is a pseudo-nanosheet. One feature of the egg-shell architecture is the same crystal structure of both the inert core and the catalytically-active shell. It is common in literature to find the term ‘egg-shell’ used in different connotations. For example, Mintova and coworkers [25] used this term to describe heterogeneity within zeolites in reference to defect-zoned shell layers obtained via post-treatment fluoride etching (a material that is structurally distinct from the egg-shell zeolites described herein). Alternative terminology includes *yolk-type* catalysts, which are comprised of a core with a crystal structure that is different than the shell. Examples of yolk-type catalysts include metal oxides encapsulated by a hollow zeolite [26], or zeolite-zeolite composites such as SAPO-5@ZSM-5 [27] or zeolite Y@beta [28]. A common attribute of zeolite yolk-type catalysts is a non-contiguous shell comprised of zeolite particles either grown or adhered to the core.

It has been reported that there are positive effects of surface passivation and core-shell configurations on catalyst performance, such as improved product selectivity [10, 29-31] and conversion capacity [32]; however, the difficulty of synthesizing well-defined zeolitic materials with uniform shells and controlled shell thickness has obfuscated the precise effects of surface passivation on catalyst performance. In this respect, methanol to hydrocarbons (MTH) is an appropriate probe reaction for these type of studies. MTH is highly relevant to the energy industry as a key step to gasoline-rich and olefin-rich products from alternative carbon sources [33]. A recent scientific review of MTH revealed several zeolites as effective catalysts for upgrading methanol to gasoline derivatives [34]. To this end, major research initiatives in both industry and academia have been focused on improving the efficiency of MTH processes, with one critical optimization parameter being catalyst design. Although extensively researched, the MTH mechanism is still not fully understood – notably the less discussed process, known as the direct mechanism, responsible for the formation of the first C-C bond during the induction period, which feeds into the well-known autocatalytic dual cycle mechanism [35]. Advancements in computational and experimental techniques have spurred research efforts to identify and validate specific pathways and species associating with the direct-coupling mechanism and linking it to the hydrocarbon pool mechanism [36-38]. It is postulated that key C_2-C_4 olefins species [34] undergo further oligomerization and aromatization to form larger olefins and aromatic species, which become part of the hydrocarbon pool and concomitantly transform into alkanes via hydrogen transfer reactions. The direct mechanism is a subject of on-going study with relatively few established structure-mechanism relationships. Several studies [35] have demonstrated the influence of extra-framework aluminum species in facilitating the formation of key products in the direct mechanism. On the contrary, the autocatalytic cycles, also known as the dual cycle mechanism, is relatively more established. The dual cycle mechanism involves an aromatic (arene) cycle and an olefins (alkene) cycle [39] which are connected via hydrogen transfer reactions. The relative propagation of the two cycles can be described with a selectivity ratio of ethene, the primary product of aromatic cycle, and the sum of 2-methylbutane and 2-methyl-2butene (2MBu), the primary products of the olefin cycle [40]. More recently, various studies have revealed the importance of formaldehyde in the dual cycle mechanism, which can accelerate the formation of bulky aromatic species (i.e. coke) [41-43] Therefore, the ability to reduce coke, which can obstruct pores and access to catalytically-active sites [44], is critical to enhancing catalyst performance.

In this study, we synthesized a series of MEL and MFI zeolites with core-shell and egg-shell configurations and assessed their performance in the MTH reaction relative to catalysts with homogeneous distributions of acid sites. These core-shell zeolites contain regions of composition that range from purely-siliceous (silicalite-2 and silicalite-1 for MEL and MFI, respectively) to aluminosilicate (ZSM-11 and ZSM-5 for MEL and MFI, respectively). Based on our previous study of ZSM-5@silicalite-1 core-shell synthesis [45], we used a similar strategy to prepare ZSM-11@silicalite-2 catalysts with varying shell thickness. We also report the synthesis of egg-shell catalysts for both zeolite frameworks. The MEL-type zeolite was selected for systematic analysis owing to its more simplified network of channels relative to MFI, and based on previous catalytic testing showing superior performance of MEL zeolites in the MTH reaction [46-48]. Collectively, our findings indicate that both core-shell and egg-shell zeolite@zeolite configurations markedly improve catalyst lifetime and activity relative to their homogeneous counterparts.

5.3 Experimental Methods

The following reagents were purchased from Sigma-Aldrich: tetraethyl orthosilicate (TEOS, 98%), tetrabutylammonium hydroxide (TBAOH, 40%), 1,8-diaminooctane (DAO, 99%), aluminum sulfate ($Al_2(SO_4)_3$), silica gel (Davisol Grade 636, 35-60 mesh size), and pyridine (99.8%, anhydrous). The following reagents were purchased from Alfa Aesar: sodium aluminate ($NaAlO_2$, technical grade) and tetrapropylammonium hydroxide (TPAOH, 40%). Deionized (DI) water was produced with an Aqua Solutions RODI-C-12A purification system (18.2 MΩ). All reagents were used as received without further purification. For reaction testing, methanol was purchased from Sigma Aldrich (ChromaSolv, 99.9%), and argon, oxygen, and nitrogen gases were purchased from Matheson (UHP grade, 99.999%).

The synthesis of core ZSM-11 samples followed a previously published protocol for synthesis of MEL with 1,8–diaminooctane [46] Note that all zeolite crystal structures are referred to by their three letter framework codes (MEL or MFI) assigned by the International Zeolite Association [49]. The molar composition of the synthesis solution for MEL zeolite was 30 DAO: 10 K_2O: 100 SiO_2: 1 $Al_2(SO_4)_3$: 4000 H_2O. The solution was aged under stirring for 24 h before hydrothermal synthesis at 160°C for 3 d. The synthesized core was washed three times with centrifugation and stored in DI H_2O before shell growth. Core-shell ZSM-11 was synthesized using a modification of a previously published protocol [45]. The shell growth solution was 14 TBAOH: x SiO_2: 9500 H_2O with x varied in the range of 17-30 to control shell thickness. The synthesis was performed at 100°C for 1 d, followed by an annealing process with 14 TBAOH: 10 SiO_2: 9500 H_2O. The growth solution was aged for 24 h before silicalite-2 core was added to get a 1 wt% suspension. The synthesis of core-shell ZSM-5 followed a reported protocol [45] similar to steps outlined above. A secondary growth solution with molar composition 14 TPAOH: 17 SiO_2: 9500 H_2O was chosen to generate a thin shell.

Synthesis of the silicalite-1@ZSM-5 egg-shell zeolite involved the use of a silicalite-1 core, which was generated using a growth solution of molar composition 0.3 TPAOH: 1.0 TEOS: 35 H_2O based on a published protocol [50]. The synthesis was performed at 170°C for 3 d. The aluminum containing shell was grown using a molar composition of 20 TPAOH: 4 Na_2O: 100 SiO_2: 2.5 Al_2O_3: 4000 H_2O. The mixture was aged for 2 h before silicalite-1 seed was added to obtain a 10 wt% suspension. The synthesis was performed under rotation at 120°C for 2 d, following by a hydrothermal annealing process described in the cited procedure. Synthesis of the silicalite-2@ZSM-11 egg-shell zeolite involved the use of a silicate-2 crystal seed (core) prepared from a growth mixture with molar composition 20 TBAOH: 4 Na_2O: 100 SiO_2: 4000 H_2O. The synthesis was conducted at 150°C for 1 d. The aluminosilicate ZSM-11 shell was grown in a secondary growth mixture using a molar composition of 20 TBAOH: 4 Na_2O: 100 SiO_2: 2.5 Al_2O_3: 6000 H_2O. The synthesis mixture was initially aged for 2 h at room temperature prior to the addition of silicalite-2 seed to obtain a 10 wt% suspension. The synthesis was performed at 130°C for 2 d under rotation.

For both egg-shell syntheses, crystals were isolated from the supernatant by three cycles of centrifugation and washing with DI H_2O, dried at room temperature in air, and then calcined in a muffle furnace at 550°C using heating and cooling rates of 1 °C min^{-1} for 5 h. Ion exchange was performed three times using a 1 M NH_4NO_3 solution (2 wt% of calcined samples in solutions), which was heated at 80°C under continuous stirring for 2 h. The exchanged samples were dried and calcined by the same procedure described above to obtain H-form zeolites.

Powder X-ray diffraction (XRD) patterns were collected on a Rigaku diffractometer using Cu Kα radiation (40 kV, 40 mA) to verify the crystallinity and topology of the catalysts. Nitrogen physisorption experiments were performed on a Micromeritics ASAP 2020 instrument at 77 K to calculate micropore volumes (t-plot method) and BET surface area. Transient sorption experiments with 2,3-dimethylbutane were performed, and collected data was fitted following a previously reported procedure [47, 51] to obtain the characteristic diffusion timescale R^2/D. Scanning electron microscopy (SEM) was done on a GEMINI FE-SEM system. The overall Si/Al ratio was determined by inductively coupled plasma optical emission spectrometry (ICP-OES) analysis at Galbraith Laboratories (Knoxville, TN). Energy dispersive X-ray spectroscopy (EDX) was performed using a JEOL SM-31010/METEK EDAX system at 15 kV and 15 mm working distance. X-ray photoelectron spectroscopy (XPS) analysis of samples was performed using a PHI 5800 ESCA (Physical Electronics) multitechnique system equipped with a standard an achromatic Al Kα X-ray source (1486.6 eV) operating at 300 W (15 kV and 20 mA) and a concentric hemispherical analyzer. The equipment neutralizer component was utilized to reduce charging effects. All data were collected at a 45° takeoff angle.

We used a combination of two elemental analysis techniques, EDX and XPS, to characterize the distribution of elements in ZSM-5 zeolites. The average bulk chemical composition of ZSM-5 crystals was estimated by EDX, which has a sampling depth around two micrometers. The chemical composition of the outer rim of zeolite crystals was evaluated by XPS, which is a surface-sensitive technique with a sampling depth of only a few nanometers [52]. To approximate shell thickness of the core-shell and egg-shell ZSM-5 samples, we used dynamic light scattering (DLS) to obtain the average hydrodynamic diameter. Initially, a small amount of sample was dispersed into DI water and sonicated at 8W for 5 – 10 min. The solution was then filtered through a 250 µm membrane, further diluted with DI water, and placed in a clean glass vial. The level of dilution was adjusted to ensure a scattering count rate within 100 to 400 kcps. The glass vial was placed in a filtered decalin bath sample holder housed within a Brookhaven Instruments BI-200SM DLS equipped with a HeNe laser (637nm) and TurboCorr Digital Correlator. A total of eight measurements (2 min each) was taken for each sample at 25°C. The autocorrelation functions collected were analyzed using the method of cumulants in the Brookhaven Instruments Corporation DLS software. The shell thickness of the core-shell sample ZSM-5@silicalite-1 was estimated from differences in the hydrodynamic diameters of core and core-shell. The shell thickness of the egg-shell sample, silicalite-1@ZSM-5, was calculated similarly.

We used variable kinetic energy X-ray photoelectron spectroscopy (VKE-XPS) to probe the change in Si and Al contents as a function of depth into the crystals. VKE-XPS was performed at NSLS-II (Brookhaven National Laboratory, Upton, NY) at the HAXPES endstation at beamline 7-ID-2. The powder form of samples was deposited onto carbon tape followed by the deposition of a thin layer of carbon coating (ca. 10 nm) to reduce charging effects. Samples were attached to the sample holder rod and installed in the vacuum chamber and allowed to pump overnight. A neutralizer was also used to further minimize charging. A plane mirror was used for large (mm scale) spot size for spectra collection, with pass energy of 500 eV and a take-off angle of 80°. An Ag 3d spectrum was collected after every photon energy change to calculate actual ionization energy. Each sample sweep was for 0.5 to 1 h with a time ratio of 1:30 of Si 1s to Al 1s. The collected spectra were integrated using the Scienta program (IgorPro), and the peak areas were subsequently corrected with Scofield cross-section (NIST XCOM database) for Si/Al calculation. Inelastic mean free path (IMFP, λ) was calculated from corresponding Si 1s and Al 1s kinetic energy at each photon energy (eV) using relativistic equation TPP2M formula in the QUASES program) for SiO_2 and Al_2O_3. The information depth was then calculated from IMFP using the following equation:

$$\text{Information depth} = 3\lambda\cos(\theta_{photoemission}) \tag{5-1}$$

Aluminum speciation was determined from ^{27}Al MAS NMR spectra collected at a spinning frequency of 12.5 kHz, pulse of π/12, relaxation delay of 0.8s, and 4K scans at 11.7T on a JEOL ECA-500 spectrometer [53]. We quantified the total number of acid sites with temperature-programmed desorption of ammonia (NH_3-TPD) on a Micromeritics Autochem II 2920 equipped with a TCD detector. Approximately 100 mg of catalyst sample was degassed for 1 h at 600°C before being cooled down to 100°C for ammonia adsorption. At saturation, the sample was flushed with He for 120 min before we ramped up the temperature to 600°C at a rate of 10 °C min^{-1} while concurrently monitoring the desorbed ammonia with the TCD detector. To identify the types of acid sites (i.e., Lewis and Brønsted), we conducted pyridine-adsorbed Fourier-transform infrared spectroscopy (pyr. FTIR). We first collected background spectrum at room temperature for a high temperature cell equipped with KBr windows using a Nicolet 6700 FTIR spectrometer. Subsequently, approximately 20 mg of sample was pelletized and placed in the cell. The configuration was installed in the spectrometer and connected to heated N_2 gas lines (150°C). The cell was heated to 550°C for 2 h to eliminate adsorbed moisture in the sample before being cooled down to 200°C for the adsorption experiment. Parent spectrum is collected before increment of 1 □l anhydrous pyridine (Sigma Aldrich) was injected into the heated N_2 stream (Matheson, 50 cm^3 min^{-1}). Spectra were collected 5 min after each injection until saturation, and the final spectrum was collected after purging for 2 h with N_2. The subtracted results from the final and parent spectra were analyzed using OMNIC software with peaks assigned to Brønsted and Lewis acid sites at 1545 and 1450 cm^{-1}, respectively [54]. The corrected peak area was used to obtain the percentages of Brønsted and Lewis acid sites.

Time-resolved amine uptake spectra were measured using FTIR with a HeNe laser and RT-DLaTGS detector (Bruker Vertex 70, 20 kHz scanner velocity, 6 mm aperture, KBr beam splitter). For sample preparation, ca. 15 mg of powder catalyst sample was homogenized using an agate mortar and pestle, pressed (Pike Technologies, CrushIR Digital Hydraulic Press) at ~3 ton for 5 min into 13 mm-diameter pellets (International Crystal Laboratories, KBR Die, CAS#7758-02-3) and inserted into the cell body (Harrick Scientific, High Temperature Cell, Part No. HTC-M-05, CaF_2 windows). Before inserting each sample pellet, a background spectrum was collected (64 scans, 4 cm^{-1} resolution) with the empty cell. A K-type thermocouple (Harrick Scientific, Part No. 008-144) was in constant intimate contact with the sample pellet holder to measure the temperature. The manufacturer-provided cartridge heater (100W, 24V) was controlled via a temperature controller in cascade mode (Omega CN7800). To ensure that the CaF_2 windows of the sample cell does not overheat, cooling water was continuously pumped (Control Company, Variable Flow Chemical Pump) and flowed through water cooling ports connected to the cell body. The sample was calcined at 500°C for 4 h in air (Linde, Air Ultra Zero) at a ramp rate of 1 °C min^{-1}. After calcination, the sample was cooled down and remained at 240°C for the duration of the experiment to ensure the absence of water. Cold 2,4,6-trimethylpyridine (Sigma-Aldrich) was used for dosing in FTIR. For the amine dosing process, He gas (Minneapolis Oxygen Company, Grade 5.0 He, UN1046) was flowed over the sample pellet to purge any remaining air. To ensure that the He is moisture-free, He gas was flowed through a liquid nitrogen trap and desiccator before reaching the cell body. The initial spectrum of the calcined catalyst was measured at this time, with the background spectrum subtracted. Purified 2,4,6-trimethylpyridine was flowed at 0.06 mL h^{-1} to the sample cell. FTIR spectra (64 scans, 4 cm^{-1} resolution, scan range from 4000 to 1000 cm^{-1}) were saved continuously at different time intervals during the duration of the experiment: every 30 s for the first 30 min, then every 10 min for the rest of the experiment.

The MTH reaction was carried out in a 0.25 in. stainless steel tube installed in a Thermo Fisher furnace, equipped with a temperature controller. All catalysts (40 – 60 mesh size) were diluted with silica gel (Davisol Grad 636; 35 – 60 mesh size) and held between two plugs of quartz wool. A K-type thermocouple (Omega Engineering) was inserted into the stainless tube to measure the temperature of the bottom of the catalyst bed. Prior to the reaction, the catalyst bed was pretreated *in situ* at 550°C for 3 h under flow of dried air (Matheson, 6 cm^3 min^{-1} of O_2, 24 cm^3 min^{-1} of N_2). The catalyst bed was then cooled to the reaction temperature, 350°C. Methanol was fed by a syringe pump (Harvard Apparatus) into a heated inert gas stream of Ar (Matheson, UHP) to achieve a methanol partial pressure of 11.5 kPa. The molar space velocity was varied in the range of 0.5 – 1.8 s^{-1} to achieve different contact times. The first data point was collected after 20 min time on stream (TOS) at three different contact times for each sample. The reaction effluent was evaluated using an on-stream gas chromatograph (Agilent 7890B) equipped with an FID detector and an Agilent DB-1 capillary column. Methanol and dimethyl ether (DME) are considered as reactant with the conversion X defined as

$$X = \left[1 - C_{eff}/C_{feed}\right] \times 100\% \qquad \text{5-2}$$

where C_{eff} is the concentration of both methanol and DME in the effluent and C_{feed} is the concentration of methanol in the feed. The selectivity S_i of hydrocarbon product *i* is defined as

$$S_i = \left[C_i / C_{t,eff}\right] \times 100\% \qquad \text{5-3}$$

where C_i is the concentration of hydrocarbon *i* in the effluent and $C_{t,eff}$ is the total concentration of hydrocarbons in the effluent. Linear regression was performed on initial conversion versus contact time (τ) curves and conversion versus time-on-stream curves to obtain dX/dτ and dX/dt, respectively. Site loss yield was calculated using the following equation [43]:

$$-\frac{d\tau}{dt} = \frac{dX/dt}{dX/d\tau} \qquad \text{5-4}$$

where dX/dt and dX/dτ are the slopes from the linear regressions.

5.4. Results and Discussion

In the following sections, we first focus on the design of ZSM-11 core-shells with varying siliceous shell thickness and systematically examine the impact of this configuration on catalytic performance. We test the hypothesis that siliceous shells have benefits beyond surface passivation of external acid sites by impacting mass transport properties. This analysis is then extended to ZSM-5 to determine if secondary growth of a shell has a comparable effect on its overall catalytic performance. These studies are complemented by diffusion measurements to validate the effects of shell growth on internal diffusion. Lastly, we explore whether the reverse egg-shell configuration mimicking pseudo nanosheets for both MEL and MFI is capable of reducing diffusion limitations, irrespective of their relatively high percentage of external acid sites.

ZSM-11@silicalite-2 core-shell catalysts (Figure 5-1a) were prepared by secondary growth of a silicalite-2 shell (Si/Al = ∞) on a ZSM-11 core (Si/Al = 30 from EDS) using a previously reported protocol for zeolite MFI [45] as a guide for seeded growth. For all syntheses we used ZSM-11 seeds (sample C-30) with an apparent dimension of 300 nm in the [100] direction (Figure 5-1b). Sample C-30 was synthesized using 1,8-diaminooctane (DAO) as the organic structure-directing agent to produce high yield of pure MEL-type zeolite without any detectable MFI impurity [46]. Secondary growth of seeds was accomplished in siliceous growth mixtures where the silica concentration was adjusted to generate core-shell catalysts with a range of shell thickness.

We prepared three ZSM-11@silicalite-2 catalysts, referred to herein as samples CS-x where *x* is the Si/Al ratio of the shell measured by laboratory XPS. Table 1 lists the physicochemical properties of C-30 (ZSM-11 core) and three core-shell samples (CS-60, CS-91, and CS-133) after ion-exchange with NH_4^+ ions and calcination to generate H-form zeolites. Textural analysis (Fig. S2) revealed nearly identical total surface area (BET S_A) and micropore volume (V_{micro}) for all samples. The concentration and speciation of acid sites were quantified by a combination of techniques. Solid state ^{27}Al NMR was used to estimate the percentage of extra-framework aluminum (EFAl). Ammonia temperature programmed desorption (NH_3-TPD) was used to calculate the total acid site concentration, C_{acid}. The percentage of acid type, Brønsted (B) vs. Lewis acid (L), was estimated by pyridine adsorption Fourier transform infrared (FTIR) spectroscopy, noting that differences in Lewis acid content measured by FTIR and NMR can differ based on several factors that include the presence of various non-framework Al species and/or hydrated species [5]. As expected, C_{acid} values for ZSM-11@silicalite-2 samples monotonically decreased with increasing silicalite-2 shell thickness, but the percentages of each acid type were relatively constant. FTIR measurements also showed that silicalite-2 shell growth did not contribute to the formation of internal silanol defects (Fig. S3), which were evident in spectra (around 3500 cm^{-1}) [55, 56] for ZSM-11 zeolites prepared with higher silicon content than the core (e.g. samples H-45 and H-55 where the nomenclature H-x denotes homogeneous distributions of Al sites with *x* referring to the Si/Al ratio measured by EDX).

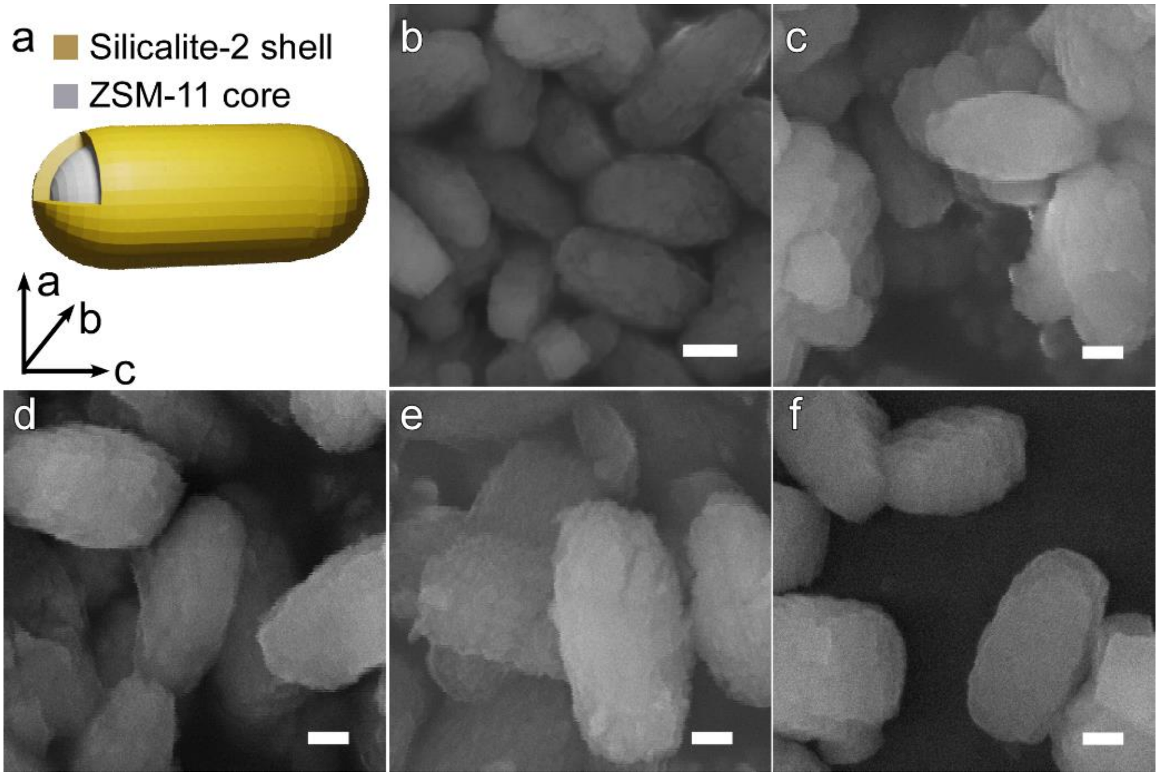

Figure 5-1. (a) Scheme of a ZSM-11@silicalite-2 core-shell particle where the silicalite-2 shell (gold) is epitaxially grown on the surface of a ZSM-11 crystal seed (gray).

(b-f) Scanning electron micrographs of the (b) C-30 core used in the preparation of three core-shell samples: (c) CS-60, (d) CS-91, and (e) Cs-133. (f) SEM image of a ZSM-11 particle (sample H-55) with homogeneous Al distribution and a higher Si/Al ratio than the core (see Fig. S1 for an image of H-45). Scale bars equal 200 nm.

Scanning electron microscopy (SEM) images confirmed that seeded growth of silicalite-2 shells did not alter the morphology of ZSM-11 seeds (Figure 5-1b-e). Comparison of SEM images for core-shell samples to that of the core confirmed that shell thicknesses were all less than 50 nm; however, subtle differences in shell thickness for each of the three core-shell samples was difficult to distinguish by electron microscopy. The anisotropic rod-like shape of crystals also precluded the use of more sensitive techniques, such as dynamic light scattering (DLS), to detect small changes in particle size after secondary growth. Indirect confirmation of shell thickness was achieved by the change in surface Si/Al ratio measured by XPS. In order to extract Si/Al ratios as a function of depth, we conducted variable kinetic energy XPS (VKE-XPS). As shown in Figure 5-2, the Si/Al ratio is reported for each sample as a function of both photon energy (bottom x-axis) and estimated information depth (top x-axis). The first approximate 10 nm of depth is associated with a carbon coating that was applied to each sample for the purpose of minimizing the effects of charging. This data confirms the increase in shell Si/Al ratio with a concomitant increase in shell thickness (CS-133 > CS-91 > CS-60) where information depth analysis confirms an approximately shell thickness of ca. 15 nm for CS-60, whereas values for the other two core-shell samples are unresolved due to limits in XPS depth analysis. These findings also reveal that secondary growth does not result in pure silicalite-2 owing to the possible reallocation of aluminum from the seed (core) to the shell during hydrothermal synthesis, consistent with an observed decrease in EFAl for core-shell samples compared to the parent core (Table 1). As such, the shell never achieves complete surface passivation, although the concentration of Al sites in the shell are diluted by as much as four-fold compared to the seed.

Table 5-1. Physicochemical properties of H-ZSM-11 samples prepared for catalytic testing.

Sample[a]	R^2/D (ks)	BET S_A (m^2/g)	V_{micro} (cm^3/g)	C_{acid}[b] (μmol/g)	Acid type[c] (%)		EFAl[d] (%)	$-d\tau/dt$ (mol_{H+}/mol_C)
					B	L		
C-30	0.22	427	0.14	302	85	15	9	501
CS-60	0.08	420	0.14	273	89	11	3	74
CS-91	0.08	403	0.14	243	90	10	0	439
CS-133	0.17	437	0.15	210	84	16	9	885
H-45	0.12	408	0.14	244	77	23	14	550
H-55	0.30	427	0.14	193	73	27	4	377

[a]C-X = core (ZSM-11) and CS-X = core-shell (ZSM-11@silicalite-2), where X = Si/Al from XPS, whereas H-X = homogeneous ZSM-11 where X = Si/Al from EDX; [b]NH_3 –TPD; [c]Measured by pyridine FTIR where B = Brønsted acid sites and L = Lewis acid sites; [d]Measured by ^{27}Al MAS NMR, Fig. S4. Variables refer to the diffusional timescale (R^2/D), total surface area (BET S_A), microporous volume (V_{micro}), total acid site concentration (C_{acid}), extra-framework aluminum (EFAl), and site-loss yield ($d\tau/dt$).

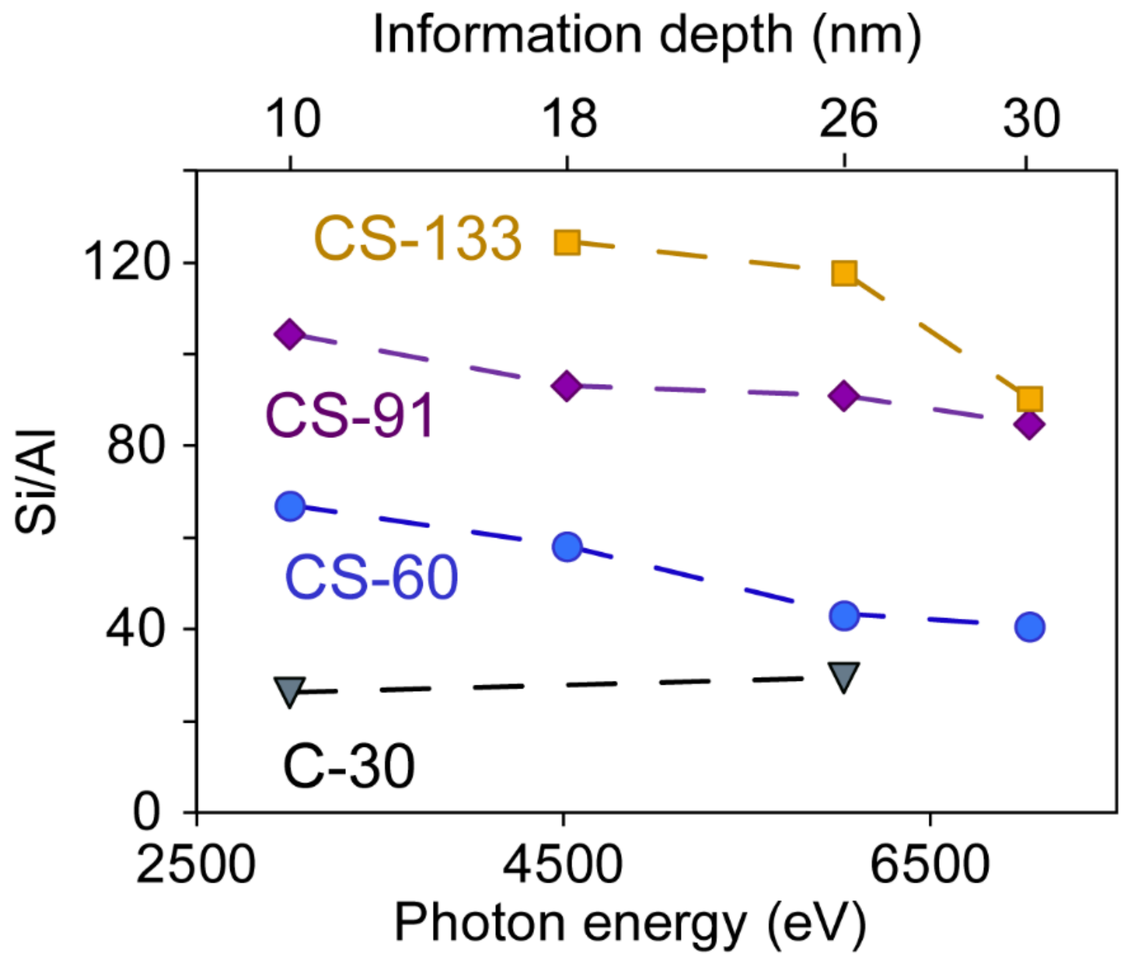

Figure 5-2. Comparison of Si/Al ratios for the ZSM-11 core (C-30) and core-shell samples (CS-60, CS-91, and CS-133) from XPS depth analysis (VKE-XPS) as a function of photon energy (bottom x-axis) and the corresponding information depth (top x-axis) where 95% of the signal is generated.

Each sample was pre-coated with ca. 10 nm of carbon. Any uneven (or rough) surfaces of zeolite powders from VKE-XPS sample preparation increase the uncertainty in depth estimation for a single particle. This results in a diffuse transition between shell and core that creates uncertainty in estimates of shell thickness.

The performance of H-form ZSM-11 and ZSM-11@silicalite-2 catalysts was assessed using the MTH reaction at sub-complete methanol conversion. Catalytic testing was conducted in a fixed bed reactor at 350°C with a molar hourly space velocity that was varied to achieve a starting conversion in the range of 50 to 70%. Conversion (X) versus time-on-stream (t) curves in Figure 5-3a exhibit variable rates of deactivation, or slopes listed as dX/dt, spanning an order of magnitude among all catalyts tested (ranging from 0.03 to 0.20 h^{-1}). Similar reactions were performed at varying space velocity (Figure 5-3b) to assess changes in the initial conversion as a function of contact time, □. Comparisons are made for C-30 core (inverted gray triangles), a ZSM-11 catalyst with higher Si/Al ratio and homogeneous Al distribution (sample H-55, red triangles), and core-shell samples CS-60 (blue circles), CS-91 (purple diamonds), and CS-133 (gold squares). The slopes of initial conversion versus contact time, dX/d□, range from 0.5 to 1.4 s^{-1} for all tested catalysts.

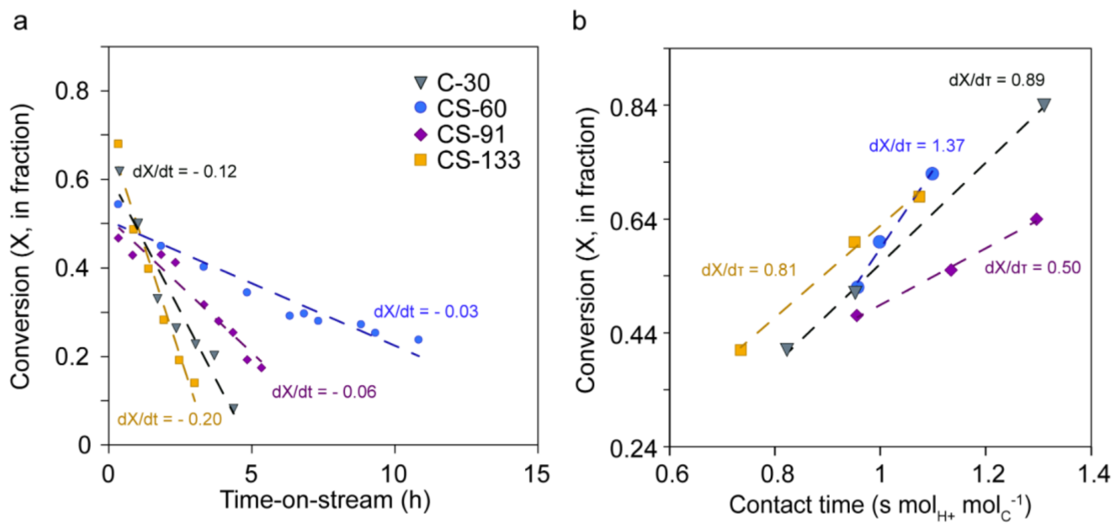

Figure 5-3. MTH reactions over ZSM-11 catalysts at 350°C and P_{MeOH} = 11.5 kPa.

(a) Fractional conversion of reactant (methanol and dimethyl ether) plotted as a function of time-on-stream, t. (b) Initial conversion (at t = 20 min) plotted as a function of contact time τ (s mol_{H+} mol_C^{-1}). Corresponding plots for homogeneous samples H-45 and H-55 are provided in Fig. S3.

Janssens and coworkers [57] suggested that the use of rates of decreasing sub-conversion with time, defined as dX/dt, as an assessment of catalyst deactivation in the MTH reaction is convoluted based on its inability to distinguish between loss of active sites and the intrinsic activity of sites. Bhan and coworkers [43] examined a commercial ZSM-5 catalyst to expand upon the model introduced by Janssens wherein they empirically determined the quantity d□/dt, which is the ratio of slopes dX/dt (Figure 5-3a) and dX/d□ (Figure 5-3b). The physical significance of d□/dt is a site-loss yield, or mole of H^+ loss for every mole of reactant fed (mol_{H+}/mol_{C}), which is posited to be a more accurate parameter for comparing non-selective deactivation of different catalysts [58]. The site-loss yield for each catalyst in this study (Table 1) reveals that ZSM-11@silicalite-2 with the thinnest shell (CS-60) loses active sites at a rate seven-times less than the ZSM-11 core (C-30). As the thickness of the shell increases, the absolute value of d□/dt monotonically increases such that the core-shell catalyst with the thickest shell (CS-133) loses active sites at a rate 1.8-times greater than the parent ZSM-11 catalyst, indicating thin shells markedly improve catalyst lifetime while thick shells can have a deliterious effect on catalyst performance.

The performance of ZSM-11@silicalite-2 catalysts can be impacted by several factors, which include (but are not limited to) dilution of total acid sites or mass transport effects imposed by defects, such as pore blockage as a result of misoriented or incomplete shell growth. Mass transport was assessed by two techniques: the first described here and the second discussed latter. The first approach used to examine diffusion limitations in zeolite catalysts was adapted from Bhan and coworkers [59] wherein the diffusional timescale R^2/D was estimated from transient adsorption of the probe molecule 2,3-dimethylbutane (Fig. S5). Values of R^2/D for all core-shell catalysts (Table 1) are less than the core, indicating the addition of a siliceous shell reduces diffusion limitations. There is a nearly three-fold reduction in R^2/D for core-shells CS-60 and CS-91, whereas CS-133 has a value that is only slightly less than the core. This indicates that thicker shells generated by secondary growth in more concentrated media can have a detrimental impact on mass transport with the concomitant loss of catalyst peformance. Indeed, this is consistent with larger values of dX/dt (Figure 5-3a) and d□/dt (Table 1) for CS-133 relative to those of the parent core (C-30).

One outcome of core-shell preparation is the dilution of total acid sites via the incorporation of a catalytically-inactive siliceous shell. In order to confirm that the enhanced performace of core-shell catalysts is atributed to the shell and not acid site dilution, the latter was assessed by preparing ZSM-11 catalysts with higher Si/Al ratios than C-30. To this end, we synthesized two ZSM-11 catalysts, H-45 and H-55, with homogeneous distributions of Al sites. All homogeneous catalysts (C-30, H-45, and H-55) exhibit shorter lifetimes (or higher |dX/dt|) than the best performing core-shell catalyst (CS-60), which indicates ZSM-11@silicalite-2 outperforms ZSM-11 over a range of Si/Al ratios. Moreover, the site-loss yield (d□/dt) for CS-60 is markedly less than any of the homogeneous catalysts (see Table 1), which confirms that the exceptional performance of CS-60 is not attributed to the dilution of acid sites.

To facilitate comparisons among catalysts with disparate properties, we used a general descriptor $C_{H^+}S_A^{-1}R^2/D$ that combines mass transport characteristics (R^2/D) with the BET surface area S_A and the Brønsted acid concentration C_{H^+} calculated as the product of C_{acid} (from NH_3 TPD) and the percentage of Brønsted acids (from pyridine FTIR). This approach is motivated by similar methodologies used by the groups of Bhan [59, 60] and Gascon [61] with slight modification. Here we compare MTH product selectivity (Figure 5-4) using the commonly reported ratio Ethene/2MBu comparing ethene, a characteristic product of the aromatic cycle, to the sum of 2-methylbutane and 2-methyl-2-butene (2MBu), which are characteristic products of the olefin cycle [40] in the hydrocarbon pool mechanism. Bhan and coworkers [51, 59] previously examined the effect of crystallite size and Al content for ZSM-5 catalysts on selectivity and reported that the Ethene/2MBu ratio decreased with decreasing crystallite size and increasing Si/Al ratio. The dual effect of crystallite size and Al content were combined into a single descriptor, similar to the one used here, representing the number of Al sites along a diffusion path length. Increases in both Al content and crystallite size increase the number of aromatic methylation/dealkylation events (i.e. interaction of methylbenzenes with acid sites), leading to higher ethene selectivity. This trend reported by Bhan (see Fig. S6 in the Supporting Information) is similar to the one we observe for zeolites prepared in this study, where the dashed line in Figure 5-4 is a fit to all homogeneous samples. Here we compare all homogeneous and core-shell MEL catalysts (Table 1) to those of MFI catalysts

(Table 2) that will be discussed later. The trend in selectivity as a function of the descriptor is consistent with the trend reported by Bhan, with the exception of two core-shell ZSM-11@silicalite-2 catalysts: CS-60 and CS-91.

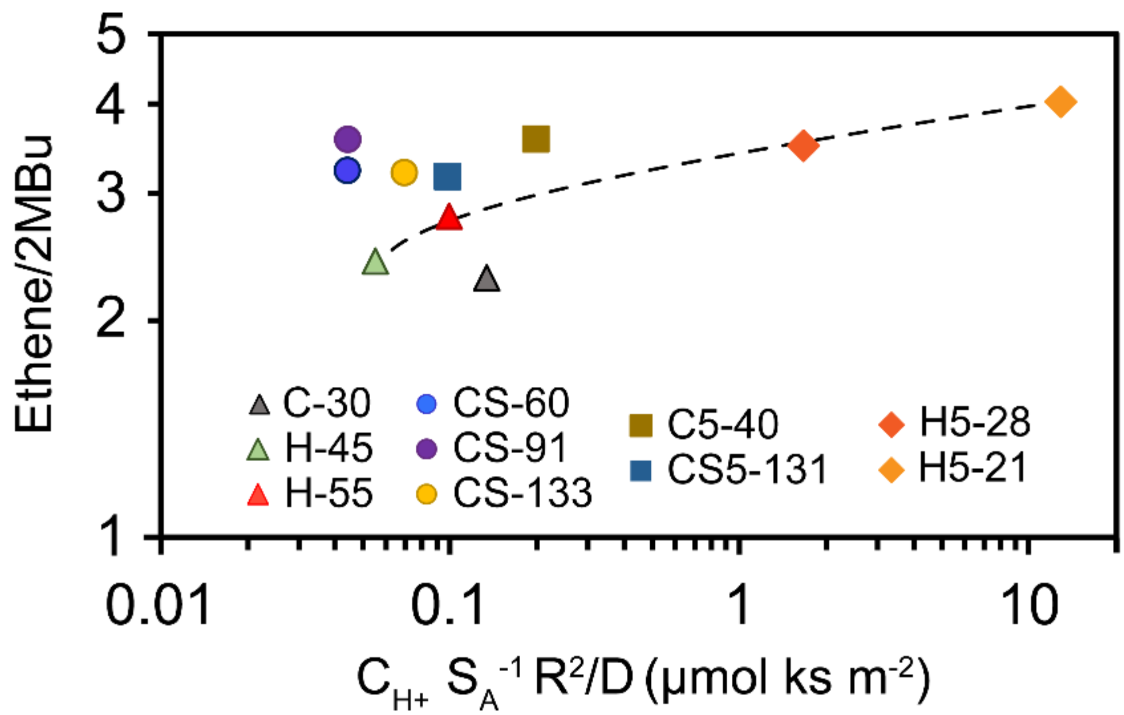

Figure 5-4. Ratio of Ethene/2MBu evaluated at sub-complete methanol conversion and early time-on-stream for MTH reactions as a function of the descriptor $C_{H^+}S_A^{-1}\,R^2/D$.

Triangles represent ZSM-11 catalysts with homogeneous Al distribution; circles represent ZSM-11 core-shell samples; squares represent ZSM-5 core and core-shell samples; and diamonds refer to ZSM-5 catalysts with homogeneous Al distribution (H5-28 and H5-21) synthesized according to reported protocols [45, 62] (see Table S1 for details). Selectivity profiles for a broader range of products in MTH reactions over select catalysts are provided in Fig. S7. The dashed line is a logarithmic regression fit to only the homogeneous MFI and MEL samples (C-30, H-45, H-55, C5-40, H5-28, and H5-21) according to the reported trend in Fig. S6.

The two outliers in Figure 5-4 are core-shell catalysts with thinner shells, which were shown to have longer catalyst lifetimes than that of their parent core (C-30). The larger Ethene/2MBu ratios of these two samples is more characteristic of zeolites with longer diffusion length (i.e. larger particle size) and/or higher overall acid site concentration [40, 51, 59]. A previous study of diffusion-free nanosheet

MFI showed that the aromatic cycle is not intrinsically promoted in this medium-pore zeolite [63]. Propagation of the aromatic cycle depends on the existence of active methylbenzene species (MBs) [51, 63]. Their entrainment within the pores leads to a higher degree of alkelation/dealkelation events toward higher ethene selectivity and Ethene/2MBu ratio; however, from our measured diffusion timescale (R^2/D) using 2,3-dimethylbutane, it can be seen that all core-shell samples exhibit improved diffusion (i.e. smaller R^2/D) compared to the parent core C-30. We posit these differences are due to factors associated with complex diffusion in zeolite pores. It is possible that while the core-shell configuration improves diffusion of small molecules, it imposes diffusional constraints on larger species (e.g. aromatics). The longer residence time of the active MBs allow for promotion of the aromatic cycle, which is reflected in the higher Ethene/2MB ratios of the core-shell samples. This qualitatively agrees with the trends discussed from mass transport measurements of core and core-shell catalysts using a bulkier probe molecule.

The broader applicability of core-shell design by post-synthesis modification was demonstrated for the zeolite MFI framework. We synthesized a ZSM-5@silicalite-1 core-shell catalyst (Figure 5-5a and S8) using an established seeding method [45] wherein a shell of silicalite-1 (siliceous ZSM-5) was epitaxially grown on a ZSM-5 parent crystal (core) with Si/Al = 40 (measured by EDS). Using similar naming conventions, we refer to the core as sample C5-40 and the core-shell as sample CS5-131 with corresponding physicochemical properties listed in Table 2 (see also Fig. S9). The parent ZSM-5 core was synthesized according to a reported protocol [45] to achieve relatively monodisperse spheroidal crystals, which enabled facile quantification of shell thickness by DLS. Comparison of the hydrodynamic diameter of the core-shell sample relative to its parent core revealed an average shell thickness less than 5 nm, which is close to the resolution limit of DLS (ca. 3 nm).

Table 5-2. Physicochemical properties of H-ZSM-5 and egg-shell catalysts.

Sample[a]	Zeolite	R^2/D (ks)	BET S_A (m^2/g)	V_{micro} (cm^3/g)	C_{acid}[b] (μmol/g)	Acid type[c] (%) B	Acid type[c] (%) L	EFAl[d] (%)
C5-40	MFI	0.35	518	0.14	435	68	32	4
CS5-131	MFI	0.22	516	0.15	327	71	29	4
ES5-16	MFI	0.31	440	0.12	193	79	21	6
ES-27	MEL	0.88	430	0.14	101	76	24	---

[a]C5-X = ZSM-5 core, CS5-X = core-shell (ZSM-5@silicalite-1), ES5-X = egg-shell (silicalite-1@ZSM-5), ES-X = egg-shell (silicalite-2@ZSM-11) , where X = Si/Al from XPS (or ICP-OES for C5-40); [b]NH_3–TPD; [c]Measured by pyridine FTIR where B = Brønsted acid sites and L = Lewis acid sites; [d]Measured by ^{27}Al MAS NMR, Fig. S10. Variables refer to the diffusional timescale (R^2/D), total surface area (BET S_A), microporous volume (V_{micro}), total acid site concentration (C_{acid}), and extra-framework aluminum (EFAl).

VKE-XPS measurements were performed to quantify the Si/Al ratio of MFI samples as a function of depth (Figure 5-5c). The parent core (C5-40) had a constant value with depth as expected owing to the homogeneous Al distribution. The core-shell sample (CS5-131) had a decreasing Si/Al with increasing depth where the apparent thickness was 15 – 20 nm. The discrepancy in shell thickness from VKE-XPS compared to DLS can be attributed to multiple factors, which include potential dealumination of the core in its outer rim during shell growth or more likely the uneven (or rough) surface of zeolite powder from VKE-XPS sample preparation that increases uncertainty in depth estimation for a single particle. However, the overall trends observed in VKE-XPS were consistent with the expected compositional gradients of a core-shell zeolite. Similar to MEL core-shell samples, this data also confirmed that secondary growth during the preparation of ZSM-5@silicalite-1 results in a shell that is not pure silicalite-1 but is diluted nearly three-fold in Al concentration compared to its parent core.

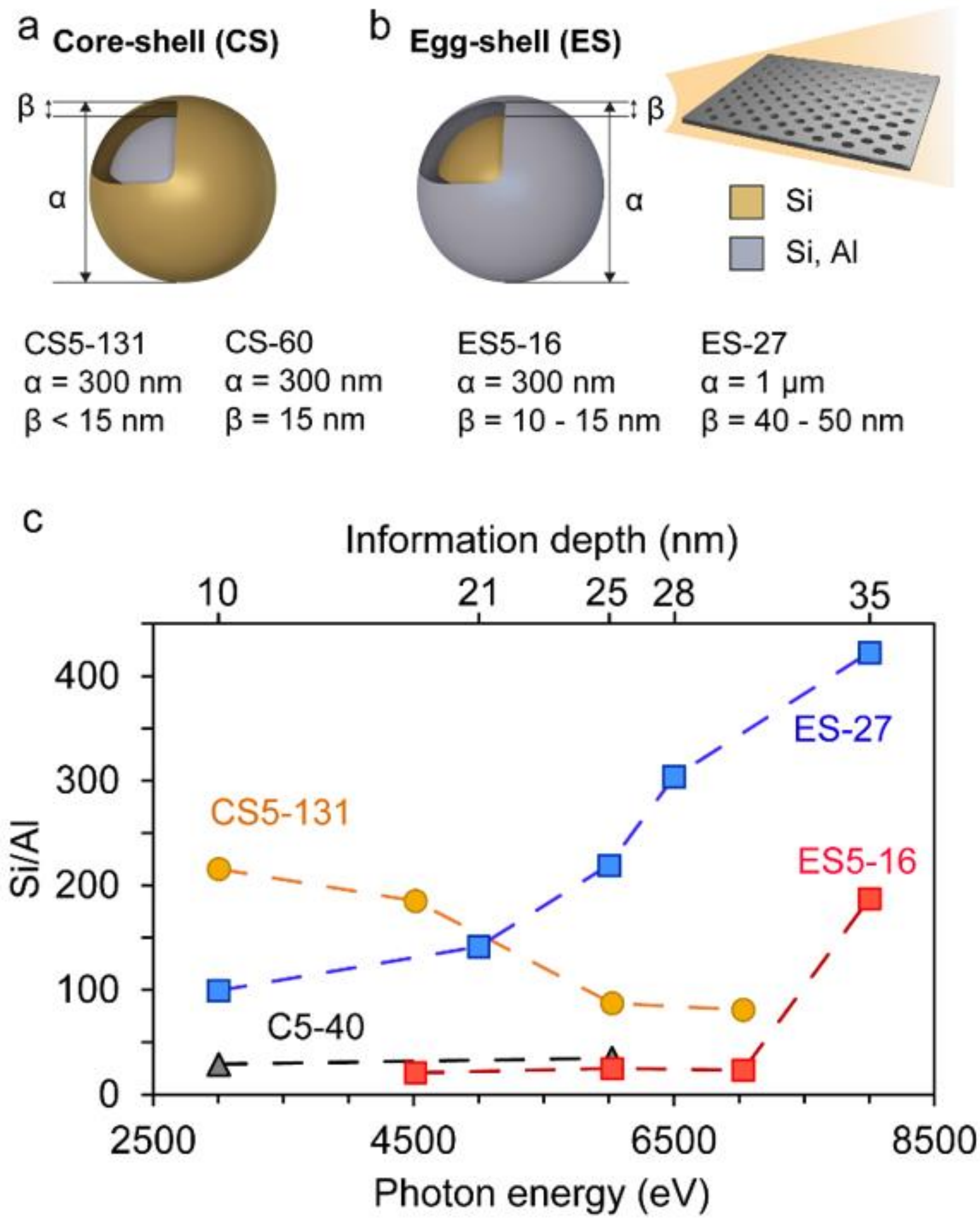

Figure 5-5. (a) Illustration of a core-shell catalyst where the shell is comprised of either ZSM-11 (CS-60) or ZSM-5 (CS5-131).

The latter was prepared using parent core C5-40. (b) Illustration of an egg-shell catalyst where the shell is comprised of either silicalite-2 (ES-27) or silicalite-2 (ES5-16). Inset: idealized rendering of the exterior rim of an egg-shell as a pseudo nanosheet. Approximate dimensions of the shell (size α) and core (size β) are listed for each MEL and MFI catalyst. (c) Comparison of Si/Al ratios for ZSM-5 (core and core-shell) and egg-shell catalysts from VKE-XPS as a function of photon energy (bottom x-axis) and the corresponding information depth (top x-axis). Each sample was pre-coated with ca. 10 nm of carbon.

Catalyst testing was performed at sub-complete methanol conversion (<60%) to assess the relative performance of MFI core and core-shell samples. We observed that the introduction of a thin silicalite-1 shell (CS5-131) resulted in a two-fold increase in catalyst lifetime (Fig. S11) compared to the parent ZSM-5 core (C5-40). While this trend is consistent with core-shell MEL catalysts (Figure 5-3a), the improvement in lifetime was less than the four-fold increase observed for MEL samples (e.g., CS-60 vs. C-30). This disparity is not likely due to differences in siliceous shell thickness since CS5-131 has a thinner shell than CS-60. We posit the dominant factor pertains to larger differences in mass transport within MEL and MFI core-shells. For instance, comparison of R^2/D values for core-shell and core samples reveals a 64% reduction for MEL and only a 37% reduction for MFI, which suggests that a larger number of defects may be generated in the growth of silicalite-1. This trend was also reflected in calculations of total turnover number (TON) for MFI samples (Figure 5-6a) and MEL samples (Figure 5-6b) where the introduction of a shell produced two- and four-fold increases in TON, respectively. One consistent observation for both MFI and MEL was that the performance of a zeolite catalyst can be enhanced via post-synthesis modification to passivate external surfaces and introduce a siliceous exterior rim that reduces mass transport limitations, extends catalyst lifetime, and increases turnovers.

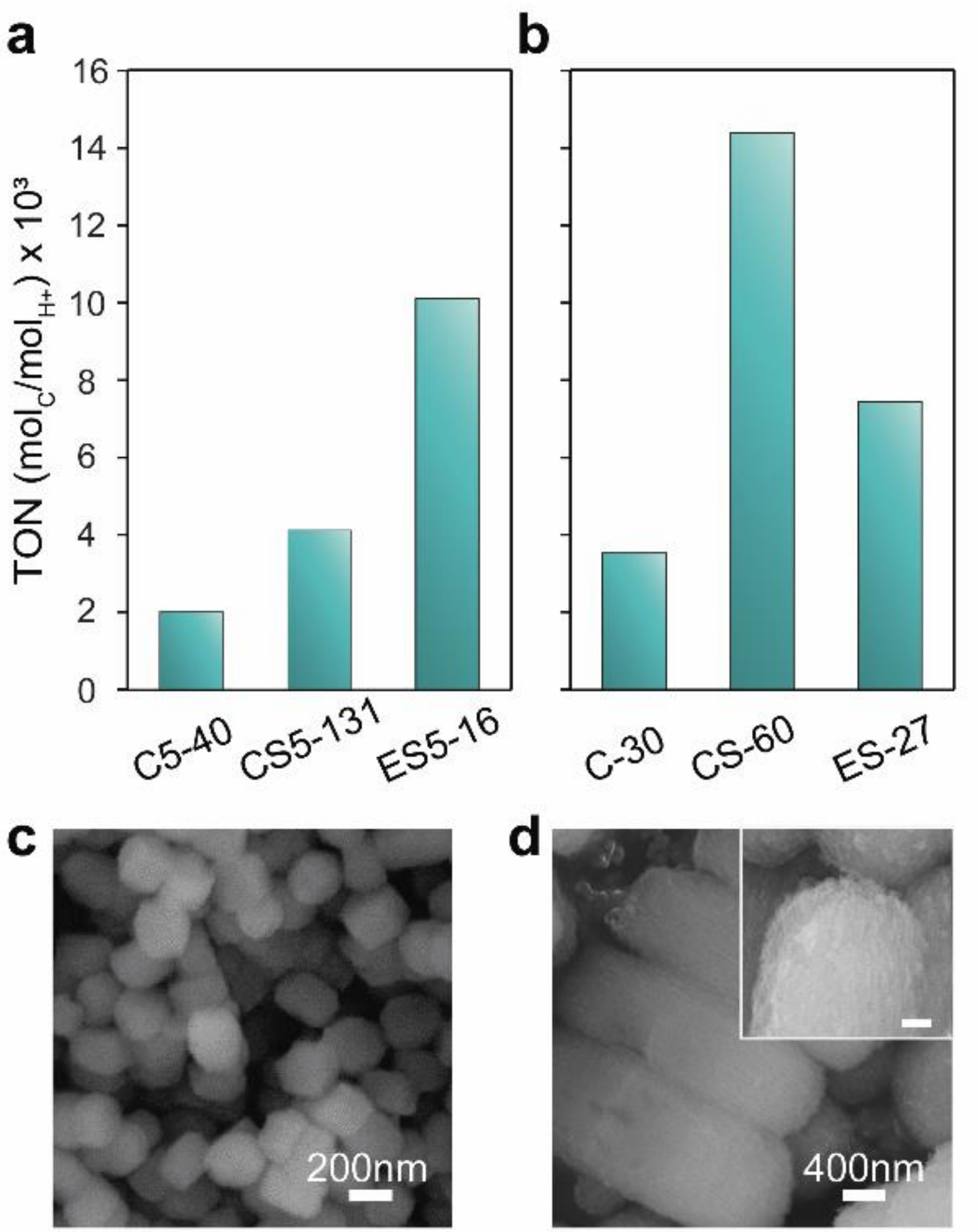

Figure 5-6. (a, b) Comparison of the total turnover number (TON) in MTH reactions at 350°C for the following samples: (a) MFI catalysts ZSM-5 (C5-40), ZSM-5@silicalite-1 (CS5-131), and silicalite-1@ZSM-5 (ES5-16);

(b) MEL catalysts ZSM-11 (C-30), ZSM-11@silicalite-2 (CS-60), and silicalite-2@ZSM-11 (ES-27). The shell thickness of MFI and MEL coreshell samples is approximately the same (see Figure 5-5) owing to the use of similar secondary growth media. (c,d) Scanning electron micrographs of egg-shell samples (c) ES5-16 and (d) ES-27. Inset in d: high resolution image showing an incomplete coverage of ZSM-11 on the silicalite-2 core for sample ES-27 (scale bar = 200 nm).

The mass-transport properties of core-shell catalysts (CS-60, CS-91, and CS-133) were compared with the parent core (C-30) using an experimental protocol to assess internal diffusion based on time-resolved FTIR spectroscopy. Similar to our previous study [21], the bulky organic base 2,4,6-trimethylpyridine (TMPyr) was used to slowly titrate Brønsted acid sites within the micropores of H-ZSM-11 over 8 to 72 h due to steric hindrance from the methyl groups. TMPyr titration was quantified by the disappearance of vacant Brønsted acid sites, associated with FTIR peak at 3605 cm^{-1} (Figure 5-7a, inset) and appearance of TMPyr-occupied Brønsted acid sites at 1565 cm^{-1} (Figs. S13 and S14). When the percentage of vacant Brønsted acid sites in ZSM-11 core and ZSM-11@silicalite-2 core-shell samples were plotted over time (Figure 5-7a), we observed a faster uptake in the homogeneous ZSM-11 core, with a delay in uptake for all three core-shell samples. The slopes of the fitted lines for Brønsted acid sites uptake (Fig. S15) show an order of magnitude difference.

The delayed uptake of TMPyr in core-shell samples can be attributed to the primary location of Brønsted acid sites. In addition to steric diffusion limitations of TMPyr, growth of a siliceous shell places a hydrophobic exterior rim in ZSM-11@silicalite-2, which also impacts molecular diffusion. Here, we refer to the logarithm of the octanol-water partition coefficient (log P) [64, 65], which is a common method of quantifying a molecule's hydrophobicity (log $P > 0$) or hydrophilicity (log $P < 0$). The probe molecule used to measure the diffusion timescale R^2/D (2,3-dimethylbutane, log $P = 3.6$) is more hydrophobic than TMPyr (log $P = 2.1$). Interactions between TMPyr and the hydrophobic silicalite-2 shell likely explain why diffusion is less rapid through the siliceous exterior of the zeolite particle. If we consider the MTH reaction, mildly hydrophilic reactant methanol (log $P = –0.7$) readily diffuses through the core-shell catalyst. This can be explained by the fact that methanol is much smaller than TMPyr, which allows for its diffusion through the siliceous shell without significant interaction with the zeolite framework. Indeed, prior molecular dynamics simulations have predicted that methanol diffusion is nearly four-fold faster in a siliceous zeolite compared to its aluminosilicate isostructure [66].

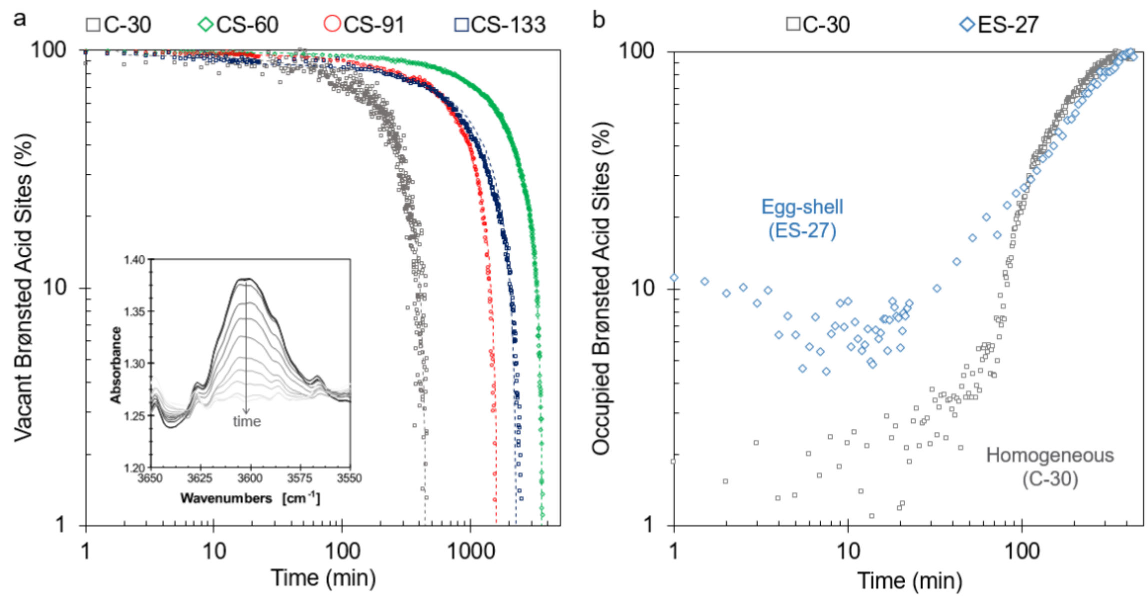

Figure 5-7. Time-resolved titration of Brønsted acid sites by TMPyr using FTIR spectroscopy.

(a) Temporal reduction in vacant Brønsted acid sites for MEL core (C-30) and core-shell samples (CS-60, CS-91, and CS-133). Symbols are experimental points and lines are model fits using the procedure described in Dai et al. [21]. Inset: FTIR spectra showing a decrease in the vacant Brønsted acid site peak at 3600 cm^{-1} with increasing time (indicated by the arrow). (b) Temporal increase in occupied Brønsted acid sites for MEL egg-shell (ES-27) and homogeneous ZSM-11 (C-30) samples.

The diverse species generated in the hydrocarbon pool likely exhibit disparate trends. For example, it has been experimentally and computationally verified that the degree of saturation (olefin vs. paraffin) impacts molecule diffusivity in zeolite pores as a function of Brønsted acid density [67, 68]. This indicates that hydrophobicity alone is an insufficient explanation for broader trends in diffusivity. Indeed, the interplay of zeolite composition and pore topology (specifically for MFI and MEL) on the diffusion of MTH products, such as ethene (log P = 1.3) and aromatics (e.g. benzene, log P = 2.2), is not fully understood, but is a topic we are investigating separately, outside the scope of this work.

Here, we consider an inverse core-shell design where a catalytically-active aluminosilicate shell is grown on an inactive siliceous core to generate an egg-shell configuration (Figure 5-5b). We hypothesize that egg-shells can function as pseudo nanosheets (Figure 5-5b, inset) that have advantages similar to those of nano-sized (<100 nm) and hierarchical zeolites reported in literature [47, 69-71], but with the added benefits that egg-shell syntheses can be performed with conventional organic structure-directing agents and the overall particle size (core + shell) is within the range of commercial zeolites, which simplifies post-synthesis separation of zeolites. Egg-shell MFI and MEL were synthesized by similar procedures using different organic structure-directing agents (see Experimental Methods for details). Samples will be referred to as ES5-x and ES-x, respectively (with *x* referring to the Si/Al measured by laboratory XPS). Growth of a ZSM-5 shell on a silicalite-1 core (ca. 300 nm) resulted in an egg-shell silicalite-1@ZSM-5 sample (ES5-16) with a 10 – 15 nm shell thickness measured by DLS. This thickness and the composition measured by laboratory XPS (Si/Al ~ 16) are in close agreement with the values estimated from VKE-XPS (Figure 5-5c). The formation of a relatively smooth shell was confirmed by SEM (Figure 5-6c), and a summary of all physicochemical properties are listed in Table 2.

Preparation of egg-shell silicalite-2@ZSM-11 involved a similar approach wherein a ZSM-11 shell was grown on a silicalite-2 core (ca. 1 μm in the b-direction), resulting in sample ES-27 (see Table 2 for a summary of its physicochemical properties). The thickness of the shell in ES-27 was estimated from VKE-XPS (Figure 5-5c) to be in the range of 10 – 20 nm. The electron micrograph of ES-27 shows roughened surfaces that indicate a discontinuous shell consisting of dispersed nano-sized ZSM-11 domains with widths around 40-50 nm in size based on SEM images (Figure 5-6d). The presence of a non-contiguous shell is consistent with differences in shell composition measured by laboratory XPS (Si/Al = 27) and VKE-XPS (Si/Al = 99) where the incomplete shell creates a heterogeneous surface comprised of both ZSM-11 and silicalite-2. Many synthesis conditions were tested (Table S2) without success for generating a contiguous shell layer, which suggests that the preparation of silicalite-2@ZSM-11 is more challenging than that of silicalite-1@ZSM-5.

Catalytic testing of egg-shell samples with the MTH reaction at identical conditions reveal enhanced lifetime for both MFI and MEL samples relative to their respective parent cores (refer to conversion vs. cumulative turnover in Fig. S11a and b, respectively). As shown in Figure 5-6a, the TON for ES5-16 is markedly higher than its core-shell analogue (CS5-131), and five-fold higher than homogeneous ZSM-5 (C5-40). This is consistent with our hypothesis that the egg-shell configuration behaves as a pseudo nanosheet with a catalytic performance that compares favorably (on a qualitative basis) with the performances of 2D ZSM-5 (ca. 3 nm) [69] and other nano-sized ZSM-5 catalysts [72]. Analysis of the MEL egg-shell (ES-27) reveals a more modest improvement in TON (Figure 5-6b) with a value that is two-fold higher than homogeneous ZSM-11 (C-30) but less than that of the core-shell (CS-60). The apparent activity of catalysts can be assessed on the basis of the space velocity required to achieve similar initial conversion among different samples. Reactions performed with MFI egg-shell ES5-16 at a molar space velocity of 0.77 s^{-1} resulted in similar starting conversion (Fig. S11) as reactions with C5-40 and CS5-131 at lower space velocities (0.43 and 0.54 s^{-1}, respectively), indicating a higher apparent activity for the egg-shell catalyst, which has around one-half the concentration of Brønsted acid sites (Table 2). This shows that placement of acid sites in the outer rim of the zeolite is an efficient design to extend catalyst lifetime without compromising activity. In the case of MEL egg-shell ES-27, reactions performed at a molar space velocity of 0.49 s^{-1} resulted in similar starting conversion (Fig. S11) as reactions with catalysts C-30 and CS-60 at a higher space velocity (ca. 0.78 s^{-1}). This indicates a lower apparent activity for the MEL egg-shell catalyst, which is consistent with its incomplete shell where the concentration of Brønsted acid sites (Table 2) is three-fold less than homogeneous ZSM-11 (Table 1), i.e. ES-27 has the lowest C_{acid} among all catalysts tested in this study. Despite this decrease in activity, the MEL egg-shell still outperforms its homogeneous counterpart.

Analysis of selectivity using the same approach in Figure 5-4 is not feasible for egg-shell samples given that measurements of R^2/D assess the entire particle, and not solely diffusion within catalytically active shells. The Ethene/2MBu ratios, however, follow the expected trend of decreasing values with reduced catalyst size: egg-shell (ES5-16) and homogeneous (C5-40) MFI have ratios of 2.6 and 3.6, respectively; and egg-shell (ES-27) and homogeneous (C-30) MEL have ratios of 1.9 and 2.3, respectively. It was also noted that the R^2/D value for MEL egg-shell is significantly higher than any other sample tested, which indicates that access to the silicalite-2 core is partially hindered by either incomplete crystallization of the ZSM-11 shell or misalignment between the shell and core that impede diffusion into the passivated core. A similar effect was reported by Bhan and coworkers [51] who intentionally deposited silica (i.e. silylation) on the external surfaces of MFI catalysts to block pores, thereby imposing mass transfer limitations in a manner equivalent to increasing particle size (or increasing R^2/D). The incomplete shell for silicalite-2@ZSM-11 does not completely block access to the core, which is reflected in the high micropore volume (Table 2). In addition, these apparent defects do not affect the overall catalytic performance of silicalite-2@ZSM-11, which is reflected in the enhanced lifetime and TON of egg-shell ZSM-11 relative to its homogeneous counterpart. Lastly, we performed time-resolved TMPyr titration experiments to assess diffusion properties of egg-shell MEL (Figure 5-7b), which showed no evidence of hindered diffusion in the ZSM-11 shell. Conversely, these measurements revealed significant fast uptake in ES-27 in the first 10 minutes, which can be attributed to the Brønsted acid sites in the outer shell of the catalyst. Interestingly, comparisons to hierarchical zeolites in our previous study [21] reveal that Brønsted acid sites are absorbed on a faster timescale for both egg-shell and finned zeolites (~10 min) relative to that of a self-pillared pentasil (SPP) zeolite (~100 min).

Collectively, our findings highlight the exceptional catalytic performance of the egg-shell design, which shows promise for developing ultra-thin zeolite catalysts with reduced mass transport limitations and/or enhanced activity.

5.5. Conclusions

In summary, we have shown that core-shell zeolites designed with a catalytically active aluminosilicate core and passive silicon-rich shell can markedly enhance catalyst performance in the MTH reaction. The lifetime and total turnovers of core-shell MEL and MFI zeolites increases by 2 to 4 times with the introduction of a siliceous zeolite. This enhanced performance cannot be attributed solely to surface passivation but does appear to strongly correlate with a reduced effective particle size relative to the parent core based on diffusion measurements showing that the siliceous shell reduces mass transport limitations. The exact mechanism for this effect remains elusive, but several possible explanations can be offered. The first is the impact of placing a hydrophobic shell at pore mouths, which alters diffusion of reactants and products in/out of zeolite pores. This may also contribute to reduced external coke formation due to a concomitant reduction in the accumulation of larger hydrocarbons (i.e. pre-coke species). This general phenomenon was reported for Si-zoned MFI [6], and likely applies to core-shell catalysts in this study to explain their extended lifetime relative to homogeneous counterparts.

Another possible explanation for the exceptional performance of core-shell catalysts is the removal of defective Al species during secondary growth of the shell. The nature of defect sites is diverse and often difficult to characterize, but can generally be categorized as species that deviate from full tetrahedral coordination or are distorted within the zeolite framework. Solid state ^{27}Al NMR measurements in this study showed no evidence of common defects sites, such as penta-coordinated Al. In the case of MEL core-shell catalysts, we did observe a decrease in extra-framework (octahedral-coordinated) Al species; however, this was not observed in the case of the MFI core-shell catalyst. If defects are too few to detect by NMR, it is possible that these sites may still impose restrictions on mass transport – particularly if the sites are located in the exterior rim to (partially) block molecule diffusion in/out of pore mouths. We have recently shown that ZSM-5 catalysts can be prone to the incorporation of defective Al species [53, 73], while another study reported the annealing of catalysts at hydrothermal conditions in dilute siliceous solutions at high temperature to improve zeolite crystallinity and concurrently catalyst performance [21]. Here, we used an identical annealing process to prepare all MFI catalysts.

To our knowledge, there is no prior report of the inverse egg-shell design presented here where both zeolites of identical crystal structure are combined with a passive siliceous core and catalytically active aluminosilicate shell. This design leads to pseudo nanosheets with enhanced total turnovers that, in the case of MFI, are 5-fold higher than the corresponding homogeneous ZSM-5, while the incomplete shell of MEL leads to slightly more than 2-fold increase. One of the key benefits of this synthesis approach is the use of conventional organic structure-directing agents, which is not possible in many reported methods to achieve either nano-sized or hierarchical MFI and MEL materials. The formation of the MEL egg-shell with a contiguous shell layer proved to be difficult. Conversely, the MFI egg-shell was generated through a facile process. We envision in the future that this process could be extended to organic-free ZSM-5 synthesis conditions, although generation of the silicalite-1 core is challenging without the use of organics. One addition benefit of the egg-shell design is that zeolite nanosheets are anchored to a support, which lends structure integrity to the catalyst that is generally lacking in other hierarchical zeolites. For all catalysts prepared in this study, the overall size is sufficiently large for facile separation and recovery of solids post-synthesis, which is more challenging for nano-sized zeolites.

Our findings indicate that both core-shell and egg-shell configurations effectively reduce diffusion limitations, with thinner shells leading to more enhanced catalyst performance. For core-shell catalysts, the exact role of the siliceous shell is not fully understood but is a subject of ongoing investigation. Likewise, continued development of synthesis methods to predictively control shell growth in both core-shell and egg-shell configurations has the potential to become a generalized platform for zeolite catalyst optimization that may be extended to other frameworks and composition

Chapter 6 – Dehydra-Decyclization of Tetrahydrofuran for Butadiene Across the Spectrum of Solid Acidity

*Reproduced with permission from C. Lee, M. A. Ardagh, G. Kumar, M. Shetty, O. Abdelrahman, M. Tsapatsis, P. J. Dauenhauer. Dehydra-Decyclization of Tetrahydrofuran for Butadiene Across the Spectrum of Solid Acidity. *In Prep* (2022).

6.1 Conspectus

Catalytic C-O bond cleavage and dehydration of tetrahydrofuran was evaluated for a set of progressively stronger solid acid catalysts. Strong acids, namely tungsten-based heteropoly acids, exhibited higher activity and selectivity towards butadiene production than more weakly acidic zeolites; enthalpic stabilization in the controlling transition state in butadiene formation contributed to a lower apparent activation energy barrier for stronger acids. The most weakly acidic phosphorus-based zeolite (P self-pillared pentasil, P-SPP) showed high selectivity to butadiene. Selectivity to products, mainly butadiene and propene, was controlled by the interplay of enthalpy-entropy contributions to dehydra-decyclization and retro-Prins reactions, respectively. In this balancing act, P-SPP is the least enthalpically stabilized but most entropically favourable in the butadiene formation reaction, resulting in the highly selective formation of butadiene.

6.2 Introduction

Conjugated dienes such as 1,3-butadiene are important building blocks in the production of synthetic rubber. Butadiene is a precursor in the production of elastomers, such as styrene-butadiene in car tires as well as non-elastomers, such as acrylonitrile-butadiene-styrene (ABS) plastic, that are constituents of automotive components like wheel covers and dashboards.[1,2] Almost all butadiene is currently produced as a byproduct of ethylene production via naphtha steam cracking.[1,3] However, as a consequence of the shale gas revolution in North America and the shift to methanol-to-olefins technology in the Asia-Pacific, the production of ethylene from lighter hydrocarbon feedstock and alternative chemistry has led to fewer side products and an inadvertent decline in butadiene production.[4] Thus, there is a clear motivation to fulfil the increasing disparity between dwindling butadiene supplies and the continuing growth in butadiene demand.[5]

Lignocellulose-derived chemical precursors present a renewable alternative to manufacture conjugated dienes and have gained interest in the sustainable chemical industry.[6] Ring opening of biomass-derived furfural derivatives, such as tetrahydrofuran (THF), yields platform chemicals such as succinic acid and isoprene (2-methyl-1,3-butadiene).[7] Examples of some acid-catalyzed reactions that form conjugated dienes include the hydrodeoxygenation of 2-methyl-THF to pentadienes over supported transition metal phosphides[8,9], boron-containing zeolites[10], and vanadium-titanium-phosphorus mixed oxides.[11]

The mechanism of ring-opening dehydration of cyclic ethers to C4 and C5 dienes has been the subject of recent studies to understand the sequence of ring opening and dehydration. Abdelrahman *et al.* reported high selectivity (99%) but low activity at all conversions of tetrahydrofuran to butadiene over phosphorus-containing siliceous self-pillared pentasil (P-SPP).[6] In addition to the main reaction to produce dienes, there are two side reactions: (i) ring opening without subsequent dehydration that produces the 2-butene-1-ol intermediate, and (ii) retro-Prins condensation that produces propylene and formaldehyde.[12] Due to its weak Brønsted acidity and enhanced stability,[13] P-SPP increased selectively to butadiene without promoting side reactions to propylene. However, P-SPP catalytic activity was significantly lower (~6X) than more conventional aluminosilicate zeolite catalysts. Similarly, dehydration and ring opening of cyclic ethers, such as 2-methyl-THF (2-MTHF) was evaluated; Kumbhalkar *et al.* described the dehydration of 2-MTHF to pentadienes over amorphous silica/alumina.[14] The proposed dominant pathway involved the joint process of hydride transfer and the dehydration of carbenium intermediates. Lastly, Witzke *et al.* noted that the isolation of Brønsted acid sites (BAS) on nickel phosphide catalyses C-O bond cleavage of 2-MTHF to form C5 dienes.[15]

Although prior studies have contributed understanding of the pathways and acid sites that catalyse the C-O bond scission of cyclic ethers, catalyst selection and optimization were limited by the absence of fundamental understanding of the relationship between acid strength and reaction pathway control. Heteropoly acids (HPA) present a tunable catalytic platform for dehydra-decyclization chemistry due to the capability for acid strength modification via substitution of its central and heteroatoms. The Keggin-type cluster is a HPA primary structure consisting of a heteropoly anion ($XM_{12}O_{40}^{n-}$) and a counter cation (H^+).[16] Other primary structures of HPA include the Dawson structure, a configuration with two units of heteropoly anion.[17] Variation of the selected structure and composition allows precise capability for synthesizing specific Brønsted acidity in solid catalytic materials, which are then evaluated for performance in the selective dehydra-decyclization of tetrahydrofuran to butadiene.

6.3 Results and Discussion

Here, we synthesized a series of siliceous MCM-41-supported Keggin-type HPA with tunable central (X = P^{5+}, Si^{4+}, Al^{3+}) and metal (M = W^{6+}, Mo^{6+}) atoms. Keggin-type HPA is composed of a central atom (X) tetrahedrally coordinated to four oxygens (O_c), which are surrounded by a metal (M) oxide cage that consists of three M_3O_{12} units.[16,17] There are four types of oxygen atoms, of which those relevant for Brønsted acid catalysis are the edge-sharing M-O_e-M bonds and the terminal M=O_t double bonds.[16–19] Brønsted acid sites in HPAs have shown catalytic activity in the polymerization of tetrahydrofuran, oxidation of methacrolein, and hydration of C3-C4 dienes.[17]

Keggin-type and Dawson-type structures exhibit differences in Brønsted acidity[17]. Based on XRD, Raman spectroscopy, solid state magic angle spinning (ssMAS) NMR, and Fourier transform infrared (FT-IR) spectroscopies, the Keggin-type isomer has been shown to be the thermally stable structure under ambient pressure and temperature conditions below 573 K.[17] As shown in Figure 6-1a, the intact MCM-41 structure was verified by XRD with the expected diffraction peaks at d_{100}, d_{110}, and d_{200} spacing.[20] XRD spectra of the supported HPA only depicted attenuated peaks assigned to the MCM-41 support. This suggests that the clusters of HPA were dispersed on MCM-41 and did not agglomerate into sufficiently large clusters detectable by X-ray diffraction. Additionally, the composition of the catalysts analysed by inductively-coupled plasma optical emission spectroscopy (ICP-OES) indicated 20-30 wt% of HPA supported on the siliceous MCM-41 (Table 6-1). Surface area and porosity determined by argon physisorption in Figure 6-1b were determined from the adsorption isotherm, shown in Table 6-1, indicating high surface area (>450 m^2) and ~30 angstrom pores. The isotherms indicate H1-type hysteresis loops, i.e. well-defined cylindrical pores, and the absence of micropores (< 2 nm in diameter). The total surface area and pore volume decreased after incipient wetness impregnation, suggesting that HPA clusters were deposited within the mesopores of Si-MCM41 and not solely on the particle external surface. The density of Brønsted acid sites (BAS) was measured via tert-butyl amine decomposition in a reactive gas chromatograph[21]; this density was used for calculating turnover numbers (TON) and acid site normalized catalytic reaction rates. The BAS count, noted as H^+ in Table 6-1, ranged from 150 to 190 μmol (g cat)$^{-1}$, indicating relatively uniform density of accessible sites by the probe molecule (tert-butyl amine) across all five HPA catalysts.

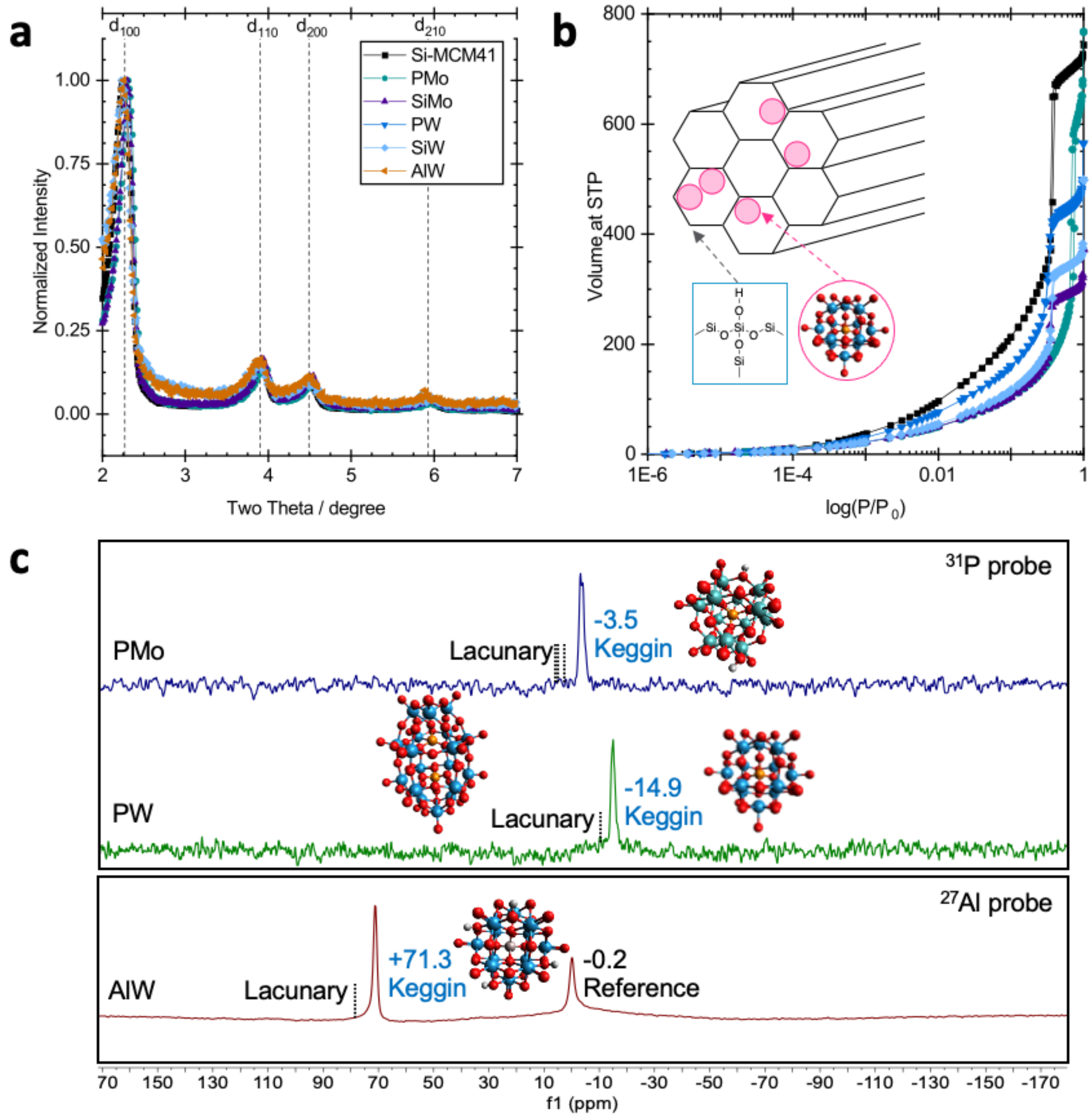

Figure 6-1. Figure 1. Heteropoly Acid (HPA) Catalyst Characterization.

(a) X-ray diffraction pattern with normalized intensity of the supported HPA only showed peaks assigned to the MCM-41 support. Diffraction pattern suggests that the clusters of HPA were dispersed onto MCM-41 and did not agglomerate into large enough clusters to be detectable by XRD. (b) Ar physisorption characterization, where an isotherm curve is drawn by filling the pores with Argon atoms at various pressure. The isotherms were H1-type hysteresis loops, indicating well-defined cylindrical pores and the absence of micropores (<20 angstrom in diameter). (c) ^{31}P MAS-NMR and ^{27}Al MAS-NMR of phosphorus containing and aluminum containing heteropoly acids indicating peaks corresponding to Keggin structures.

Table 6-1. Summary of catalyst characterization.

Catalyst	H^+ [μmol g^{-1}][a]	HPA content [wt%][b]	Accessible H^+ [mol H^+ (mol HPA)$^{-1}$]	Surface Area [m^2 g^{-1}][c]	Pore Volume [cm^3 g^{-1}][d]
Si-MCM41	-	-	-	966	1.2
H_3PW	174	22	2.3	740	0.9
H_4SiW	153	24	1.8	522	0.7
H_3PMo	188	28	1.3	451	1.0
H_4SiMo	138	25	1.0	468	0.6
H_5AlW	151	33	1.3	-	-

[a]Site count measured by tert-Butylamine (TBA) decomposition using reactive gas chromatography, assuming 1:1 TBA:H+; [b]Si, P, and Mo wt% determined using ICP-OES (performed by Galbraith Laboratories); [c]Calculated from Ar physisorption isotherm using multipoint Brunauer-Emmett-Teller (BET) equation on relative pressures from 0.05 to 0.3; [d]Calculated from Ar physisorption isotherm using Barrett-Joyner-Halenda (BJH) equation on the desorption branch.

The chemical structures of HPA catalysts were identified by solid-state magic angle spinning NMR with ^{31}P and ^{27}Al probes after incipient wetness impregnation synthesis (Figure 6-1c). Following existing protocols,[20,25] external references were selected as bulk phosphotungstic acid for ^{31}P MAS-NMR and aluminum chloride ($AlCl_3$-$6H_2O$) for ^{27}Al MAS-NMR and were set at δ of 0 ppm. Peaks at -3.5 ppm (PMo) and -14.9 ppm (PW) were assigned to P-O-M bonds indicating intact Keggin-type structures, as confirmed in literature.[20,25,38,39] Using ^{27}Al MAS-NMR, a peak at 71.3 ppm was assigned to Al-O-M bond of Keggin structures.[20,25,38,39] Literature values of ssMAS-NMR were not identified for Si-HPAs. To ensure that the Keggin structure remained intact at reaction conditions, ssMAS-NMR spectra were obtained with deactivated catalysts after reaction and showed similar peaks as the starting material (Figure S5).

The five heteropoly acid (HPA) catalysts for dehydra-decyclization of tetrahydrofuran were compared via experiment for trends in activity and selectivity (Figure 6-1). Tungsten-containing HPAs were significantly more active (~10X) and more selective (>75%) than molybdenum-containing HPAs in catalysing the main reaction of tetrahydrofuran to butadiene. W-HPAs rapidly deactivated on the time scale of 60 minutes (SI Figure S1). Additionally, due to the thermal instability of heteropoly acids above 573 K[20], the catalysts were not regenerated via steaming at 773 K.

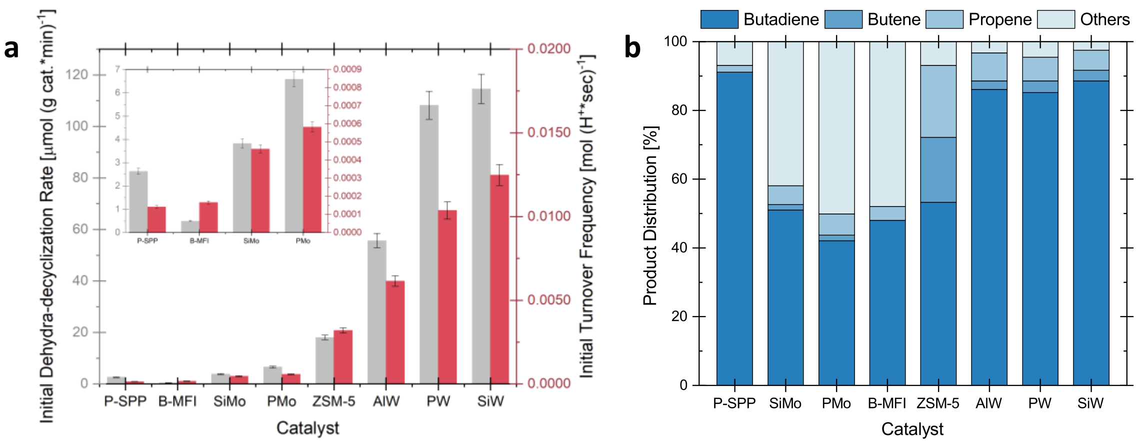

Figure 6-2. Tetrahydrofuran Dehydra-Decyclization Activity and Selectivity to Products.

(a) Initial rates of butadiene formation over HPAs (SiW, AlW, PW, PMo, SiMo), ZSM-5 and P-SPP. W-HPAs displayed significantly higher rates of formation of butadiene than Mo-HPAs. **(b)** Selectivity to C1-C4 products after flowing tetrahydrofuran over HPAs. W-HPAs displayed significantly higher initial selectivity to butadiene (>85%) than Mo-HPAs (>30%). Conditions: Temperature = 543 K; P_{THF} = 20 Torr; He = 30 sccm; weight hourly space velocity (WHSV) = 5 hr^{-1}; Conversion = 1 – 10 %; Carbon balance > 85%.

Non-zero initial selectivity to butadiene (>50%) at low conversion (<10%) suggests that butadiene is a primary product formed directly from THF (Figure 6-2b).[6] Additionally, experimental and computational studies of dehydra-decyclization of THF to butadiene over aluminosilicates has shown that the ring-opening of THF is the kinetically-controlling reaction step. In agreement with these aforementioned studies[6,10], C_3 (propene) and C_4 (butene) were also observed as primary products.

Specifically, an increase in the selectivity to propene and butene with HPA catalysts with time on stream suggests that these side products are formed via a secondary pathway (SI Figure S2 and S4). The increase of propene and butene products is more significant with Mo-HPAs, as there is a significantly lower activity and lower selectivity (<60%) to butadiene (Figure 6-2b). The initial selectivity towards butadiene over the highest activity catalyst (SiW) decreased from 90% to 70% over a period of 24 hours (10% to 0.2% conversion of THF). The time-on-stream selectivity to products of all HPA catalysts are included in Figure S4. When compared to commercial and P-SPP catalysts, tungsten-containing HPAs exhibited an order of magnitude higher normalized rate of butadiene production (~0.01 mol*$(H^{+}*s)^{-1}$ versus ~0.0005 mol*$(H^{+}*s)^{-1}$). Additionally, selectivity to butadiene over tungsten-containing heteropoly acids remained high at ~80%.

Isobaric experimental trials of tetrahydrofuran (THF) dehydra-decylization were conducted at low conversion of 1-10% (Figure 6-3a and b) with P-SPP, HZSM-5 (Si/Al 54), B-MFI (Si/B 39), and five HPA catalysts. Reaction kinetic experiments were conducted at higher temperatures of 533-573 K (260-300 ºC) than prior mechanistic studies[35] to enable measurable rates of the lowest activity catalysts for comparison with all materials at conditions relevant for industrial application. Consistent with Figure 6-2, site-normalized butadiene production rates in Figure 6-3a show that tungsten-containing HPAs catalysed significantly higher butadiene production rates and selectivity (>85%; calculated on a per carbon basis by dividing by the sum of products) than molybdenum-containing HPAs.

Apparent enthalpies and entropies of activation were calculated from the fitted slope and the intercept of the catalytic reaction rates, respectively, using the linearized Arrhenius equation,

6-1
$$ln\frac{k}{T} = -\frac{\Delta H^{\ddagger}}{R} * \frac{1}{T} + ln\frac{\kappa k_B}{h} + \frac{\Delta S^{\ddagger}}{R}$$

where k is the observed rate constant, T is the absolute temperature, $\Delta H^{\ddagger}$ is the enthalpy of activation, $\Delta S^{\ddagger}$ is the entropy of activation, κ is the transmission coefficient, k_B is the Boltzmann constant, h is the Planck's constant, and R is the gas constant.

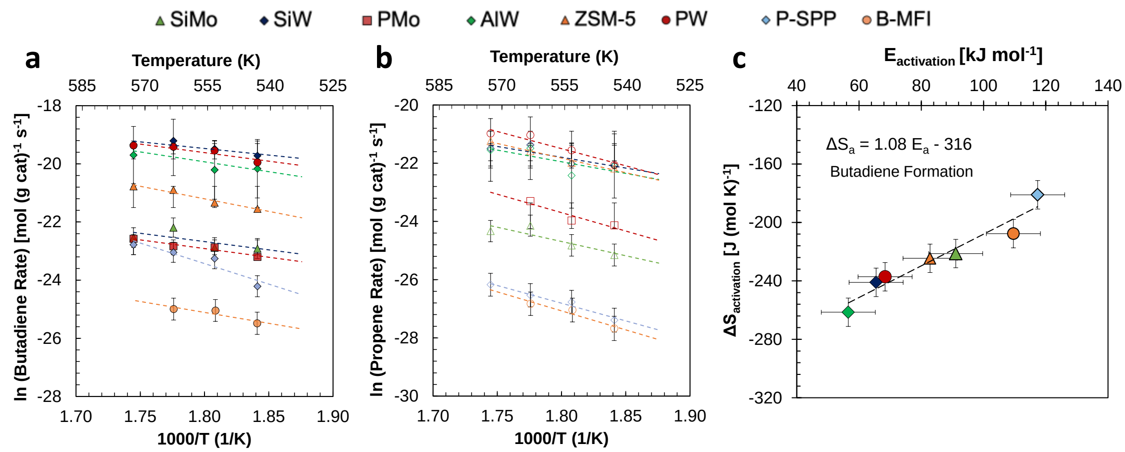

Figure 6-3. Kinetic Analysis of Solid Acid Dehydra-Decyclization of Tetrahydrofuran.

Arrhenius analysis using of the rates of formation of **(a)** butadiene and **(b)** propene. **(c)** Apparent activation entropy for butadiene formation plotted as a function of apparent activation energy, indicating a compensation effect between entropy and activation energy. By plotting the rates of product formation as a function of temperatures, apparent activation energies and entropies were obtained from the slope and intercept, respectively, using the linearized Arrhenius equation. Conditions: Temperature = 533 – 573 K; P_{THF} = 20 Torr; He = 30 sccm; weight hourly space velocity (WHSV) = 5 hr^{-1}; Conversion = 1 – 10 %; CB > 85%.

The kinetics of Figure 6-3 must be interpreted through the combination of elementary steps comprising the pathways from THF gas-phase reactant to products. For example, butadiene activation energy of ZSM-5 (Si/Al 54) measured here at 82$\pm$9 kJ mol^{-1} is lower than previous measurements with the same material at lower temperature (220-270 ºC)[35]. At lower temperatures used in prior mechanistic studies, high surface coverage of THF* led to low reaction order of THF(g), and the measured activation energy of 138$\pm$7 kJ mol^{-1} for ring-opening dehydration to butadiene matched the computed elementary step of THF* ring opening (140 kJ mol^{-1}). In the data of Figure 6-3 at higher temperatures, the reaction is not zero order in THF(g), as evidenced by experiments that reveal a shift in reaction rate with THF partial pressure (Fig. S6 in supporting information).

The catalytic rates and associated fitted apparent enthalpies and entropies in Figure 6-3 are thus a combination of at least THF adsorption energy and ring opening reaction kinetics for butadiene formation. Figure 6-3c depicts the apparent activation entropy for butadiene formation plotted as a function of apparent activation energy, indicating a linear compensation effect between apparent entropy and activation energy with slope of 1080 K^{-1}. The weakest solid acids (B-MFI, P-SPP) were at one extreme (high apparent E_a), while the strong solid acids were at the other extreme (low apparent E_a).

For more moderate conditions (533 – 573 K; 20 Torr THF partial pressure) and coverages (weight hourly space velocity of 5 hr^{-1}) as previous mechanistic studies of tetrahydrofuan (THF) dehydra-decylization over aluminosilicates[35], tetrahydrofuran C-O bond cleavage, i.e. ring-opening, is the rate-limiting reaction step on the active site of heteropolyacids. Under this assumption, the key steps in the mechanism controlling the overall rate can be described: (i) gas phase THF to adsorbed THF*, and (ii) adsorbed THF* to the transition state of ring-opened THF. By separating adsorption energies from intrinsic activation energies, both of which constitutes the components of apparent enthalpies and entropies, the apparent activation energies will be evaluated on a relative scale using a single descriptor, the deprotonation energy (DPE), across classes of Brønsted acid catalysts, ranging from aluminosilicates to heteropoly acids.

Heteropoly acids are appealing model systems for catalytic studies due to their uniform atomic arrangement and acid strength tunability. Neurock,[24–28] Iglesia,[29–34] and co-workers have quantified the acid strength of solid Brønsted acids, particularly among zeolite and HPA families, using density functional theory (DFT)-derived deprotonation energy. Deprotonation energy (DPE) is a probe-independent reactivity descriptor defined as the heterolytic cleavage of a proton and its conjugate base. When compared with HPAs (DPE range of 1080 – 1125 kJ mol^{-1}, zeolites substituted with heteroatoms Al^{3+}, Ga^{3+}, Fe^{3+}, B^{3+}) into the same framework have been shown to possess a similar range, albeit larger magnitude, of acid strength based on DPEs (1167−1214 kJ mol^{-1}).[28,33]

The apparent activation energies for the formation of butadiene decrease monotonically with the deprotonation energy (DPE) of the supported HPA, as shown by the filled in points in Figure 6-4a-b. Solid acids with higher DPEs also exhibited lower enthalpy of activation for butadiene formation. This suggests that the stability of the conjugate anion of the HPA stabilizes the ion-pair transition state of C-O bond cleavage, which is evidenced by the inverse dependence of ΔH_{app} on deprotonation energy. Because activation enthalpy reflects the relative bond strengths of the ground state and transition state, it makes sense that activation enthalpy trends with the deprotonation energy, which is the energy needed to remove the proton from its conjugate base. Activation energies for the rate of butadiene formation decreased with increasing DPE values.

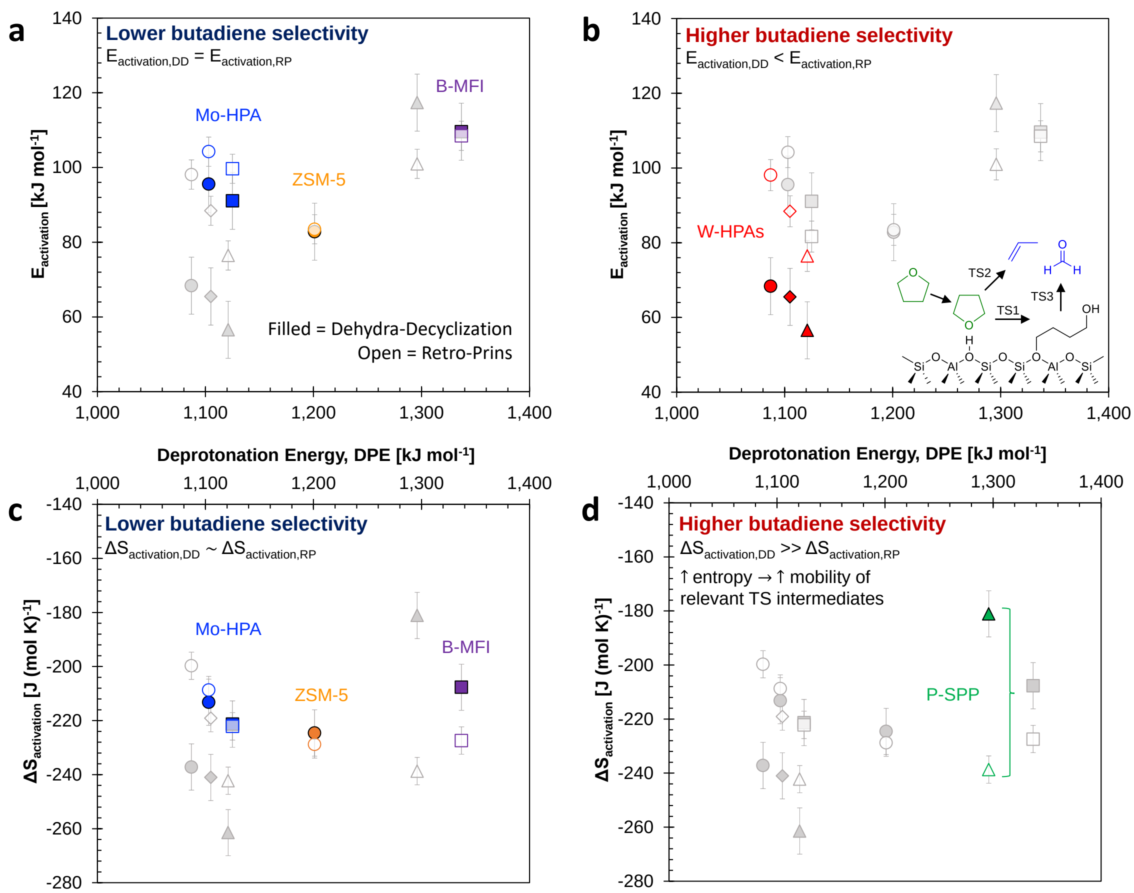

Figure 6-4. (a-b) Apparent activation energies and (c-d) entropies in the dehydra-decylization and retro-prins reactions as a function of deprotonation energy (DPE).

DPE is a computationally calculated descriptor of solid acid strength. A higher DPE indicates a relatively weaker acid strength. Conditions: Temperature = 533 – 573 K; P_{THF} = 20 Torr; He = 30 sccm; weight hourly space velocity (WHSV) = 5 hr^{-1}; Conversion = 1 – 10 %; Carbon Balance > 85%.

Previous microkinetic modeling and experimental study by Li *et al.* found that THF ring opening on H-ZSM-5 proceeds via two main reaction intermediates: surface alkoxide leading to the butadiene formation via dehydra-decyclization and C2-to-C3 hydride shift leading to retro-Prins products.[35] To compare the influence of deprotonation energies on the two competing pathways, dehydra-decyclization (DD) and retro-Prins (RP), we assessed the activation energies and entropies of butadiene and propene formation across the spectrum of solid acidity. Apparent activation energies for the retro-Prins reaction (the open points of Figure 6-4a-b), the main undesired side reaction, were 90 $\pm$ 15 kJ mol^{-1} across all relevant acid strengths. The trends were similar for pre-exponential factors, i.e. activation entropies, of each reaction (Figure 6-4a). This suggests that retro-Prins reaction rate is generally invariant of deprotonation energy, i.e. acid strength while strong acids such as HPAs enhance the catalytic formation of butadiene compared to weaker acids such as P-SPP. Therefore, although similar butadiene selectivities (~90%) were observed between HPA and P-SPP, the rates of butadiene formation were an order of magnitude higher on HPAs than on P-SPP. These results are consistent with Li *et al.*, which shows that overall THF reaction and selectivity are controlled by a reaction triangle consisting of three key transition states.[35] Butadiene selectivity changes considerably with the energy of transition state controlled by surface alkoxide formation, which is highly sensitive to the deprotonation energy. Although there are two key transition states relevant for retro-Prins products resulting from C2-to-C3 hydride shift, propene is predominantly formed via C3-C4 bond cleavage that occurs after the hydride shift.

To understand why P-SPP exhibited high butadiene selectivity compared to other zeolites, we further examine the enthalpy-entropy tradeoff in the stabilization of transition states of dehydra-decyclization and retro-Prins reactions. As mentioned, enthalpic factors are attributed to charge distribution in the transition state, which is the same for the rate-limiting step and evidenced by the catalysts falling in the same linear manner across deprotonation energies. However, entropic factors are complicated by different structural frameworks for the various catalysts, from the large-pores of MCM-41, to three-dimensional channels of ZSM-5, to self-pillared pentasils of P-SPP. Thus, the apparent entropic trends are not as clear. The apparent entropic energies of dehydra-decyclization and the main side reaction, retro-Prins, are compared with each other in **Figure 4**. We show that for molybdenum-based heteropoly acids, aluminum- and boron-zeolites, the apparent entropic barriers of dehydra-decyclization and retro-Prins are similar, leading to ~50% butadiene selectivity and ~40% propene selectivity. Conversely, for P-SPP, the apparent entropic barrier for dehydra-decyclization is significantly lower than that of retro-Prins. We posit that the relatively more favorable entropic barrier for butadiene formation results from the weakly acidic nature and structural framework of P-SPP, leading to increase mobility of the relevant transition state intermediates. Rate indifference with decreasing oxidation states of the central atom indicate similar charges and ionic character in the relevant transition state (*i.e.*, the transition state of the rate-determining step occurs on M-O instead of X-O sites). These results are consistent with the deprotonation energies (DPE) of W-HPA and Mo-HPA having different ratios between ionic and covalent characters that can contribute to the stability of the transition states.

6.4 Conclusions

Based on these results, future work will include the combination of kinetic studies with theoretical investigations using density functional theory to assess free energies and plausible elementary steps. Compared to the previously best performing catalyst (Phosphorus SPP) and conventional zeolite (ZSM-5), tungsten-based heteropoly acids were found to exhibit high selectivity (~90%) and high activity (~120 µmol butadiene / g cat / min) in the renewable conversion of tetrahydrofuran to butadiene. Although the mechanism of the dehydra-decyclization reaction is not yet well-understood over heteropoly acids, results indicate that entropies and enthalpic energies play a role in stabilizing the transition state of the relevant intermediates, leading to the increase in activity of the tungsten families over molybdenum families and other solid acid catalysts. Preliminary results show there is strong correlation between the activation enthalpy for Brønsted acid catalyzed reactions and density functional theory (DFT)-derived deprotonation energy. To further understand this relationship, in-depth mechanistic experiments in conjunction with theoretical insights are proposed to investigate the kinetically relevant transition states in the THF dehydration reaction and their relation to the deprotonation energies. Key insights obtained on the catalyst design principles for the efficient and sustainable production of renewable C4 – C6 dienes can help work towards a rubber / elastomer industry based on biomass-derived feedstocks.

Bibliography

1. Cron, A. F. Industry and Permanent Subject of Research. 2022, 10–12.
2. Daage, M. Base Oil Production and Processing. Catalytic Science Series, Zeolites for Cleaner Technologies, 2002, 3, 167-187.
3. Zeolite Market Size, Share | Industry Report, 2022-2030 (accessed Mar 11, 2022).
4. Thomas, C. L.; Barmby, D. S. The Chemistry of Catalytic Cracking with Molecular Sieve Catalysts, J. Catal. 1968, 12, 341.
5. Haynes, Jr., H. W.; Parker, J. F.; Helmer, N. E. Hydrocracking Polycyclic Hydrocarbons over a Dual-Functional Zeolite (Faujasite)-Based Catalyst, Ind. Eng. Chem. Process Des. Dev. 1983, 22, 401.
6. Vaughan, D. E.; Ghosh, A.K. Catalytic Reforming Using Group VIII Noble Metal High Silica Faujasites. US Patent 4. 1989, 832, 824.
7. Calemma, V.; Ferrari, M.; Rabl, S.; Weitkamp, J. Selective Ring Opening of Naphthenes: From Mechanistic Studies With a Model Feed to the Upgrading of a Hydrotreated Light Cycle Oil. Fuel 2013, 111, 763.
8. Bulánek, R. Catalysis in Zeolites and Zeotypes—Cornerstone of Chemical Industry and Permanent Subject of Research. Catalysts 2022, 12, 53. https://doi.org/10.3390/ catal12010053
9. Kalvachev, Y.; Todorova, T.; Popov, C. Recent Progress in Synthesis and Application of Nanosized and Hierarchical Mordenite—A Short Review. Catalysts 2021, 11, 308.
10. Parker, S.F.; Kombanal, A.J. How Many Molecules Can Fit in a Zeolite Pore? Implications for the Hydrocarbon Pool Mechanism of the Methanol-to-Hydrocarbons Process. Catalysts 2021, 11, 1204.
11. H. Dai, Y. Shen, T. Yang, C. Lee, D. Fu, A. Agarwal, T.T. Le, M. Tsapatsis, J.C. Palmer, B.M. Weckhuysen, Finned zeolite catalysts, Nature Materials, 19 (2020) 1074-1080.

12. Hunger, M. Brønsted Acid Sites in Zeolites Characterized by Multinuclear Solid State NMR Spectroscopy. Catal. Rev.-Sci. Eng. 1997, 39, 345.
13. Aguayo, A. T.; Gayubo, A. G.; Erena, J.; Olazar, M.; Arandes, J. M.; Bilbao, J. Isotherms of Chemical Adsorption of Bases on Solid Catalysts for Acidity Measurement. J. Chem. Tech. Biotechnol. 1994, 60, 141.
14. Auroux, A.; Bolis, V.; Wierzchowski, P.; Gravelle, P. C.; Vedrine, J. C. Study of the Acidity of ZSM-5 by Microcalorimetry and Infrared Spectroscopy. J. Chem. Soc. Faraday Trans. 1979, 1, 75, 2544.
15. Knözinger, H. Infrared Spectroscopy for the Characterization of Surface Acidity and Basicity. Handbook of Heterogeneous Catalysis, Wiley-VCH, 2008, 2, 1135.
16. Paze, C.; Bordiga, S.; Lamberti, C.; Salvalaggio, M.; Zecchina, A.; Bellussi, G. Acidic Properties of H-β Zeolite As Probed by Bases with Proton Affinity in the 118-204 kcal mol-1 Range: A FTIR Investigation. J. Phys. Chem. B 1997, 101, 4740.
17. Montanari, T.; Bevilacqua, M.; Busca, G.; Use of Nitriles as Probe Molecules for the Accessibility of the Active Sites and the Detection of Complex Interactions in Zeolites Through IR Spectroscopy. Appl. Catal. A: General 2006, 307, 21-29.
18. Pereira, C.; Gorte, R. J. Methods for Distinguishing Brønsted Acid Sites in Mixtures of H-ZSM-5, H-Y and Silica-Alumina. Appl. Catal. A: General 1992, 90, 145.
19. Haag, W. O.; Lago, R. M.; Weisz, P. B. The Active Site of Acidic Aluminosilicate Catalysts. Nature 1984, 390, 589.
20. W. Kiefer and H. J. Bernstein, Appl. Spectrosc., 1971, 25, 609.
21. A. Muller and T. Weber, Appl. Catal., 1991, 77, 243.
22. Y. T. Chua and P. C. Stair, J. Catal., 2000, 196, 66.
23. G. Spoto, E. N. Gribov, G. Ricchiardi, A. Damin, D. Scarano, S. Bordiga, C. Lamberti and A. Zecchina, Prog. Surf. Sci., 2004, 76, 71.

24. E. Stavitski, M. H. F. Kox, I. Swart, F. M. F. de Groot and B. M. Weckhuysen, Angew. Chem.-Int. Edit., 2008, 47, 3543.
25. F. C. Meunier, Chem. Soc. Rev., 2010, 39, 4602.42. P. Bazin, A. Alenda and F. Thibault-Starzyk, Dalton Trans., 2010, 39, 8432.
26. M. El-Roz, P. Bazin and F. Thibault-Starzyk, Catal. Today, 2013, 205, 111.
27. P. Beato, E. Schachtl, K. Barbera, F. Bonino and S. Bordiga, Catal. Today, 2013, 205, 128.
28. A. J. O'Malley, C. R. A. Catlow, M. Monkenbusch, H. Jobic, J. Phys. Chem. C 2015, 119, 26999–27006.
29. A. J. O'Malley, S. F. Parker, C. R. A. Catlow, Chem. Commun. 2017, 53, 12164–12176.
30. S. K. Matam, C. R. A. Catlow, I. P. Silverwood, A. J. O'Malley, Top. Catal. 2021, 64, 699–706.
31. T. W. Hansen, J. B. Wagner, P. L. Hansen, S. Dahl, H. Topsoe and C. J. H. Jacobsen, Science, 2001, 294, 1508.
32. P. L. Gai, Microsc. microanal., 2002, 8, 21. 751. P. L. Hansen, J. B. Wagner, S. Helveg, J. R. Rostrup-Nielsen, B. S. Clausen and H. Topsoe, Science, 2002, 295, 2053.
33. S. Helveg, C. Lopez-Cartes, J. Sehested, P. L. Hansen, B. S. Clausen, J. R. Rostrup-Nielsen, F. Abild- Pedersen and J. K. Norskov, Nature, 2004, 427, 426.
34. Thibault-Starzyk, F.; Stan, I.; Abello, S.; Bonilla, A.; Thomas, K.; Fernandez, C.; Gilson, J.-P.; Perez-Ramirez, J. Quantification of Enhanced Acid Site Accessibility in Hierarchical Zeolites – The Accessibility Index. J. Catal. 2009, 264, 11.
35. Mlekodaj, K.; Tarach, K.; Datka, J.; Gora-Marek, K.; Makowski, W. Porosity and Accessibility of Acid Sites in Desilicated ZSM-5 Zeolites Studied Using Adsorption of Probe Molecules. Microporous and Mesoporous Materials 2014, 183, 54.

36. Corma, A.; Fornes, V.; Forni, L.; Marques, F.; Martinez-Triguero, J.; Moscotti, D. 2,6-Di-Tert-Butyl-Pyridine as a Probe Molecule to Measure External Acidity of Zeolites. J. Catal. 1998, 179, 451.
37. Gora-Marek, K.; Tarach, K.; Choi, M. 2,6-Di-Tert-Butylpyridine Sorption Approach to Quantify the External Acidity in Hierarchical Zeolites. J. Phys. Chem. C 2014, 118, 12266.
38. Wu, Y.; Emdadi, L.; Qin, D.; Zhan, J.; Liu, D. Quantification of External Surface and Pore Mouth Acid Sites in Unit-Cell Thick Pillared MFI and Pillared MWW Zeolites. Microporous and Mesoporous Materials 2017, 241, 43.
39. Lercher, J.A., Gründling, C., Eder-Mirth, G., Catalysis Today 27, 353 (1996).
40. Kunkeler, P. J.; Downing, R. S.; van Bekkum, H. The Use of Bulky Molecules as Probes for Investigating the Contributions of the External and Internal Pore-Wall Activities of Zeolite Catalysts. Stud. Surf. Sci. Catal. 2001, 137, 987.
41. D. Fu, J. J. E. Maris, K. Stanciakova, N. Nikolopoulos, O. Heijden, L. D. B. Mandemaker, M. E. Siemons, D. S. Pastene, L. C. Kapitein, F. T. Rabouw, F. Meirer, and B. M. Weckhuysen, Angew. Chem. Int. Ed. 2022, 61, e202114388
42. Davis, Mark E. and Davis, Robert J. (2003) *Fundamentals of Chemical Reaction Engineering.* McGraw-Hill Higher Education, New York, NY. ISBN 0-07-245007-X
43. Frédéric Thibault-Starzyk, Irina Stan, Sònia Abelló, Adriana Bonilla, Karine Thomas, Christian Fernandez, Jean-Pierre Gilson, Javier Pérez-Ramírez,
44. Quantification of enhanced acid site accessibility in hierarchical zeolites – The accessibility index, Journal of Catalysis, Volume 264, Issue 1, 2009, Pages 11-14, ISSN 0021-9517.
45. Chem. Soc. Rev., 2015,44, 7262-7341
46. R. Buzzoni, S. Bordiga, G. Ricchiardi, C. Lamberti, A. Zecchina and G. Bellussi, Langmuir, 1996, 12, 930

Chapter 3 References

47. [1] E. M. Gallego et al., "Ab initio" synthesis of zeolites for preestablished catalytic reactions. Science 355, 1051-1054 (2017).

48. [2] C. Paolucci et al., Dynamic multinuclear sites formed by mobilized copper ions in NOx selective catalytic reduction. Science 357, 898-903 (2017).
49. [3] K. A. Cychosz, R. Guillet-Nicolas, J. Garcia-Martinez, M. Thommes, Recent advances in the textural characterization of hierarchically structured nanoporous materials. Chem. Soc. Rev. 46, 389-414 (2017).
50. [4] K. Varoon et al., Dispersible exfoliated zeolite nanosheets and their application as a selective membrane. Science 333, 72-75 (2011).
51. [5] N. Rangnekar, N. Mittal, B. Elyassi, J. Caro, M. Tsapatsis, Zeolite membranes - a review and comparison with MOFs. Chem. Soc. Rev. 44, 7128-7154 (2015).
52. [6] L. Karwacki et al., Morphology-dependent zeolite intergrowth structures leading to distinct internal and outer-surface molecular diffusion barriers. Nat. Mater. 8, 959-965 (2009).
53. [7] A. Hwang et al., Effects of diffusional constraints on lifetime and selectivity in methanol-to-olefins catalysis on HSAPO-34. J. Catal. 369, 122-132 (2019).
54. [8] H. Awala et al., Template-free nanosized faujasite-type zeolites. Nat. Mater. 14, 447-451 (2015).
55. [9] M. Choi et al., Stable single-unit-cell nanosheets of zeolite MFI as active and long-lived catalysts. Nature 461, 246-249 (2009).
56. [10] K. Na et al., Directing zeolite structures into hierarchically nanoporous architectures. Science 333, 328-332 (2011).
57. [11] X. Y. Zhang et al., Synthesis of self-pillared zeolite nanosheets by repetitive branching. Science 336, 1684-1687 (2012).
58. [12] K. H. Li, J. Valla, J. Garcia-Martinez, Realizing the commercial potential of hierarchical zeolites: new opportunities in catalytic cracking. ChemCatChem 6, 46-66 (2014).
59. [13] J. Perez-Ramirez, C. H. Christensen, K. Egeblad, C. H. Christensen, J. C. Groen, Hierarchical zeolites: enhanced utilisation of microporous crystals in catalysis by advances in materials design. Chem. Soc. Rev. 37, 2530-2542 (2008).

60. [14] Y. Shen et al., Deconvoluting the competing effects of framework topology and diffusion path length on methanol-to-hydrocarbons reactions. ACS Catal. 8, 11042-11053 (2018).
61. [15] Z. Ristanovic et al., Intergrowth structure and aluminium zoning of a zeolite ZSM-5 crystal as resolved by synchrotron-based micro X-Ray diffraction imaging. Angew. Chem.-Int. Edit. 52, 13382-13386 (2013).
62. [16] K. L. Ding et al., Constructing hierarchical porous zeolites via kinetic regulation. J. Am. Chem. Soc. 137, 11238-11241 (2015).
63. [17] J. J. De Yoreo et al., Crystallization by particle attachment in synthetic, biogenic, and geologic environments. Science 349, aaa6760 (2015).
64. [18] A. I. Lupulescu, J. D. Rimer, In situ imaging of silicalite-1 surface growth reveals the mechanism of crystallization. Science 344, 729-732 (2014).
65. [19] H. Zhu, Z. Liu, D. Kong, Y. Wang, Z. Xie, Synthesis and catalytic performances of mesoporous zeolites templated by polyvinyl butyral gel as the mesopore directing agent. J. Phys. Chem. C 112, 17257-17264 (2008).
66. [20] H. Zhang et al., Seeding bundlelike MFI zeolite mesocrystals: A dynamic, nonclassical crystallization via epitaxially anisotropic growth. Chem. Mater. 29, 9247-9255 (2017).
67. [21] S. Kim, G. Park, M. H. Woo, G. Kwak, S. K. Kim, Control of hierarchical structure and framework-Al distribution of ZSM-5 via adjusting crystallization temperature and their effects on methanol conversion. ACS Catal. 9, 2880-2892 (2019).
68. [22] A. Ghorbanpour, A. Gumidyala, L. C. Grabow, S. P. Crossley, J. D. Rimer, Epitaxial growth of ZSM-5@silicalite-1: A core-shell zeolite designed with passivated surface acidity. ACS Nano 9, 4006-4016 (2015).
69. [23] S. Ilias, A. Bhan, Mechanism of the catalytic conversion of methanol to hydrocarbons. ACS Catal. 3, 18-31 (2013).
70. [24] R. Khare, D. Millar, A. Bhan, A mechanistic basis for the effects of crystallite size on light olefin selectivity in methanol-to-hydrocarbons conversion on MFI. J. Catal. 321, 23-31 (2015).

71. [25] E. C. Nordvang, E. Borodina, J. Ruiz-Martinez, R. Fehrmann, B. M. Weckhuysen, Effects of coke deposits on the catalytic performance of large zeolite H-ZSM-5 crystals during alcohol-to-hydrocarbon reactions as investigated by a combination of optical spectroscopy and microscopy. Chem.: Eur. J. 21, 17324-17335 (2015).
72. [26] P. D. Kolokathis et al., Dimensionality reduction of free energy profiles of benzene in silicalite-1: calculation of diffusion coefficients using transition state theory. Mol. Simul. 40, 80-100 (2014).
73. [27] D. M. Ruthven, M. Eic, E. Richard, Diffusion of C8 aromatic hydrocarbons in silicalite. Zeolites 11, 647-653 (1991).
74. [28] Góra-Marek, Kinga, Karolina Tarach, and Minkee Choi, 2,6-Di-tert-butylpyridine sorption approach to quantify the external acidity in hierarchical zeolites. J. Phys. Chem. C 118, 12266-12274 (2014).

Chapter 4 References

75. [1] K. Varoon, X. Zhang, B. Elyassi, D. D. Brewer, M. Gettel, S. Kumar, J. A. Lee, S. Maheshwari, A. Mittal, C. Y. Sung et al. Science 2011, 334, 6052, 72-75
76. [2] K. A. Cychosz, R. Guillet-Nicolas, J. García-Martínez, M. Thommes, Chem. Soc. Rev. 2017, 46, 2, 389–414
77. [3] J. Li, A. Corma, J. Yu, Chem. Soc. Rev. 2015, 44, 20, 7112–7127; d) D. J. Rimer, J. D. Nat. Catal. 2018, 1, 7, 488–489
78. [4] E. M. Gallego, M. T. Portilla, C. Paris, A. León-Escamilla, M. Boronat, M. Moliner, A. Corma, Science 2017, 355, 6329, 1051–1054
79. [5] N. Rangnekar, N. Mittal, B. Elyassi, J. Caro, M. Tsapatsis, Chem. Soc. Rev. 2015, 44, 20, 7128–7154
80. [6] C. Martínez, A. Corma, Coord. Chem. Rev. 2011, 255, 13, 1558–1580; h) M. E. Davis, Nature. 2002, 813–821
81. [7] I. Yarulina, A. D. Chowdhury, F. Meirer, B. M. Weckhuysen, J. Gascon, Nat. Catal. 2018, 1, 6, 398–411.

82. [8] M. Choi, K. Na, J. Kim, Y. Sakamoto, O. Terasaki, R. Ryoo, Nature 2009, 461, 7261, 246–249
83. [9] J. Přech, P. Pizarro, D. P. Serrano, J. Áejka, Chem. Soc. Rev. 2018, 8263–8306
84. [10] M. T. Yuan, D. Y. Zhao, Q. Q. Hao, Q. X. Luo, J. Zhang, H. Chen, M. Sun, L. Xu, X. Ma, Ind. Eng. Chem. Res. 2020, 59, 37, 16312–16320
85. [11] L. Xu, P. Wu, New J. Chem. 2016, 40, 5, 3968–3981
86. [12] W. J. Roth, P. Nachtigall, R. E. Morris, J. Čejka, Chem. Rev. 2014, 114, 9, 4807–4837
87. [13] Y. Zhou, Y. Mu, M. F. Hsieh, B. Kabius, C. Pacheco, C. Bator, R. M. Rioux, J. D. Rimer, J. Am. Chem. Soc. 2020, 142, 18, 8211–8222.
88. [14] X. Zhang, D. Liu, D. Xu, S. Asahina, K. A. Cychosz, K. V. Agrawal, Y. Al Wahedi, A. Bhan, S. Al Hashimi, O. Terasaki et al. Science 2012, 336, 6089, 1684–1687
89. [15] P. Lu, S. Ghosh, M. Dorneles de Mello, H. S. Kamaluddin, X. Li, G. Kumar, X. Duan, M. Abeykoon, J. A. Boscoboinik, L. Qi et al. Angew. Chemie Int. Ed. 2021, 60, 35, 19214-19221
90. [16] L. Ren, Q. Guo, P. Kumar, M. Orazov, D. Xu, S. M. Alhassan, K. A. Mkhoyan, M. E. Davis, M. Tsapatsis, Angew. Chemie Int. Ed. 2015, 54, 37, 10848–10851.
91. [17] K. Li, J. Valla, J. Garcia-Martinez, ChemCatChem 2014, 6 (1), 46–66
92. [18] K. Zhang, M. L. Ostraat, Catal. Today 2016, 264, 3–15
93. [19] J. Pérez-Ramírez, C. H. Christensen, K. Egeblad, C. H. Christensen, J. C. Groen, Chem. Soc. Rev. 2008, 37 (11), 2530–2542
94. [20] E. Koohsaryan, M. Anbia, Chinese J. Catal. 2016, 37 (4), 447–467
95. [21] W. Schwieger, A. G. Machoke, T. Weissenberger, A. Inayat, T. Selvam, M. Klumpp, A. Inayat, Chem. Soc. Rev. 2016, 45 (12), 3353–3376.
96. [22] V. Valtchev, L. Tosheva, Chem. Rev. 2013, 113 (8), 6734–6760

97. [23] S. Mintova, M. Jaber, V. Valtchev, Chem. Soc. Rev. 2015, 44 (20), 7207–7233
98. [24] S. Mintova, J. P. Gilson, V. Valtchev, Nanoscale 2013, 5 (15), 6693–6703
99. [25] H. Awala, J. P. Gilson, R. Retoux, P. Boullay, J. M. Goupil, V. Valtchev, S. Mintova, Nat. Mater. 2015, 14 (4), 447–451
100. [26] I. Schmidt, C. Madsen, C. J. H. Jacobsen, Inorg. Chem. 2000, 39 (11), 2279–2283.
101. [27] O. Muraza, Ind. Eng. Chem. Res. 2015, 54 (3), 781–789
102. [28] O. Muraza, I. A. Bakare, T. Tago, H. Konno, T. Taniguchi, A. M. Al-Amer, Z. H. Yamani, Y. Nakasaka, T. Masuda, Fuel 2014, 135, 105–111
103. [29] M. H. M. Ahmed, O. Muraza, A. M. Al-Amer, K. Miyake, N. Nishiyama, Appl. Catal. A Gen. 2015, 497, 127–134.
104. [30] S. S. Hassani, F. Salehirad, H. R. Aghabozorg, Z. Sobat, Cryst. Res. Technol. 2010, 45 (2), 183–187
105. [31] R. Li, N. Linares, J. G. Sutjianto, A. Chawla, J. Garcia-Martinez, J. D. Rimer, Angew. Chemie Int. Ed. 2018, 57 (35), 11283–11288
106. [32] M. Kumar, Z. J. Berkson, R. J. Clark, Y. Shen, N. A. Prisco, Q. Zheng, Z. Zeng, H. Zheng, L. B. McCusker, J. C. Palmer et al. J. Am. Chem. Soc. 2019, 141 (51), 20155–20165.
107. [33] W. J. Roth, C. T. Kresge, J. C. Vartuli, M. E. Leonowicz, A. S. Fung, S. B. McCullen, Elsevier, 1995, 94, 301–308
108. [34] A. Corma, C. Corell, J. Pérez-Pariente, Zeolites 1995, 15 (1), 2–8
109. [35] L. Schreyeck, P. Caullet, J. C. Mougenel, J. L. Guth, B. Marler, Microporous Mater. 1996, 6 (5), 259–271.
110. [36] P. Kumar, K. V. Agrawal, M. Tsapatsis, K. A. Mkhoyan, Nat. Commun. 2015, 6 (1), 7128
111. [37] P. Wuamprakhon, C. Wattanakit, C. Warakulwit, T. Yutthalekha, W. Wannapakdee, S. Ittisanronnachai, J. Limtrakul, Microporous Mesoporous Mater. 2016, 219, 1–9

112. [38] M. V. Opanasenko, W. J. Roth, J. Čejka, Catal. Sci. Technol. 2016, 6 (8), 2467–2484.

113. [39] H. Xu, W. Chen, G. Zhang, P. Wei, Q. Wu, L. Zhu, X. Meng, X. Li, J. Fei, S. Han et al. J. Mater. Chem. A 2019, 7 (28), 16671–16676

114. [40] W. Chu, X. Li, X. Zhu, S. Xie, C. Guo, S. Liu, F. Chen, L. Xu, Microporous Mesoporous Mater. 2017, 240, 189–196

115. [41] W. Chu, F. Chen, C. Guo, X. Li, X. Zhu, Y. Gao, S. Xie, S. Liu, N. Jiang, L. Xu, Chinese J. Catal. 2017, 38 (11), 1880–1887

116. [42] Y. Lee, M. B. Park, P. S. Kim, A. Vicente, C. Fernandez, I. S. Nam, S. B. Hong, ACS Catal. 2013, 3 (4), 617–621

117. [43] W. Dai, V. Ruaux, X. Deng, W. Tai, G. Wu, N. Guan, L. Li, V. Valtchev, J. Mater. Chem. A 2021; DOI: 10.1039/D1TA06596C

118. [44] Y. P. Khitev, I. I. Ivanova, Y. G. Kolyagin, O. A. Ponomareva, Appl. Catal. A: Gen. 2012, 441, 124-135.

119. [45] C. L. Kibby, A. J. Perrotta, F. E. Massoth, J. Catal. 1974, 35 (2), 256–272

120. [46] J. Liu, H. Xue, X. Huang, Y. Li, W. Shen, Catal. Letters 2010, 139 (1), 33–37

121. [47] V. J. Margarit, M. R. Díaz-Rey, M.T. Navarro, C. Martínez, A. Corma, Angew. Chemie Int. Ed. 2018, 57 (13), 3459–3463

122. [48] H. Xu, J. Zhu, L. Zhu, E. Zhou, C. Shen, Molecules 2020, 25 (16), 3722

123. [49] Z. Zhao, W. Zhang, P. Ren, X. Han, U. Müller, B. Yilmaz, M. Feyen, H. Gies, F. Xiao, D. D. Vos, T. Tatsumi, X. Bao, Chem. Mater. 2013, 25 (6), 840-847.

124. [50] L. Qi, J. Li, L. Xu, Z. Liu, RSC Adv. 2016, 6 (61), 56698–56704.

125. [51] A. Corma, U. Diaz, M. E. Domine, V. Fornés, Angew. Chemie Int. Ed. 2000, 39 (8), 1499–1501.

126. [52] A. Bonilla, D. Baudouin, J. Pérez-Ramírez, J. Catal. 2009, 265 (2), 170–180

127. [53] E. Catizzone, M. Migliori, A. Aloise, R. Lamberti, G. Giordano, J. Chem. 2019, 2019, 3084356.

128. [54] H. Dai, Y. Shen, T. Yang, C. Lee, D. Fu, A. Agarwal, T. T. Le, M. Tsapatsis, J. C. Palmer, B. M. Weckhuysen et al. Nat. Mater. 2020, 19 (10), 1074–1080

129. [55] B. Xie, J. Song, L. Ren, Y. Ji, J. Li, F. Xiao, Chem. Mater. 2008, 20 (14), 4533-4535; c) H. Zhang, L. Wang, D. Zhang, X. Meng, F. Xiao, Microporous Mesoporous Mater. 2016, 233, 133-139.

130. [56] N. Danilina, F. Krumeich, S. A. Castelanelli, J. A. Van Bokhoven, J. Phys. Chem. C 2010, 114 (14), 6640–6645

131. [57] W. Qin, Y. Zhou, J. D. Rimer, React. Chem. Eng. 2019, 4 (11), 1957–1968

132. [58] J. Dwyer, F. R. Fitch, G. Qin, J. C. Vickerman, J. Phys. Chem. 1982, 86 (23), 4574–4578.

133. [59] P. A. Vaughan, Acta Crystallogr. 1966, 21 (6), 983–990.

134. [60] Y. Shen, T. T. Le, D. Fu, J. E. Schmidt, M. Filez, B. M. Weckhuysen, J. D. Rimer, ACS Catal. 2018, 8 (12), 11042–11053.

135. [61] S. Bordiga, C. Lamberti, F. Bonino, A. Travert, F. Thibault-Starzyk, Chem. Soc. Rev. 2015, 44 (20), 7262–7341.

136. [62] A. A. Gabrienko, I. G. Danilova, S. S. Arzumanov, L. V. Pirutko, D. Freude, A. G. Stepanov, J. Phys. Chem. C 2018, 122 (44), 25386–25395

137. [63] C. Schroeder, V. Siozios, M. Hunger, M. R. Hansen, H. Koller, J. Phys. Chem. C 2020, 124 (42), 23380-23386

138. [64] S. Zeng, J. Li, N. Wang, W. Zhang, Y. Wei, Z. Liu, S. Xu, Energy Fuels 2021.

139. [65] M. Ravi, V. L. Sushkevich, J. A. van Bokhoven, Nat. Mater. 2020, 19 (10), 1047–1056.

140. [66] D. Jo, S. B. Hong, M. A. Camblor, ACS Catal. 2015, 5 (4), 2270–2274.

Chapter 5 References

141. [1] K. Na, M. Choi, W. Park, Y. Sakamoto, O. Terasaki, R. Ryoo, Pillared MFI zeolite nanosheets of a single-unit-cell thickness, Journal of the American Chemical Society, 132 (2010) 4169-4177.

142. [2] K. Na, G.A. Somorjai, Hierarchically nanoporous zeolites and their heterogeneous catalysis: current status and future perspectives, Catalysis Letters, 145 (2015) 193-213.

143. [3] T.T. Le, A. Chawla, J.D. Rimer, Impact of acid site speciation and spatial gradients on zeolite catalysis, Journal of Catalysis, 391 (2020) 56-68.

144. [4] B.C. Knott, C.T. Nimlos, D.J. Robichaud, M.R. Nimlos, S. Kim, R. Gounder, Consideration of the aluminum distribution in zeolites in theoretical and experimental catalysis research, ACS Catalysis, 8 (2018) 770-784.

145. [5] M. Ravi, V.L. Sushkevich, J.A. van Bokhoven, Towards a better understanding of Lewis acidic aluminium in zeolites, Nature Materials, 19 (2020) 1047-1056.

146. [6] L. Karwacki, M.H. Kox, D.M. De Winter, M.R. Drury, J.D. Meeldijk, E. Stavitski, W. Schmidt, M. Mertens, P. Cubillas, N. John, A.S. Chan, N. Kahn, S.R. Bare, M.W. Anderson, J. Kornatowski, B.M. Weckhuysen, Morphology-dependent zeolite intergrowth structures leading to distinct internal and outer-surface molecular diffusion barriers, Nature Materials, 8 (2009) 959-965.

147. [7] R. Von Ballmoos, W. Meier, Zoned aluminium distribution in synthetic zeolite ZSM-5, Nature, 289 (1981) 782-783.

148. [8] D.J. Yang, Process for coating crystalline silica polymorphs, EI Du Pont de Nemours and Co, 1982, Patent US4452909A.

149. [9] P.G. Rodewald, Silica-modified zeolite catalysts, Mobil Oil Corporation, New York. N.Y., 1981, Patent US4402867A.

150. [10] J.H. Kim, A. Ishida, M. Okajima, M. Niwa, Modification of HZSM-5 by CVD of various silicon compounds and generation of para-selectivity, Journal of Catalysis, 161 (1996) 387-392.

151. [11] S. Zheng, H.R. Heydenrych, A. Jentys, J.A. Lercher, Influence of surface modification on the acid site distribution of HZSM-5, Journal of Physical Chemistry B, 106 (2002) 9552-9558.
152. [12] P.G. Rodewald, Silica-modified zeolite catalysts, Mobil Oil Corporation, New York. N.Y., 1977, Patent US4145315A.
153. [13] R. Brent, S.M. Stevens, O. Terasaki, M.W. Anderson, Coaxial core shell overgrowth of zeolite L - Dependence on original crystal growth mechanism, Crystal Growth & Design, 10 (2010) 5182-5186.
154. [14] W. Huybrechts, J.W. Thybaut, B.R. De Waele, G. Vanbutsele, K.J. Houthoofd, F. Bertinchamps, J.F.M. Denayer, E.M. Gaigneaux, G.B. Marin, G.V. Baron, P.A. Jacobs, J.A. Martens, Bifunctional catalytic isomerization of decane over MTT-type aluminosilicate zeolite crystals with siliceous rim, Journal of Catalysis, 239 (2006) 451-459.
155. [15] M. Okamoto, L. Huang, M. Yamano, S. Sawayama, Y. Nishimura, Skeletal isomerization of tetradecane catalyzed by TON-type zeolites with a fragmented core-shell structure, Applied Catalysis, A, 455 (2013) 122-128.
156. [16] C. Peng, Z. Liu, Y. Yonezawa, Y. Yanaba, N. Katada, I. Murayama, S. Segoshi, T. Okubo, T. Wakihara, Ultrafast Post-Synthesis Treatment to Prepare ZSM-5@Silicalite-1 as a Core-Shell Structured Zeolite Catalyst, Microporous and Mesoporous Materials, 277 (2019) 197-202.
157. [17] X. Zhang, D. Liu, D. Xu, S. Asahina, K.A. Cychosz, K.V. Agrawal, Y. Al Wahedi, A. Bhan, S. Al Hashimi, O. Terasaki, Synthesis of self-pillared zeolite nanosheets by repetitive branching, Science, 336 (2012) 1684-1687.
158. [18] W. Chaikittisilp, Y. Suzuki, R.R. Mukti, T. Suzuki, K. Sugita, K. Itabashi, A. Shimojima, T. Okubo, Formation of hierarchically organized zeolites by sequential intergrowth, Angewandte Chemie International Edition, 125 (2013) 3439-3443.
159. [19] R. Jain, A. Chawla, N. Linares, J. García Martínez, J.D. Rimer, Spontaneous Pillaring of Pentasil Zeolites, Advanced Materials, 33 (2021) 2100897.

160. [20] K. Li, J. Valla, J. Garcia-Martinez, Realizing the Commercial Potential of Hierarchical Zeolites: New Opportunities in Catalytic Cracking, ChemCatChem, 6 (2014) 46-66.
161. [21] H. Dai, Y. Shen, T. Yang, C. Lee, D. Fu, A. Agarwal, T.T. Le, M. Tsapatsis, J.C. Palmer, B.M. Weckhuysen, Finned zeolite catalysts, Nature Materials, 19 (2020) 1074-1080.
162. [22] H. Awala, J.-P. Gilson, R. Retoux, P. Boullay, J.-M. Goupil, V. Valtchev, S. Mintova, Template-free nanosized faujasite-type zeolites, Nature Materials, 14 (2015) 447-451.
163. [23] B.C. Gates, M. Flytzani-Stephanopoulos, D.A. Dixon, A. Katz, Atomically dispersed supported metal catalysts: perspectives and suggestions for future research, Catalysis Science & Technology, 7 (2017) 4259-4275.
164. [24] S.T. Hunt, M. Milina, A.C. Alba-Rubio, C.H. Hendon, J.A. Dumesic, Y. Román-Leshkov, Self-assembly of noble metal monolayers on transition metal carbide nanoparticle catalysts, Science, 352 (2016) 974-978.
165. [25] Y. Shen, Z. Qin, S. Asahina, N. Asano, G. Zhang, S. Qian, Y. Ma, Z. Yan, X. Liu, S. Mintova, The inner heterogeneity of ZSM-5 zeolite crystals, Journal of Materials Chemistry A, 9 (2021) 4203-4212.
166. [26] X. Wang, G. Yang, J. Zhang, S. Chen, Y. Wu, Q. Zhang, J. Wang, Y. Han, Y. Tan, Synthesis of isoalkanes over a core (Fe–Zn–Zr)–shell (zeolite) catalyst by CO_2 hydrogenation, Chemical Communications, 52 (2016) 7352-7355.
167. [27] R. Zhang, J. Wang, L. Han, J. Wang, L. Zhao, Enhanced aromatic selectivity using the core–shell synergistic effects of HZSM-5/SAPO-5 zeolites in isobutane conversion, Journal of Physics and Chemistry of Solids, (2021) 110194.
168. [28] Q. Zhao, B. Qin, J. Zheng, Y. Du, W. Sun, F. Ling, X. Zhang, R. Li, Core–shell structured zeolite–zeolite composites comprising Y zeolite cores and nano-β zeolite shells: Synthesis and application in hydrocracking of VGO oil, Chemical Engineering Journal, 257 (2014) 262-272.

169. [29] J.H. Ahn, R. Kolvenbach, S.S. Al-Khattaf, A. Jentys, J.A. Lercher, Enhancing shape selectivity without loss of activity - novel mesostructured ZSM5 catalysts for methylation of toluene to p-xylene, Chemical Communications, 49 (2013) 10584-10586.
170. [30] T. Hibino, M. Niwa, Y. Murakami, Shape-selectivity over hzsm-5 modified by chemical vapor deposition of silicon alkoxide, Journal of Catalysis, 128 (1991) 551-558.
171. [31] S. Zheng, H.R. Heydenrych, H.P. Roger, A. Jentys, J.A. Lercher, On the Enhanced Selectivity of HZSM-5 Modified by Chemical Liquid Deposition, Topics in Catalysis, 22 (2003) 101.
172. [32] F. Goodarzi, I.P. Herrero, G.N. Kalantzopoulos, S. Svelle, A. Lazzarini, P. Beato, U. Olsbye, S. Kegnæs, Synthesis of Mesoporous ZSM-5 Zeolite Encapsulated in an Ultrathin Protective Shell of Silicalite-1 for MTH Conversion, Microporous and Mesoporous Materials, 292 (2020) 109730-109730.
173. [33] U. Olsbye, S. Svelle, M. Bjørgen, P. Beato, T.V.W. Janssens, F. Joensen, S. Bordiga, K.P. Lillerud, Conversion of Methanol to Hydrocarbons: How Zeolite Cavity and Pore Size Controls Product Selectivity, Angewandte Chemie International Edition, 51 (2012) 5810-5831.
174. [34] A. Galadima, O. Muraza, From synthesis gas production to methanol synthesis and potential upgrade to gasoline range hydrocarbons: A review, Journal of Natural Gas Science and Engineering, 25 (2015) 303-316.
175. [35] I. Yarulina, A.D. Chowdhury, F. Meirer, B.M. Weckhuysen, J. Gascon, Recent Trends and Fundamental Insights in the Methanol-to-Hydrocarbons Process, Nature Catalysis, 1 (2018) 398-411.
176. [36] A.D. Chowdhury, K. Houben, G.T. Whiting, M. Mokhtar, A.M. Asiri, S.A. Al-Thabaiti, S.N. Basahel, M. Baldus, B.M. Weckhuysen, Initial Carbon-Carbon Bond Formation during the Early Stages of the Methanol-to-Olefin Process Proven by Zeolite-Trapped Acetate and Methyl Acetate, Angewandte Chemie International Edition, 55 (2016) 15840-15845.

177. [37] Y. Liu, S. Müller, D. Berger, J. Jelic, K. Reuter, M. Tonigold, M. Sanchez-Sanchez, J.A. Lercher, Formation Mechanism of the First Carbon–Carbon Bond and the First Olefin in the Methanol Conversion into Hydrocarbons, Angewandte Chemie International Edition, 55 (2016) 5723-5726.
178. [38] A.D. Chowdhury, A.L. Paioni, K. Houben, G.T. Whiting, M. Baldus, B.M. Weckhuysen, Bridging the Gap between the Direct and Hydrocarbon Pool Mechanisms of the Methanol-to-Hydrocarbons Process, Angewandte Chemie International Edition, 57 (2018) 8095-8099.
179. [39] S. Ilias, A. Bhan, Mechanism of the Catalytic Conversion of Methanol to Hydrocarbons, ACS Catalysis, 3 (2013) 18-31.
180. [40] S. Ilias, R. Khare, A. Malek, A. Bhan, A descriptor for the relative propagation of the aromatic- and olefin-based cycles in methanol-to-hydrocarbons conversion on H-ZSM-5, Journal of Catalysis, 303 (2013) 135-140.
181. [41] S.S. Arora, A. Bhan, The critical role of methanol pressure in controlling its transfer dehydrogenation and the corresponding effect on propylene-to-ethylene ratio during methanol-to-hydrocarbons catalysis on H-ZSM-5, Journal of Catalysis, 356 (2017) 300-306.
182. [42] Y. Liu, F.M. Kirchberger, S. Müller, M. Eder, M. Tonigold, M. Sanchez-Sanchez, J.A. Lercher, Critical role of formaldehyde during methanol conversion to hydrocarbons, Nature Communications, 10 (2019) 1462.
183. [43] B.L. Foley, B.A. Johnson, A. Bhan, A Method for Assessing Catalyst Deactivation: A Case Study on Methanol-to-Hydrocarbons Conversion, ACS Catalysis, 9 (2019) 7065-7072.
184. [44] M. Guisnet, L. Costa, F.R. Ribeiro, Prevention of zeolite deactivation by coking, Journal of Molecular Catalysis A: Chemical, 305 (2009) 69-83.
185. [45] A. Ghorbanpour, A. Gumidyala, L.C. Grabow, S.P. Crossley, J.D. Rimer, Epitaxial growth of ZSM-5@Silicalite-1: A core–shell zeolite designed with passivated surface acidity, ACS Nano, 9 (2015) 4006-4016.

186. [46] Y. Shen, T.T. Le, R. Li, J.D. Rimer, Optimized Synthesis of ZSM-11 Catalysts using 1,8-Diaminooctane as a Structure-Directing Agent, ChemPhysChem, 19 (2018) 529-537.
187. [47] Y. Shen, T.T. Le, D. Fu, J.E. Schmidt, M. Filez, B.M. Weckhuysen, J.D. Rimer, Deconvoluting the competing effects of zeolite framework topology and diffusion path length on methanol to hydrocarbons reaction, ACS Catalysis, 8 (2018) 11042-11053.
188. [48] F. Bleken, W. Skistad, K. Barbera, M. Kustova, S. Bordiga, P. Beato, K.P. Lillerud, S. Svelle, U. Olsbye, Conversion of methanol over 10-ring zeolites with differing volumes at channel intersections: comparison of TNU-9, IM-5, ZSM-11 and ZSM-5, Physical Chemistry Chemical Physics, 13 (2011) 2539-2549.
189. [49] P. de Moor, T.P.M. Beelen, B.U. Komanschek, R.A. van Santen, Nanometer scale precursors in the crystallization of Si-TPA-MFI, Microporous and Mesoporous Materials, 21 (1998) 263-269.
190. [50] Y.-Q. Deng, S.-F. Yin, C.-T. Au, Preparation of nanosized Silicalite-1 and its application in vapor-phase Beckmann rearrangement of cyclohexanone oxime, Industrial & Engineering Chemistry Research, 51 (2012) 9492-9499.
191. [51] R. Khare, D. Millar, A. Bhan, A mechanistic basis for the effects of crystallite size on light olefin selectivity in methanol-to-hydrocarbons conversion on MFI, Journal of Catalysis, 321 (2015) 23-31.
192. [52] S.R. Bare, A. Knop-Gericke, D. Teschner, M. Hävacker, R. Blume, T. Rocha, R. Schlögl, A.S. Chan, N. Blackwell, M. Charochak, Surface analysis of zeolites: An XPS, variable kinetic energy XPS, and low energy ion scattering study, Surface Science, 648 (2016) 376-382.
193. [53] W. Qin, Y. Zhou, J.D. Rimer, Deleterious effects of non-framework Al species on the catalytic performance of ZSM-5 crystals synthesized at low temperature, Reaction Chemistry & Engineering, 4 (2019) 1957-1968.

194. [54] G. Paul, C. Bisio, I. Braschi, M. Cossi, G. Gatti, E. Gianotti, L. Marchese, Combined solid-state NMR, FT-IR and computational studies on layered and porous materials, Chemical Society Reviews, 47 (2018) 5684-5739.

195. [55] K. Barbera, F. Bonino, S. Bordiga, T.V.W. Janssens, P. Beato, Structure–deactivation relationship for ZSM-5 catalysts governed by framework defects, Journal of Catalysis, 280 (2011) 196-205.

196. [56] Z. Qin, L. Lakiss, L. Tosheva, J.-P. Gilson, A. Vicente, C. Fernandez, V. Valtchev, Comparative study of nano-ZSM-5 catalysts synthesized in OH^- and F^- media, Advanced Functional Materials, 24 (2014) 257-264.

197. [57] T.V.W. Janssens, A new approach to the modeling of deactivation in the conversion of methanol on zeolite catalysts, Journal of Catalysis, 264 (2009) 130-137.

198. [58] J.S. Martinez-Espin, M. Morten, T.V.W. Janssens, S. Svelle, P. Beato, U. Olsbye, New insights into catalyst deactivation and product distribution of zeolites in the methanol-to-hydrocarbons (MTH) reaction with methanol and dimethyl ether feeds, Catalysis Science & Technology, (2017).

199. [59] R. Khare, Z.H. Liu, Y. Han, A. Bhan, A mechanistic basis for the effect of aluminum content on ethene selectivity in methanol-to-hydrocarbons conversion on HZSM-5, Journal of Catalysis, 348 (2017) 300-305.

200. [60] A. Hwang, T.T. Le, Z. Shi, H. Dai, J.D. Rimer, A. Bhan, Effects of diffusional constraints on lifetime and selectivity in methanol-to-olefins catalysis on HSAPO-34, Journal of Catalysis, 369 (2018) 122-132.

201. [61] I. Yarulina, K. De Wispelaere, S. Bailleul, J. Goetze, M. Radersma, E. Abou-Hamad, I. Vollmer, M. Goesten, B. Mezari, E.J.M. Hensen, J.S. Martínez-Espín, M. Morten, S. Mitchell, J. Perez-Ramirez, U. Olsbye, B.M. Weckhuysen, V. Van Speybroeck, F. Kapteijn, J. Gascon, Structure–performance descriptors and the role of Lewis acidity in the methanol-to-propylene process, Nature Chemistry, 10 (2018) 804-812.

202. [62] F.Y. Dai, M. Suzuki, H. Takahashi, I. Saito, Mechanism of zeolite crystallization without using template reagents of organic bases, in: Y.

Murakami, A. Iijima, J.W. Ward (Eds.) Studies in Surface Science and Catalysis, Elsevier, 1986, pp. 223-230.

203. [63] R. Khare, A. Bhan, Mechanistic studies of methanol-to-hydrocarbons conversion on diffusion-free MFI samples, Journal of Catalysis, 329 (2015) 218-228.

204. [64] P. de Moor, T.P.M. Beelen, B.U. Komanschek, L.W. Beck, P. Wagner, M.E. Davis, R.A. van Santen, Imaging the assembly process of the organic-mediated synthesis of a zeolite, Chemistry: A European Journal, 5 (1999) 2083-2088.

205. [65] A. Leo, The octanol–water partition coefficient of aromatic solutes: the effect of electronic interactions, alkyl chains, hydrogen bonds, and ortho-substitution, Journal of the Chemical Society, Perkin Transactions 2, (1983) 825-838.

206. [66] C.H. Botchway, R. Tia, E. Adei, A.J. O'Malley, N.Y. Dzade, C. Hernandez-Tamargo, N.H. de Leeuw, Influence of topology and Brønsted acid site presence on methanol diffusion in zeolites beta and MFI, Catalysts, 10 (2020) 1342.

207. [67] P. Cnudde, E.A. Redekop, W. Dai, N.G. Porcaro, M. Waroquier, S. Bordiga, M. Hunger, L. Li, U. Olsbye, V. Van Speybroeck, Experimental and Theoretical Evidence for the Promotional Effect of Acid Sites on the Diffusion of Alkenes through Small-Pore Zeolites, Angewandte Chemie International Edition, 133 (2021) 10104-10110.

208. [68] P. Cnudde, R. Demuynck, S. Vandenbrande, M. Waroquier, G. Sastre, V.V. Speybroeck, Light Olefin Diffusion during the MTO Process on H-SAPO-34: A Complex Interplay of Molecular Factors, Journal of the American Chemical Society, 142 (2020) 6007-6017.

209. [69] M. Choi, K. Na, J. Kim, Y. Sakamoto, O. Terasaki, R. Ryoo, Stable single-unit-cell nanosheets of zeolite MFI as active and long-lived catalysts, Nature, 461 (2009) 246-249.

210. [70] Z. Li, J. Martínez-Triguero, P. Concepción, J. Yu, A. Corma, Methanol to olefins: activity and stability of nanosized SAPO-34 molecular sieves and control of selectivity by silicon distribution, Physical Chemistry Chemical Physics, 15 (2013) 14670-14680.

211. [71] L. Tosheva, V.P. Valtchev, Nanozeolites: Synthesis, crystallization mechanism, and applications, Chemistry of Materials, 17 (2005) 2494-2513.

212. [72] S. Lee, M. Choi, Unveiling coke formation mechanism in MFI zeolites during methanol-to-hydrocarbons conversion, Journal of Catalysis, 375 (2019) 183-192.

213. [73] W. Qin, Y. Zhou, J.D. Rimer, Deleterious effects of non-framework Al species on the catalytic performance of ZSM-5 crystals synthesized at low temperature, Reaction Chemistry & Engineering, 4 (2019) 1957-1968.

Chapter 6 References

214. [1] World Rubber Production, Consumption and Trade http://www.mrepc.com/industry/world_production.php (accessed Jan 18, 2019).

215. [2] Tekasakul, P.; Tekasakul, S. Environmental Problems Related to Natural Rubber Production in Thailand. J. Aerosol Res. 2006, 21 (2), 122–129.

216. [3] Das, D.; Saha, A.; Bhattacharjee, H. Rubber Processing Is Detrimental to Environment: A Case Study. Int. J. Sci. Eng. Res. 2016, 7 (7).

217. [4] Vishnu, V.; Priyadarshini, C. S.; Hiny, H. ENVIRONMENTAL ISSUES CAUSED BY RUBBER INDUSTRY | The Environmental Impact by Nearby Businesses; Palayam, 2011.

218. [5] Duisters, H. A. M. Thermal Cracking of Butadiene; 1994; Vol. 33.

219. [6] Butadiene Market | Growth, Trends, and Forecast (2018–2023) https://www.mordorintelligence.com/industry-reports/butadiene-market (accessed Jan 9, 2019).

220. [7] White, W. C. Butadiene Production Process Overview. Chem. Biol. Interact. 2007, 166, 10–14. https://doi.org/10.1016/j.cbi.2007.01.009.

221. [8] Plotkin, J. S. The Continuing Quest for Butadiene - American Chemical Society https://www.acs.org/content/acs/en/pressroom/cutting-edge-chemistry/the-continuing-quest-for-butadiene.html (accessed Jan 9, 2019).

222. [9] Abdelrahman, O. A.; Dae, ⊥; Park, S.; Vinter, K. P.; Spanjers, C. S.; Ren, L.; Cho, H. J.; Vlachos, D. G.; Fan, W.; Tsapatsis, M.; et al. Biomass-Derived Butadiene by Dehydra-Decyclization of Tetrahydrofuran. ACS Sustain. Chem. Eng. 2017, 5 (5), 3732 – 3736. https://doi.org/10.1021/acssuschemeng.7b00745.

223. [10] Abdelrahman, O. A.; Park, D. S.; Vinter, K. P.; Spanjers, C. S.; Ren, L.; Cho, H. J.; Zhang, K.; Fan, W.; Tsapatsis, M.; Dauenhauer, P. J. Renewable Isoprene by Sequential Hydrogenation of Itaconic Acid and Dehydra-Decyclization of 3-Methyl-Tetrahydrofuran. ACS Catal. 2017, 7, 1428–1431. https://doi.org/10.1021/acscatal.6b03335.

224. [11] Bui, P.; Cecilia, J. A.; Oyama, S. T.; Takagaki, A.; Infantes-Molina, A.; Zhao, H.; Li, D.; Rodríguez-Castellón, E.; Jiménez López, A. Studies of the Synthesis of Transition Metal Phosphides and Their Activity in the Hydrodeoxygenation of a Biofuel Model Compound. J. Catal. 2012, 294, 184–198. https://doi.org/10.1016/j.jcat.2012.07.021.

225. [12] Cho, A.; Takagaki, A.; Kikuchi, R.; Oyama, • S Ted. Active Sites in Ni 2 P/USY Catalysts for the Hydrodeoxygenation of 2-Methyltetrahydrofuran. Top. Catal. 2015, 58, 219–231. https://doi.org/10.1007/s11244-015-0363-3.

226. [13] United States Patent. 2015. https://doi.org/10.1039/clcy(0.0125f).

227. [14] Kumbhalkar, M. D.; Buchanan, J. S.; Huber, G. W.; Dumesic, J. A. Ring Opening of Biomass-Derived Cyclic Ethers to Dienes over Silica/ Alumina. ACS Catal. 2017, 7, 5248–5256. https://doi.org/10.1021/acscatal.7b01436.

228. [15] Witzke, M. E.; Almithn, A.; Coonrod, C. L.; Hibbitts, D. D.; Flaherty, D. W. Mechanisms and Active Sites for C−O Bond Rupture within 2-Methyltetrahydrofuran over Ni, Ni 12 P 5 , and Ni 2 P Catalysts. ACS Catal. 2018, 8, 7141–7157. https://doi.org/10.1021/acscatal.7b04403.

229. [16] Kozhevnikov, I. V. Catalysis by Heteropoly Acids and Multicomponent Polyoxometalates in Liquid-Phase Reactions. Chem. Rev. 1998, 98, 171–198.

230. [17] Misono, M. Catalysis of Heteropoly Compounds (Polyoxometalates); 2013; Vol. 176. https://doi.org/10.1016/B978-0-444-53833-8.00004-1.

231. [18] Tanabe, K.; 田部浩三. New Solid Acids and Bases : Their Catalytic Properties; Kodansha, 1989.

232. [19] Mizuno, N.; Misono, M. Heterogeneous Catalysis; 1998.

233. [20] Macht, J.; Janik, M. J.; Neurock, M.; Iglesia, E. Catalytic Consequences of Composition in Polyoxometalate Clusters with Keggin Structure**. Angew. Chemie Int. Ed. 2007, 46, 7864–7868. https://doi.org/10.1002/anie.200701292.

234. [21] Corma, A. Inorganic Solid Acids and Their Use in Acid-Catalyzed Hydrocarbon Reactions. Chem. Rev. 1995, 95 (3), 559–614. https://doi.org/10.1021/cr00035a006.

235. [22] Farneth, W. E.; Gorte, R. J. Methods for Characterizing Zeolite Acidity. Chem. Rev 1995, 61 (95), 615–635.

236. [23] Bardin, B. B.; Bordawekar, S. V.; Neurock, M.; Davis, R. J. Acidity of Keggin-Type Heteropolycompounds Evaluated by Catalytic Probe Reactions, Sorption Microcalorimetry, and Density Functional Quantum Chemical Calculations. J. Phys. Chem. B 1998, 102 (52), 10817–10825. https://doi.org/10.1021/jp982345y.

237. [24] Janik, M. J.; Bardin, B. B.; Davis, R. J.; Neurock, M. A Quantum Chemical Study of the Decomposition of Keggin-Structured Heteropolyacids. J. Phys. Chem. B 2006, 110, 4170–4178. https://doi.org/10.1021/jp0553176.

238. [25] Macht, J.; Janik, M. J.; Neurock, M.; Iglesia, E. Mechanistic Consequences of Composition in Acid Catalysis by Polyoxometalate Keggin Clusters. J. Am. Chem. Soc. 2008, 130 (31), 10369–10379. https://doi.org/10.1021/ja803114r.

239. [26] Carr, R. T.; Neurock, M.; Iglesia, E. Catalytic Consequences of Acid Strength in the Conversion of Methanol to Dimethyl Ether. J. Catal. 2011, 278 (1), 78–93. https://doi.org/10.1016/j.jcat.2010.11.017.

240. [27] Janik, M. J.; Macht, J.; Iglesia, E.; Neurock, M. Correlating Acid Properties and Catalytic Function: A First-Principles Analysis of Alcohol Dehydration Pathways on Polyoxometalates. J. Phys. Chem. C 2009, 113 (5), 1872–1885. https://doi.org/10.1021/jp8078748.

241. [28] Knaeble, W.; Iglesia, E. Kinetic and Theoretical Insights into the Mechanism of Alkanol Dehydration on Solid Brønsted Acid Catalysts. J. Phys. Chem. C 2016, 120, 3371–3389. https://doi.org/10.1021/acs.jpcc.5b11127.

242. [29] Deshlahra, P.; Carr, R. T.; Chai, S.-H.; Iglesia, E. Mechanistic Details and Reactivity Descriptors in Oxidation and Acid Catalysis of Methanol. 2014. https://doi.org/10.1021/cs501599y.

243. [30] Barton, D. G.; Soled, S. L.; Iglesia, E. Solid Acid Catalysts Based on Supported Tungsten Oxides. Top. Catal. 1998, 6, 87–99.

244. [31] Deshlahra, P.; Iglesia, E. Toward More Complete Descriptors of Reactivity in Catalysis by Solid Acids. ACS Catal 2016, 6, 5386–5392. https://doi.org/10.1021/acscatal.6b01402.

245. [32] Noh, G.; Zones, S. I.; Iglesia, E. Consequences of Acid Strength and Diffusional Constraints for Alkane Isomerization and β-Scission Turnover Rates and Selectivities on Bifunctional Metal-Acid Catalysts. 2018. https://doi.org/10.1021/acs.jpcc.8b08460.

246. [33] Deshlahra, P.; Carr, R. T.; Iglesia, E. Ionic and Covalent Stabilization of Intermediates and Transition States in Catalysis by Solid Acids. J. Am. Chem. Soc. 2014, 136, 15229–15247. https://doi.org/10.1021/ja506149c.

247. [34] Deshlahra, P.; Iglesia, E. Reactivity and Selectivity Descriptors for the Activation of C−H Bonds in Hydrocarbons and Oxygenates on Metal Oxides. 2016. https://doi.org/10.1021/acs.jpcc.6b04604.

248. [35] Nowinska, K.; Fiedorow, R.; Adamiec, J. Catalytic Activity of Supported Heteropoly Acids for Reactions Requiring Strong Acid Centres; 1991; Vol. 87.

249. [36] Munnik, P.; De Jongh, P. E.; De Jong, K. P. Recent Developments in the Synthesis of Supported Catalysts. Chem. Rev 2015, 115, 6687–6718. https://doi.org/10.1021/cr500486u.

250. [37] Reichardt, C.; Welton, T. Solvents and Solvent E¤ects in Organic Chemistry, 4th ed.; Wiley-VCH: Weinheim, 2011.

251. [38] Kozhevnikov, I. V; Kloetstra ', K. R.; Sinnema, A.; Zandbergen, H. W.; Van Bekkum, ' H. Study of Catalysts Comprising Heteropoly Acid H,PW,20, Supported on MCM-41 Molecular Sieve and Amorphous Silica. J. Mol. Catal. A Chem. 114 (996), 287–298.

252. [39] Kuang, W.; Rives, A.; Fournier, M.; Hubaut, R. Structure and Reactivity of Silica-Supported 12-Tungstophosphoric Acid. Appl. Catal. A Gen. 2003, 250, 221–229. https://doi.org/10.1016/S0926-860X(03)00239-4.

253. [40] Kozhevnikov, I. V. Heterogeneous Acid Catalysis by Heteropoly Acids: Approaches to Catalyst Deactivation. J. Mol. Catal. A Chem. 2009, 305, 104–111. https://doi.org/10.1016/j.molcata.2008.11.029.

254. [41] Abdelrahman, O. A.; Vinter, K. P.; Ren, L.; Xu, D.; Gorte, R. J.; Tsapatsis, M.; Dauenhauer, P. J. Simple Quantification of Zeolite Acid Site Density by Reactive Gas Chromatography. Catal. Sci. Technol. 2017, 7 (17), 3831–3841. https://doi.org/10.1039/C7CY01068K.

255. [42] Buchanan, J. S.; Santiesteban, J. G.; Haag, W. O. Mechanistic Considerations in Acid-Catalyzed Cracking of Olefins; 1996; Vol. 158.

256. [43] Agrawal, R. K. ON THE COMPENSATION EFFECT. J. Therm. Anal. 1986, 31, 73–86.

257. [44] Conner, W. C. A General Explanation for the Compensation Effect: The Relationship between AS* and Activation Energy. JOURNAL OF CATALYSIS. 1982, pp 238–246.

258. [45] Barrie, P. J. The Mathematical Origins of the Kinetic Compensation Effect: 1. the Effect of Random Experimental Errors. Phys. Chem. Chem. Phys 2012, 14, 318–326. https://doi.org/10.1039/c1cp22666e.

259. [46] Bligaard, T.; Honkala, K.; Logadottir, A.; Nørskov, J. K.; Dahl, S.; Jacobsen, C. J. H. On the Compensation Effect in Heterogeneous Catalysis. J. Phys. Chem. B 2003, 107, 9325–9331. https://doi.org/10.1021/jp034447g.

260. [47] Hanwell, M. D.; Curtis, D. E.; Lonie, D. C.; Vandermeersch, T.; Zurek, E.; Hutchison, G. R. Avogadro: An Advanced Semantic Chemical Editor, Visualization, and Analysis Platform. Journal of Cheminformatics 2012.

261. [48] Pauling, L. The Principles Determining the Structure of Complex Ionic Crystals. J. Am. Chem. Soc. 1929, 51 (4), 1010–1026.

262. [49] Okuhara, T.; Mizuno, N.; Misono, M. Catalytic Chemistry of Heteropoly Compounds. Adv. Catal. 1996, 41, 113–252. https://doi.org/10.1016/S0360-0564(08)60041-3.

263. [50] Hiyoshi, N. Keggin-Type Polyoxometalate Nanosheets: Synthesis and Characterization via Scanning Transmission Electron Microscopy. Chem. Commun 2018, 54, 5217–5220. https://doi.org/10.1039/c8cc02978d.

264. [51] Hiyoshi, N.; Kamiya Heteropolyanions and, Y. Observation of Microporous Cesium Salts of 12-Tungstosilicic Acid Using Scanning Transmission Electron Microscopy. Chem. Commun 2015, 51, 9975–9978. https://doi.org/10.1039/c5cc01842k.

265. [52] Baker, L. C. W.; Mccutcheon, T. P. PHYSICAL AND INORGANIC CHEMISTRY Heteropoly Salts Containing Cobalt and Hexavalent Tungsten in the Anion1. J. Am. Chem. Soc. 1956, 78 (18), 4503–4510.

266. [53] Igarashi, T.; Zhang, Z.; Haioka, T.; Iseki, N.; Hiyoshi, N.; Sakaguchi, N.; Kato, C.; Nishihara, S.; Inoue, K.; Yamamoto, A.; et al. Synthesis of ε-Keggin-Type Cobaltomolybdate-Based 3D Framework Material and Characterization Using Atomic-Scale HAADF-STEM and XANES. Inorg. Chem 2017, 56, 5. https://doi.org/10.1021/acs.inorgchem.6b02748.

267. [54] de La Haye, J. L.; Guigner, J.-M.; Hasenknopf, B.; Lacôte, E.; Rieger, J. Cryo-TEM Observations and Xray Mapping of Polyoxometalate / Polystyrene Hybrid Nanoparticles with Surface Reactivity. In European Microscopy Congress 2016: Proceedings; Wiley-VCH Verlag GmbH & Co. KGaA: Weinheim, Germany, 2016; pp 716–717. https://doi.org/10.1002/9783527808465.EMC2016.5745.

268. [55] Long, D.-L.; Cronin, L.; Deng, W.; Zhang, Q.; Wang, Y.; Nisar, A.; Wang, X.; Zhu, G.; Geletii, Y. V; Zhao, C.; et al. Of Dalton Transactions Image Reproduced with Permission of Tomoji Ozeki Surfactant-Encapsulated Polyoxometalate Building Blocks: Controlled Assembly and Their Catalytic Properties A Dodecanuclear Zn Cluster Sandwiched by Polyoxometalate Ligands. Dalt. Trans 2012, 5, 12. https://doi.org/10.1039/C2DT30637A.

269. [56] Shi, C.; Wang, R.; Zhu, G.; Qiu, S.; Long, J. Synthesis, Characterization, and Catalytic Properties of SiPW-X Mesoporous Silica with Heteropolyacid Encapsulated into Their Framework. Eur. J. Inorg. Chem. 2005, 4801–4807. https://doi.org/10.1002/ejic.200500488.

270. [57] Alharbi, W.; Kozhevnikova, E. F.; Kozhevnikov, I. V. Dehydration of Methanol to Dimethyl Ether over Heteropoly Acid Catalysts: The Relationship between Reaction Rate and Catalyst Acid Strength. ACS Catal. 2015, 5, 7185–7193. https://doi.org/10.1021/acscatal.5b01911.

271. [58] Alharbi, W.; Brown, E.; Kozhevnikova, E. F.; Kozhevnikov, I. V. Dehydration of Ethanol over Heteropoly Acid Catalysts in the Gas Phase. J. Catal. 2014, 319, 174–181. https://doi.org/10.1016/j.jcat.2014.09.003.

272. [59] Bardin, B. B.; Davis, R. J. Effect of Water on Silica-Supported Phosphotungstic Acid Catalysts for 1-Butene Double Bond Shift and Alkane Skeletal Isomerization. Appl. Catal. A Gen. 2000, 200, 219–231.

273. [60] Rozanska, X.; Sautet, P.; Delbecq, F. F.; Fre´de´, F.; Lefebvre, F.; Borshch, S.; Chermette, H.; Bassety, J.-M.; Grinenval, E. This Journal Is c the Owner Societies. Phys. Chem. Chem. Phys 2011, 13, 15955–15959. https://doi.org/10.1039/c1cp21171d.

274. [61] Lee, J. S.; Yie, J. E. AN XANES STUDY OF CARBIDES OF MOLYBDENUM AND TUNGSTEN. Korean J. Chem. Eng 1991, 8 (3), 164–167.
275. [62] George, S. J.; Drury, O. B.; Fu, J.; Friedrich, S.; Doonan, C. J.; George, G. N.; White, J. M.; Young, C. G.; Cramer, S. P. Molybdenum X-Ray Absorption Edges from 200-20,000 EV, The Benefits of Soft X-Ray Spectroscopy for Chemical Speciation. J Inorg Biochem 2009, 103 (2), 157–167. https://doi.org/10.1016/j.jinorgbio.2008.09.008.
276. [63] Zhang, G.; Keita, B.; Ngo Biboum, R.; Miserque, F.; Berthet, P.; Dolbecq, A.; Mialane, P.; Catala, L.; Nadjo, L. SYNTHESIS OF VARIOUS CRYSTALLINE GOLD NANOSTRUCTURES IN WATER: THE POLYOXOMETALATE β-[H 4 PMo 12 O 40] 3-AS THE REDUCING AND STABILIZING AGENT. J. Am. Chem. Soc. 2009, 131, 16078–16087.
277. [64] Katsoulis, D. E. A Survey of Applications of Polyoxometalates; 1998.
278. [65] Chavan, L. D. Catalytic and Structural Studies of Some Heteropoly Acids and Polyoxometalates Part I.
279. [66] Baertsch, C. D.; Komala, K. T.; Chua, Y.-H.; Iglesia, E. Genesis of Brønsted Acid Sites during Dehydration of 2-Butanol on Tungsten Oxide Catalysts. J. Catal. 2002, 205, 44–57. https://doi.org/10.1006/jcat.2001.3426.
280. [67] Li, S*; Abdelrahman O.A*; Kumar, G*; Tsapatsis, M; Vlachos, D; Caratzoulas, S; Dauenhauer, P.J. Dehydra-Decyclization of Tetrahydrofuran on H-ZSM5: Mechanisms, Pathways, and Transition State Entropy. ACS Catalysis 2020, 9(11), 10279–10293. https://doi.org/10.1021/acscatal.9b03129

281. [68] Murphy, B. M.; Letterio, M. P.; Xu, B. Selectivity Control in the Catalytic Dehydration of Methyl Lactate: The Effect of Pyridine. ACS Catal. 2016, 6, 5117–5131. https://doi.org/10.1021/acscatal.6b00723.
282. [69] Dixon, J. E.; Bruice, T. C. Dependence of the Primary Isotope Effect (Kn/KO) on Base Strength for the Primary Amine Catalyzed Ionization of

Nitroethane. J. Am. Chem. Soc. 1970, 92 (4), 905–909. https://doi.org/10.1021/ja00707a028.

283. [70] Folkman, S. J.; Kirner, J. T.; Finke, R. G. Cobalt Polyoxometalate Co 4 V 2 W 18 O 68 10− : A Critical Investigation of Its Synthesis, Purity, and Observed 51 V Quadrupolar NMR. Inorg. Chem 2016, 55, 5343–5355. https://doi.org/10.1021/acs.inorgchem.6b00324.

284. [71] Dong, X.; Wang, D.; Li, K.; Zhen, Y.; Hu, H.; Xue, G. Vanadium-Substituted Heteropolyacids Immobilized on Amine- Functionalized Mesoporous MCM-41: A Recyclable Catalyst for Selective Oxidation of Alcohols with H 2 O 2. Mater. Res. Bull. 2014, 57, 210–220. https://doi.org/10.1016/j.materresbull.2014.05.041.

285. [72] Marleny Rodriguez-Albelo, L.; Rabdel Ruiz-Salvador, A.; Sampieri, A.; Lewis, D. W.; Gó Mez, A.; Nohra, B.; Mialane, P.; Jérô Me Marrot, ⊥; Sé, F.; Mellot-Draznieks, C.; et al. Zeolitic Polyoxometalate-Based Metal-Organic Frameworks (Z-POMOFs): Computational Evaluation of Hypothetical Polymorphs and the Successful Targeted Synthesis of the Redox-Active Z-POMOF1. J. Am. Chem. Soc. 2009, 131, 16078–16087. https://doi.org/10.1021/ja905009e.

286. [73] Hutter, J.; Iannuzzi, M.; Schiffmann, F.; VandeVondele, J. Cp2k: Atomistic Simulations of Condensed Matter Systems. Wiley Interdiscip. Rev. Comput. Mol. Sci. 2014, 4 (1), 15–25. https://doi.org/10.1002/wcms.1159.

287. [74] Wang, C.; Li, S.; Mao, X.; Caratzoulas, S.; Gorte, R. J. H-D Exchange of Simple Aromatics as a Measure of Brønsted-Acid Site Strengths in Solids. Catal. Letters 2018, 148 (11), 3548–3556. https://doi.org/10.1007/s10562-018-2563-5.

288. [75] Blasco-Ahicart, M.; Soriano-López, J.; Carbó, J. J.; Poblet, J. M.; Galan-Mascaros, J. R. Polyoxometalate Electrocatalysts Based on Earth-Abundant Metals for Efficient Water Oxidation in Acidic Media. Nat. Chem. 2017, 10 (1), 24–30. https://doi.org/10.1038/nchem.2874.

289. [76] Jones, A. J.; Iglesia, E. The Strength of Brønsted Acid Sites in Microporous Aluminosilicates. ACS Catal. 2015, 5 (5741–5755). https://doi.org/10.1021/acscatal.5b01133.

Appendices

The following appendices are supplementary information pertaining to the relevant preceding chapters, as noted. Additionally, the published works with supplementary materials are available online as well.

A1 Supplementary Materials for Chapter 3

Chemicals for zeolite synthesis. Zeolite synthesis was performed with the following reagents: tetraethylorthosilicate (TEOS, 98%, Sigma-Aldrich), LUDOX AS-30 (30% suspension in H_2O, Sigma-Aldrich), sodium hydroxide (NaOH, > 98%, Sigma-Aldrich), potassium hydroxide (KOH, 1M, Fisher Chemical), 1,8-diaminooctane (DAO, 98%, Sigma-Aldrich), aluminum sulfate hydrate ($Al_2(SO_4)_3$, 98%, Sigma-Aldrich), sodium aluminate (technical grade, Alfa Aesar), tetrabutylammonium hydroxide (TBAOH, 40%, Sigma-Aldrich), and tetrapropylammonium hydroxide (TPAOH, 40%, Alfa Aesar). Time-resolved acid titration experiments were performed using 2,4,6-trimethylpyridine (Sigma-Aldrich, >99%). All reagents were used as received without further purification. Deionized (DI) water, used in all experiments, was purified with an Aqua Solutions Type I RODI filtration system (18.2 MΩ). For reaction testing, methanol was purchased from J. T. Baker (99.8%), and the argon, oxygen, and nitrogen gases were purchased from Praxair (UHP grade, 99.999%).

Direct synthesis of conventional and finned ZSM-11 crystals. For the synthesis of conventional zeolite ZSM-11, TBAOH was used as the organic structure-directing agent (OSDA). In a typical synthesis, 0.220 g of sodium aluminate was added to a mixture of 0.786 g of NaOH solution (43 mg/g of solution) and 5.36 g of DI H_2O. To this solution was added 5.925 g of TBAOH, followed by the silica source, TEOS (9.707 g). The resulting mixture was stirred at room temperature in a sealed bottle for 2 h to allow for the hydrolysis of TEOS. The resulting solution was placed in a 60 mL Teflon-lined acid digestion bomb (Parr Instruments) that was sealed and heated in a Thermo Fisher Precision oven at 170 °C and autogenous pressures.

The autoclave was removed from the oven after 3 days and was quenched in water to room temperature. The molar compositions of synthesis mixtures were varied to synthesize conventional and finned ZSM-11 samples. The crystalline product was removed from the mother liquor by three cycles of centrifugation and washes with DI water, using a Beckman Coulter Avanti J-E centrifuge at 5 °C and 13,000 rpm for 10 min per cycle. Samples for catalysis were calcined in a Thermo Fisher Lindberg Blue furnace under constant flow of dried air (Matheson Tri-Gas) at 550 °C for 5 h with a temperature ramping/cooling rate of 1 °C/min. These samples were converted to an acid form (Brønsted acids) by ion exchange wherein calcined zeolite was mixed with 1.0 M ammonium nitrate solution to obtain a 2 wt % suspension. This mixture was heated to 80 °C under continuous stirring for 2 h to allow the exchange of Na^+ with NH_4^+. This process was performed three times washing between each ion exchange cycle. The final NH_4-zeolite samples were washed thrice with DI water before they were calcined once again with the same procedure stated above to generate H-form zeolites.

Seed-directed synthesis of finned ZSM-11 and ZSM-5 crystals. The ZSM-11 sample used as seeds was prepared with a molar composition of 10 DAO: 10 K_2O:100 SiO_2:1 Al_2O_3:4000 H_2O. In a typical synthesis, 0.185 g of aluminum sulfate was added to a mixture of 0.61 g of KOH solution (50 wt %) and 15.35 g of DI H_2O. To this solution was added 0.40 g 1,8-diaminooctane (DAO), followed by 5.45 g colloidal silica (LUDOX AS-30) and 2 wt % calcined ZSM-11 according to procedures outlined in a previous paper (*29*). The resulting mixture was stirred at room temperature for 24 h. The sol gel was then placed in a 60 mL Teflon-lined acid digestion bomb and heated in an oven at 160 °C and autogenous pressure for 3 days. The solids were isolated by the centrifuge/washing cycle listed above and the resulting seeds were immediately stored in water without allowing time for the solids to dry. A seeded growth solution was made with a molar composition of 27.3 DAO: 11.9 K_2O:90 SiO_2:0.5 Al_2O_3:3588 H_2O. The solution was prepared by adding an appropriate amount of $Al_2(SO_4)_3$ to a solution containing KOH and DI water, followed by the addition of DAO and LUDOX AS-30. The mixture was stirred at room temperature for 24 h prior to adding 10 wt% ZSM-11 seeds (relative to the total amount of growth solution). The suspension was heated for 2 days at 120 °C. The solids were extracted from the mother liquor using the centrifuge/washing procedure described above. The ZSM-5 sample used as seeds was prepared with a molar composition of 15 TPAOH: 4 Na_2O:100 SiO_2:1.67 Al_2O_3:2500 H_2O: 400 EtOH. In a typical synthesis, 0.094 g of sodium aluminate was added to a mixture of 1.022 g of NaOH solution (46 mg/g of solution) and 12.17 g of DI H_2O. To this solution was added 6.41 g TEOS, followed by the OSDA, TPAOH (2.30 g). The resulting mixture was stirred at room temperature for 2 h prior to heating the sol gel in an oven at T = 170 °C and autogenous pressure for 2 days. The isolated seeds were immediately placed in DI water for storage. A solution for seeded growth was prepared using a molar composition of 10 TPAOH: 0.5 Na_2O:31.5 SiO_2:0.5 Al_2O_3:1660 H_2O. The solution was prepared similar to the protocol for seeds with the addition of 5 wt% ZSM-5 seeds (relative to the total amount of growth solution) after aging the secondary growth solution. The mixture was heated for 24 h at 100 °C and the solids were extracted as a white powder. For processes employing a thermal annealing step, the gel after centrifugation was directly transferred to a solution with composition 10 TEOS: 14 TPAOH: 9500 H_2O, which was heated at 170 °C for 7 days. The solution was then removed from the oven and the solid was dried in air after multiple centrifugation and washing cycles.

Aluminosilicate self-pillared pentasil (SPP) synthesis. A SPP sample (Si/Al = 75) for acid titration measurements was synthesized following the reported procedure in Zhang et al. (*11*).

X-ray diffraction. The H-forms of the zeolite materials were characterized by powder X-ray diffraction (XRD) using a Rigaku SmartLab Diffractometer with Cu Kα radiation to verify the crystalline structure. Powder XRD patterns were compared to simulated patterns of each framework type provided by the International Zeolite Association Structure Database (*30*).

Scanning electron microscopy. Scanning electron microscopy (SEM) was performed with a FEI 235 dual-beam (focused ion-beam) system operated at 15 kV and a 5 mm working distance. All SEM samples were coated with a thin platinum layer (ca. 5 nm) prior to imaging to reduce the effects of charging.

Inductively coupled plasma-optical emission spectroscopy analysis. The molar Si/Al ratio of zeolite samples was measured by inductively coupled plasma analysis in combination with optical emission spectroscopy (ICP-OES). Before analysis, a Katanax X-300 Fusion Fluxer instrument was used to conduct the fusion of samples (approximately 100 mg) prepared by first dissolving with $LiBO_2$ (98.5 wt% lithium metaborate and 1.5 wt% LiBr).The mixture was heated to 1000 °C for 15 min. Then 2 N HNO_3 was added to the molten mixture and stirred for 10 min, followed by dilution with water to 50 g. The elemental components of the samples were analyzed using an Agilent 725 instrument.

X-ray photoelectron spectroscopy. Surface elemental analysis of zeolites was performed with X-ray photoelectron spectroscopy (XPS) using a PHI 5800 ESCA (Physical Electronics) system, which is equipped with a standard achromatic Al Kα X-ray source (1486.6 eV) operating at 300 W (15 kV and 20 mA) and a concentric hemispherical analyzer. Since zeolites are insulating materials, the equipment neutralizer component was utilized to prevent charging effects. All data was collected at a 45° takeoff angle, and collected spectra were analyzed using the MultiPak program.

Textural analysis. Textural analysis of H-form samples prepared for catalytic testing was performed by N_2 adsorption/desorption using a Micromeritics ASAP 2020. The data was analyzed by instrument software to obtain the BET surface area and the microporous volume was determined from the t-plot method.

Transmission electron microscopy. Transmission electron microscopy (TEM) images and selected area electron diffraction (SAED) patterns were taken with a JEOL JEM-2100 FEG TEM operated at an accelerating voltage of 200 kV. A Gatan Ultrascan CCD camera was used for collecting image data and a Gatan Orius 200D CCD detector was used for collect diffraction data. Sample particles were dispersed and ultrasonicated in ethanol and then dipped on a lacey carbon copper grid. Electron tomography was also performed using the JEOL JEM-2100 FEG. A Gatan 912 ultra-high tilt tomography sample holder was used in order to achieve a large tilt range. A tilt series of bright-field TEM images of a zeolite crystal particle was acquired over an angular range from -65° to +65°. The interval between neighboring images was kept at 1.0°. Before the sample was placed on the copper grid, a droplet of 5 nm gold nanoparticle dispersion was also delivered onto the copper grid as fiducial markers for tomogram alignment. The software ETomo was used for tilt series data processing, including alignment and reconstruction.

Temperature-programmed desorption of ammonia (NH_3-TPD). NH_3-TPD was performed on a Micromeritics Autochem II 2920 equipped with a TCD detector. Prior to TPD, 60-100 mg of catalyst was first out gassed in He for 1 h at 600 °C with a heating ramp of 10 °C min^{-1}. NH_3 was adsorbed at 100 °C until saturated, followed by flushing with He for 120 min at 100 °C. The ammonia desorption was monitored using the TCD detector until 600 °C with a ramp of 10 °C min^{-1}, using a flow of 25 mL·min^{-1}.

Methanol-to-hydrocarbons (MTH) reactions. Methanol conversion over H-form zeolite catalysts was carried out in a 1/4 inch stainless steel tube installed in a Thermo Scientific Lindberg Blue M furnace. The catalyst bed was supported between two plugs of quartz wool, and a K-type thermocouple (Omega Engineering) was inserted into the stainless tube to measure the temperature of the catalyst bed. Prior to the reaction, the catalyst bed was pretreated *in situ* at

550 °C for 3 h under flow of dried air (6 $cm^3 \cdot min^{-1}$ of O_2, 24 $cm^3 \cdot min^{-1}$ of N_2). After the pretreatment, the catalyst bed was cooled down to the reaction temperature, i.e., 350 °C. Methanol was fed by a syringe pump (Harvard Apparatus) at 7 $\mu L \cdot min^{-1}$ into a heated inert gas stream of Ar (30 cm^3/min), which resulted in a reactant flow with a weight hourly space velocity (WHSV) of 9 h^{-1}. To kinetically compare the deactivation rate of the catalysts, reactions were also performed at low methanol conversion (X), where C_{eff} is the carbon-based molar concentration of both methanol and dimethyl ether (DME) in the effluent and C_{feed} is the concentration of methanol in the feed. The selectivity (S_i) of hydrocarbon product *I*, where C_i is the carbon-based molar concentration of hydrocarbon i in the effluent and $C_{t,eff}$ is the total carbon-based molar concentration of hydrocarbons in the effluent.

Operando UV−Vis micro-spectroscopy with on-line mass spectrometry. The hydrocarbon pool species and related coke compounds formed during the MTH processes were determined using *operando* UV-Vis spectroscopy (*31, 32*). The UV-Vis spectra were obtained using an AvaSpec 2048L spectrometer connected to a high-temperature UV-Vis optical fiber probe, which was used to collect spectra in reflection mode. The measurements were performed in the wavelength range of 200-1000 nm (11000–50000 cm^{-1} in wavenumber) using a high-temperature UV-vis probe (Avantes), that comprises one excitation and one collection optical fiber with a size diameter of 400 μm and length of 1.5 m, which are placed in a stainless steel protection sleeve. The probe was connected to a deuterium-halogen light source and an AvaSpec 2048 UV-Vis spectrometer. The spectra were saved every 30 s, with 100 accumulations of approximately 50 ms exposure time each. Prior to the reaction, the catalysts with same pellet size to the performance testing were loaded in a fixed-bed quartz reactor and activated at 550 °C for 3 h under 100% oxygen and then cooled to 350 °C. The WHSV of methanol was kept at 20 h^{-1} by flowing He gas through a methanol saturator, which was kept at a temperature of ca. 293 K.

Fourier-transform infrared spectroscopy (FTIR). Time-resolved spectra were measured using a Bruker Vertex 70 FTIR with a HeNe laser and RT-DLaTGS detector (20 kHz scanner velocity, 6 mm aperture, KBr beam splitter). For sample preparation, ~15 mg of powder catalyst sample was homogenized using an agate mortar and pestle, pressed at 2-3 ton (Pike Technologies, CrushIR Digital Hydraulic Press) for 5 min into 13 mm-diameter pellets (International Crystal Laboratories, KBR Die, CAS#7758-02-3) and inserted into the cell body (Harrick Scientific, High Temperature Cell, Part No. HTC-M-05, CaF_2 windows). Before inserting the sample pellet, a background spectrum was collected (64 scans, 4 cm^{-1} resolution) with the empty cell. A K-type thermocouple (Harrick Scientific, Part No. 008-144) was in constant intimate contact with the sample pellet holder. The manufacturer-provided cartridge heater (100W, 24V) was controlled via a temperature controller in cascade mode (Omega CN7800). To ensure that the CaF_2 windows of the sample cell does not overheat, cooling water was continuously pumped (Control Company, Variable Flow Chemical Pump) and flowed through water cooling ports connected to the cell body. The sample was calcined at 500 °C for 4 h in air (Linde, Air Ultra Zero) at a ramp rate of 5 °C min^{-1}. After calcination, the sample was cooled down to and remained at 150 °C for the duration of the experiment to ensure the absence of water. For the amine purification, H-ZSM-5 (Zeolyst, CBV28014) was calcined under flowing air at 550 °C for 10 h at a ramp rate of 1 °C min^{-1}. Freshly calcined H-ZSM-5 was added to 20 mL of 2,4,6-trimethylpyridine and stirred vigorously (1,200 rpm) for > 1 h. H-ZSM-5 was isolated from 2,4,6-trimethylpyridine via centrifugation at 10,000 rpm for > 5 min. 2,4,6-trimethylpyridine was used immediately post-purification for dosing in FTIR. For the amine dosing process, He gas was flowed over the sample pellet to purge any remaining air. To ensure that the He is moisture-free, He gas was flowed through a liquid nitrogen trap and desiccator before reaching the cell body. The initial spectrum of the calcined catalyst was measured at this time, with the background spectrum subtracted. Purified 2, 4, 6-trimethylpyridine was flowed at 0.06 mL h^{-1} to the sample cell. FTIR spectra (64 scans, 4 cm^{-1} resolution, scan range from 4000 to 1000 cm^{-1}) were saved continuously at different time intervals during the duration of the experiment: every 30 s for the first 10 min, then every 30 min for the rest of the experiment.

Kinetic Monte Carlo simulations. Kinetic Monte Carlo (kMC) simulations were performed to study the transport of benzene through seed and finned silicalite-1 (a siliceous isostructure of zeolite ZSM-5 with **MFI** topology) crystals at 300 K. Benzene transport in silicalite-1 is characterized by infrequent jumps between three types of favorable adsorption sites located in the straight pores (*S*), sinusoidal channels (*Z*), and intersections (*I*) of the pores (Fig. 4, A – C). This hopping process is modeled using first-order kinetic equations that are solved stochastically using the rejection-free kMC algorithm described by Laloué et al. (*33*). The rate constants for the elementary transitions between adsorption sites were derived in a previous atomistic simulation study using rare-event sampling methods, in which they were shown to lead to good predictions of benzene's experimentally measured diffusivity (*26, 34*). The seed and finned zeolite crystals were created by replication of the orthorhombic (Pnma) unit cell of **MFI**, which has unit cell dimensions of a = 2.01 nm, b = 1.99 nm and c = 1.34 nm along its three principal crystallographic axes. The seed crystal was generated by replicating the unit cell to create a nearly cubic $247 \times 250 \times 372$ ($496.47 \times 497.50 \times 498.48$ nm^3) supercell with linear dimensions of ca. β = 500 nm in each direction (refer to Fig. 1A). The finned crystal was generated by decorating the surface of the smooth structure with smaller, nearly cubic $24 \times 25 \times 37$ ($48.24 \times 49.750 \times 49.58$ nm^3) supercells with linear dimensions of α = 50 nm in each direction; the fin location on the surface was chosen to ensure continuity of the pore network. As prescribed by the kMC model, the pore networks of both crystals were represented as lattices with *S*, *Z*, and *I* adsorption sites (refer to Fig. 4, A – C). On the order of 10^8 and 10^9 lattice sites were needed to represent the seed and finned structures examined in this study, respectively.

Mass transport through the seed and finned zeolite crystals was characterized by computing the diffusion path length for benzene, where $|\Delta \mathrm{r}_i| = |\mathrm{r}_i - \mathrm{r}_{i-1}|$ is the scalar distance travelled in the ith kMC step and r is the position vector of the molecule. The initial position r_0 at time $t_0 = 0$ was chosen by placing benzene at a randomly selected lattice site on the outside of crystal's bounding surface. The kMC moves were attempted and rejected until the molecule first crossed the bounding surface of the crystal, entering at position r_1 and time t_1. The trajectory of the molecule was then propagated for n kMC steps, with the n^{th} step corresponding to the event in which the molecule first exited the zeolite crystal by re-crossing the bounding surface. The residence time within the crystal was calculated as $\tau = t_{n-1} - t_1$. For each structure, the mean diffusion path length $\langle r \rangle$ and residence time $\langle \tau \rangle$ were estimated by averaging over 10^5 independent trajectories. In each case, only a single benzene molecule was simulated inside the crystal such that interactions between diffusing species could be neglected.

Simulations were performed for several models with different surface-to-surface fin spacing γ ranging from 4 to 50 nm to vary the surface density of fins from 3.27×10^{-4} to 1.01×10^{-4} nm^{-2}. The mean diffusion path length $\langle r \rangle$ and residence time $\langle \tau \rangle$ decrease monotonically as the surface density of fins increases. For the models examined, these metrics are reduced by a factor ranging from 1.5 to 2.5, thereby demonstrating that the mass transport characteristics of the finned crystals are enhanced relative to the seed zeolites for a broad range of fin densities.

A2 Supplementary Materials for Chapter 4

Chemicals for zeolite synthesis. Zeolite synthesis was performed with the following reagents: LUDOX AS-30 (30% suspension in H_2O, Sigma-Aldrich), sodium hydroxide (NaOH, > 98%, Sigma-Aldrich), potassium hydroxide (KOH, 1M, Fisher Chemical), Catapal B alumina (72% Al_2O_3, Sasol), aluminum sulfate ($Al_2(SO_4)_3 \cdot 18H_2O$, 98%, Sigma-Aldrich), cyclohexylamine (CHA, ≥99%, Aldrich), and pyrrolidine (Pyr, 99%, Aldrich). Time-resolved acid titration experiments were performed using 2, 3-dimethylpyridine (Sigma-Aldrich, 99%). All reagents were used as received without further purification. Deionized (DI) water, used in all experiments, was purified with an Aqua Solutions Type I RODI filtration system (18.2 MΩ). For reaction testing, 1-butene (99.9%) and nitrogen (99.99%) were purchased from Dalian Special Gases Co., Ltd.

Ferrierite sample preparation. The ferrierite seed was synthesized under hydrothermal conditions using a growth mixture with a molar composition of 4.8 NaOH: 1.0 Al_2O_3: 20 SiO_2: 5.0 CHA: 1.2 KOH: 750 H_2O. In a typical synthesis, a sodium aluminate solution was premade at 165 °C for 6 h by mixing with Catapal B alumina, NaOH and DI H_2O. Then 7.22 g (0.036 mol) of LUDOX AS-30 was added to a mixture of a sodium aluminate solution (15.1 wt% Na_2O, 16.8 wt% Al_2O_3, 0.0018 mol) and 15.49 g (1.35 mol) of DI H_2O. To this solution was added 0.05 g NaOH solution (10 wt%, 0.0086 mol) and 0.24g KOH solution (50 wt%, 0.0022 mol), followed by the organic structure-directing agent (OSDA) cyclohexylamine (CHA, 0.90 g, 0.0090 mol). The resulting mixture was stirred at room temperature to obtain a homogenous solution. The resulting solution was placed in a 60 mL Teflon liner within a metal autoclave (Parr Instruments) that was sealed and heated in a Thermo Fisher Precision oven at 165 °C and autogenous pressure. The autoclave was removed from the oven after 2 days synthesis and was quenched in water to room temperature. The sample was washed three times with DI H_2O. A fraction of the sample was dried under ambient conditions for further characterization; and the remaining fraction was kept wet for use in seed-assisted synthesis. Secondary growth of fins was accomplished using a mixture with a molar composition of 6.2 Na_2O: 0.71 Al_2O_3: 20 SiO_2: 14 Pyr: 800 H_2O. The solution was prepared by mixing approximate amount of $Al_2(SO_4)_3 \cdot 18H_2O$ and DI H_2O, followed by the additions of LUDOX AS-30 and NaOH. The OSDA pyrrolidine (Pyr) was then added to the mixture, which was stirred at room temperature for 3 h. Lastly, 20 wt% of ferrierite seed (wet) was added to the solution for secondary growth. The suspension was placed in a Teflon liner within an autoclave and heated for 24 h at different temperatures (120 to 140 °C) and then quenched to room temperature. The solution was then removed from the oven and the solid was dried in air after several cycles of centrifugation and washing with DI H_2O. The finned commercial sample was synthesized at 130 °C following the similar procedure except the use of the Zeolyst CP914C as the seed (dry).

Material characterization. As-synthesized materials were characterized by powder X-ray diffraction (PXRD) using a Rigaku SmartLab diffractometer with Cu-Kα radiation (40 kV, 44 mA) to verify the crystalline structure. Powder XRD patterns acquired from 5° to 50° 2θ with a step size of 0.02° were compared to simulated patterns of FER framework type provided by the International Zeolite Association Structure Database[1]. Scanning electron microscopy (SEM) was performed with a FEI 235 dual-beam (focused ion-beam) system operated at 15 kV and a 5 mm working distance. All SEM samples were coated with a thin platinum layer (ca. 5 nm) prior to imaging to reduce the effects of charging. Textural analysis of H-form samples prepared for catalytic testing was performed by N_2 adsorption/desorption using a Micromeritics ASAP 2020. The data was analyzed by instrument software to obtain the BET surface area and the microporous volume was determined from the t-plot method. The molar Si/Al ratio of all ferrierite samples was measured by inductively coupled plasma analysis in combination with optical emission spectroscopy (ICP-OES). Before analysis, approximate 50 mg of the sample was fused with $LiBO_2$ (98.5 wt% lithium metaborate and 1.5 wt% LiBr) by a Katanax X-300 Fusion Fluxer instrument. The mixture was heated to 1000 °C for 15 min, followed by the addition of 50 mL 2 N HNO_3 to the molten mixture and stirred for 10 min. An Agilent 725 instrument was used to analyze the elemental components of the samples. Aluminum speciation was determined from ^{27}Al MAS NMR spectra collected at a spinning frequency of 12.5 kHz, pulse of π/12, relaxation delay of 0.8 s, and 4 K scans at 11.7 T on a JEOL ECA-500 spectrometer. Additional ^{1}H MAS NMR measurements were performed with samples that were first dehydrated at 400 °C and a pressure below 10^{-2} Pa for 20 h. Spectra were collected at 600.13 MHz using single-pulse sequence with p/4 pulse, 4 s recycle delay. For the determination of quantitative results, all samples were weighed and the spectra were calibrated by measuring a known amount of adamantane performed under the same condition.

Samples for transmission electron microscope (TEM) investigations were dispersed in ethanol. After ultrasonication of the suspension, a droplet was taken and transferred to a lacey carbon copper grid. Then the droplet was dried in air at room temperature. TEM images and selected area electron diffraction (SAED) patterns were collected on a JEOL JEM-2100F microscope operated at 200kV (Cs 1.0 mm, point resolution 0.23 nm) using a Gatan Orius 200D CCD camera (resolution 2048 x 2048 pixels, pixel size 7.4 μm). 3D electron diffraction (3DED) and electron tomography datasets were collected on a Thermo Fisher Themis-Z TEM operated at 300 kV with a Gatan OneView camera. A Fischione model 2020 advanced tomography holder was used to engage the copper grid. The 3DED datasets were collected by *Instamatic* software[2] and then the 3D reciprocal lattices were reconstructed and visualized by *REDp* software[3]. The collection of electron tomography dataset was done in TEM mode using *TEM Tomography* software, which allows automatic focusing and tracking of the target. For this purpose, we used 5nm gold nanoparticles as fiducial markers for tomogram alignment. The tomography datasets were processed by *ETomo* software[4], in which tilt series alignment and 3D reconstruction were performed.

For acid titration experiments, time-resolved spectra were measured using a Fourier-transform infrared spectroscopy (FTIR) with a HeNe laser and RT-

DLaTGS detector (Bruker Vertex 70, 20 kHz scanner velocity, 6 mm aperture, KBr beam splitter). For sample preparation, about 15 mg of powder catalyst sample was homogenized using an agate mortar and pestle, pressed (Pike Technologies, CrushIR Digital Hydraulic Press) at ca. 3 ton for 5 min into 13 mm-diameter pellets (International Crystal Laboratories, KBR Die, CAS no.7758-02-3) and inserted into the cell body (Harrick Scientific, High Temperature Cell, Part no. HTC-M-05, CaF_2 windows). Before inserting each sample pellet, a background spectrum was collected (64 scans, 4 cm^{-1} resolution) with the empty cell. A K-type thermocouple (Harrick Scientific, Part No. 008-144) was in constant intimate contact with the sample pellet holder to measure the temperature. The manufacturer-provided cartridge heater (100W, 24V) was controlled via a temperature controller in cascade mode (Omega CN7800). To ensure that the CaF_2 windows of the sample cell does not overheat, cooling water was continuously pumped (Control Company, Variable Flow Chemical Pump) and flowed through water cooling ports connected to the cell body. The sample was calcined at 500°C for 4 h in air (Linde, Air Ultra Zero) at a ramp rate of 1°C min^{-1}. After calcination, the sample was cooled down to and remained at 240 °C for the duration of the experiment to ensure the absence of water. Cold 2,3-dimethylpyridine (Sigma-Aldrich, CAS no. 583-61-9) was used for dosing in FTIR. For the amine dosing process, He gas (Minneapolis Oxygen Company, Grade 5.0 He, UN1046) was flowed over the sample pellet to purge any remaining air. To ensure that the He is moisture-free, He gas was flowed through a liquid nitrogen trap and desiccator before reaching the cell body. The initial spectrum of the calcined catalyst was measured at this time, with the background spectrum subtracted. 2,3-dimethylpyridine was flowed at 0.06 mL h^{-1} to the sample cell. FTIR spectra (64 scans, 4 cm^{-1} resolution, scan range from 4000 to 1000 cm^{-1}) were saved continuously at different time intervals during the duration of the experiment: every 30 s for the first 30 min, then every 10 min for the rest of the experiment.

Catalyst testing. The skeletal isomerization of 1-butene to isobutene was carried out in a fixed bed micro-reactor with an inner diameter of 7 mm under atmosphere pressure. In a typical run, 0.15 g of catalyst was diluted with quartz sand to 0.5 g and put into the center of the reactor. The catalyst was activated at 500 °C in continuous nitrogen flow for 2 h. Then the temperature was cooled down to 400 °C. The mixture flow of 1-butene with nitrogen was fed into the fixed bed. The molar ratio of 1-butene to nitrogen was 1:1 and weight hourly space velocity (WHSV) of 1-butene was 12 h^{-1}. The reaction products were analyzed online by an Agilent 7890B gas chromatograph equipped with a flame ionization detector (FID) and an Al_2O_3 capillary column. To compare the catalyst performance in 1-butene isomerization reaction, the turnover number (TON) is calculated for a selected range of time on stream (TOS) using a modified form of the equation, where $[H^+]$ is the concentration of Brønsted acid sites and $F(\tau)$ is the experimental trend of molar flow rate of all hydrocarbon products as a function of time on stream evaluated between two times (t_1 and t_2).